BIT-ROCK INTERACTION IN ROTARY DRILLING:

NUMERICAL AND EXPERIMENTAL STUDY

by © Rosana A. Reyes Nava

A thesis submitted

to the School of Graduate Studies in partial fulfillment of the

requirements for the degree of

Master of Engineering

Faculty of Engineering and Applied Science

Memorial University of Newfoundland

May 2017

St. John's Newfoundland and Labrador

Abstract

This investigation describes the dynamic model of a rotary drilling system equipped with a PDC bit. Torsional and axial dynamics are modeled separately with the bond graph technique and coupled is given by a bit-rock interaction model that considers cutting and friction components at the bit cutters. The cases for contact loss are analyzed and included as numerical functions to account for bit-bounce and stick-slip during drilling. Co-simulation of the drillstring and bit-rock models is proposed to simplify the numerical implementation. Verification confirmed that the model was captured with sufficient accuracy and yields predictable results for known inputs. A methodology for bit-rock parameter acquisition is suggested. Simulation of a real drilling setup was performed and validated against experimental tests. For the analyzed ranges, simulations were in agreement with experimental results. This shows that a close prediction of the drilling response of a PDC bit is possible with the considered model.

Acknowledgement

First and foremost, gratitude for this achievement is given to God, the creator and sustainer of my life.

I would like to express my deepest gratitude to my graduate supervisors Dr. Stephen Butt and Dr. Geoff Rideout for their encouragement to pursue excellence during my graduate studies, for their invaluable guidance, and constant support throughout this research.

Sincere thanks to all the members of the Drilling Technology Laboratory at Memorial University of Newfoundland; especially to Igor Kyzym, Pushpinder Rana, Abdelsalam Abugharara, Hongyuan Qiu, and Jinghan Zhong; for their valuable assistance and suggestions provided during this investigation.

I would like to extend my gratitude to my mother Eunice and my beloved husband Gabriel, who have been a constant source of support and encouragement during the challenges of graduate school and life. I am truly thankful for having you in my life.

Table of Contents

List of Tables

List of Figures

Nomenclature

ROP	Rate of penetration
WOB	Weight on bit
TOB	Torque on bit
TOB_c	Cutting torque on bit
TOB_f	Friction torque on bit
WOB_c	Cutting weight on bit
WOB_f	Friction weight on bit
WOB_o	Applied weigh on bit
Ω	Bit angular velocity
Ω_o	Imposed angular velocity
θ	Bit angular position
k_{axial}	Drillstring axial stiffness
$k_{torsional}$	Drillstring torsional stiffness
I	BHA mass moment of inertia
M	BHA mass
V	Bit axial velocity
U	Bit axial position
ζ	Orientation of the cutting reaction
ε	Rock intrinsic specific energy
γ	Orientation of the frictional contact surfaces associated with the cutters

μ	Coefficient of friction
a	Drill bit radius
d	Depth of cut per revolution
l	Length of wearflat surface
n	Number of cutters of the bit
σ	Maximum contact pressure at the wearflat/rock interface
t_n	Time delay
E	Drilling specific energy
S	Drilling strength

Symbols and elements related to Bond Graphs

R	Resistor element
C	Capacitive element
I	Inertia element
Sf	Source of flow
Se	Source of effort
TF	Transformer
GY	Gyrator

List of Appendices

CHAPTER 1

INTRODUCTION

This chapter gives an introduction to dynamic simulation of bit-rock interaction and its influence on drillstring vibrations with a brief context description on the importance of reduction of vibrations for optimization of the drilling process. It also states the problem of severe vibrations in drillstrings and the relevance of performing numerical simulations of these conditions. Finally, an approach for the simulation of a drilling system is presented as well as the thesis structure.

1.1. Research Context and Motivation

World energy demand is constantly rising and the process of oil and gas recovery for its generation is becoming more complex. In the 19th century, oil was available at shallow depths and production companies had access to it with simpler and cheaper production technologies. Since then, resources at shallow depths have been drastically reduced, and companies have moved towards deeper and more intricate sources of hydrocarbons. The oil and gas industry is constantly focusing on cost reduction in order to maximize the income. One of the major areas of this is the optimization of the drilling process, which represents a major portion of exploration and production of hydrocarbons [1].

Cost optimization of the drilling process includes the increase of rate-of-penetration (ROP) and the decrease of unplanned downtime. Generally, the longer it takes to drill a well, the more expensive the project will be. The improvement of downhole equipment and bit technologies such as the Polycrystalline Diamond Compact (PDC) bit has significantly increased in the past 20 years leading to faster ROP [1]. Regarding downtime, the unplanned interruption of drilling resulting from drillstring or downhole equipment failure is very expensive, especially in offshore applications where the rig operation costs are higher than in on-shore operations. There are different reasons for drill pipes and downhole tools failure, but high vibrations under extreme drilling conditions account for the majority of the cases. In this context, all attempts to avoid unfavorable conditions are justified. This can be accomplished by understanding what causes these conditions in order to change drilling strategies to decrease the severity of the vibration and its consequences.

Subjecting equipment to field-like conditions in order to observe the behavior is a good way to study the vibrations in drilling equipment. However, with computation capacity increasing each day and the availability of numerical modeling software packages, it seems more reasonable to simulate and study vibrations in a controlled environment. This approach eliminates the risk of damaging highly expensive equipment. By developing numerical models that can simulate dynamic drilling conditions, it is possible to project and understand the circumstances under which undesired vibrations occur. This will allow developing drilling plans that, in combination with tools for vibration control, can decrease downtime due to equipment failure.

1.2. Problem Statement

The drillstring on a rotary drilling system is constantly subjected to severe conditions that can negatively affect the drilling performance and the bit condition, which can introduce long delays in the drilling process. This research is focused on two kinds of vibrations that are common in rotary drilling with PDC bits: axial vibrations that can lead to a loss of contact between the bit and the rock (bit-bounce) and torsional vibrations that can lead to stick-slip. During stick-slip, the bit experiences two phases: sticking (the bit stops while the top of the drillstring keeps rotating) and slipping (the bit is released from sticking with a higher angular velocity than the top section of the drillstring) [2].

Torsional vibrations are detrimental for both the drillstring and the bit, and are documented to occur at least 50% of the on-bottom drilling time [2]. These vibrations can be mitigated in the field by changing the drilling parameters at risk of reducing the ROP or introducing other types of vibrations that can exacerbate the damaging effects of these phenomena [3]. This is because, according to experimental evidence, stick slip instabilities depend on bit-rock interaction [4]. Furthermore, simulation based studies suggest that any given perturbation, such as axial motion of the bit, can trigger self-excited stick slip vibrations of the system and vice versa [5].

The bit-rock interface reaction forces are a critical input for vibration analysis of the drillstring but are often done with overly simple treatment (e.g., sinusoidal force, displacement input) or with stochastic models for which parameter identification is difficult. Another challenge for drillstring simulations is that state-of-the-art models are commonly formulated by delay differential equations (DDE), in which the modification of the drillstring configuration and the external sources of excitation is not straight forward, thus the inclusion of downhole tools or other equipment in the drillstring requires a full reconsideration of the governing equations.

For this reason, a drillstring numerical model that considers the reaction forces from bit-rock interaction, and where the parameters are either obtained from the state variables of the drillstring model or from measurable quantities, is needed.

1.3. Research Objectives

The main purpose of this research is to develop a numerical model of a simple vertical rotary drilling system equipped with a double-cutter PDC bit. This model considers both torsional and axial vibration, which are coupled through a bit-rock interaction model. Additionally, a new approach for obtaining the bit-rock model parameters from drilling experiments and physical measurements is proposed. Furthermore, this investigation also seeks to confirm the utility of the model and the process for parameter acquisition through analysis of the model simulation and comparison against experimental drilling tests.

1.4. Thesis Outline

Chapter 2 presents an examination of the background material related to rotary drilling and drillstring modeling. A review of the different approaches for drillstring modeling is presented. This includes modeling of the bit-rock interface reactions and different suggestions to explain the development of torsional vibrations. Drillstring modeling in this investigation is done using the bond graph technique, thus this section also provides insight on the utility of bond graphs as a tool for graphical representation of physical systems. It also outlines the basic concepts and standard elements used in bond graph modeling.

Chapter 3 describes the mathematical formulation of the problem by considering the physical laws that apply to the system and by defining the coordinate system. This section also presents the bond graph model representation for two variants of the drillstring model. To complete the numerical formulation, a description of the bit-rock interaction equations model formulation is provided.

Chapter 4 describes the implementation of the model and the numerical method used to solve it. This section presents the results of the model simulation and the process of model verification; this includes verification against similar models, confirmation of initial assumptions, and analysis on how the bit-rock parameters affect the vibrations on the system. Chapter 4 also provides details on the co-simulation of the model using two software programs.

Chapter 5 presents the development and results of a systematic experimental program. The experiments involve drilling in concrete samples with a lab scale drilling rig equipped with a double-cutter PDC bit and an axial compliance tool. The purpose of these drilling tests is to obtain real-time vibration and drilling performance data in order to perform validation of the simulation results. This chapter also describes the procedure for obtaining the bit-rock interaction parameters from drill-off tests and physical measurements, as well as other preliminary experimental tests performed in order to find the simulation parameters for the lab scale drilling system.

Chapter 6 provides concluding observations about the most relevant results, the main contribution of the research, and recommendations for future work.

CHAPTER 2

TECHNICAL BACKGROUND

2.1. Fundamentals of Rotary Drilling

Rotary drilling is the standard method used in the oil and gas industry to penetrate formations and create a well for the hydrocarbons to travel from the reservoirs to the surface. The well is drilled by applying a downward force and a constant rotation to a bit that will break the rock into small pieces [6]. Figure 2.1 shows a common rotary drilling rig. A rotary table or a top drive is turned on the surface, and the torque is transmitted to the bit by a set of connected pipes called drillstring. Finally, a drilling fluid is circulated down the drillstring pipes and through the bit in order to clean the bottom-hole from the generated cuttings. The rock cuttings are then lifted to the surface through the annular space between the borehole and the drillstring exterior [7].

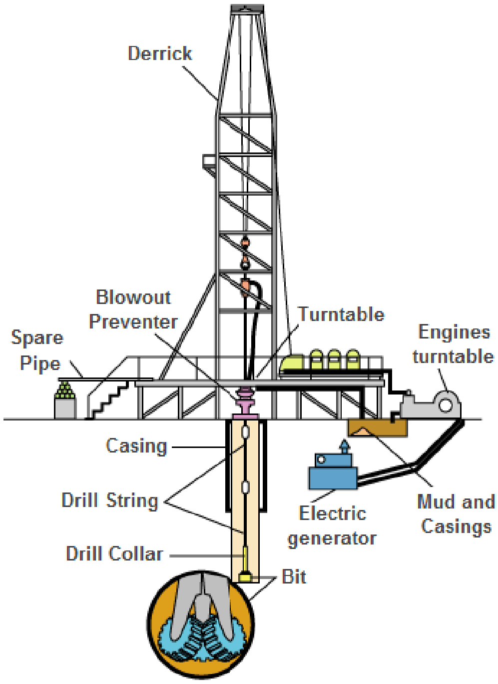

Figure 2.1. Elements of a rotary drilling rig [8]

Performance is an important factor in drilling processes, this is mainly due to operational costs and scheduled timelines; therefore, accomplishing high drilling rates is one of the main goals. The main parameter that drilling engineers consider as a performance indicative is the rate of penetration (ROP). By altering the basic drilling parameters, the driller is able to enhance ROP and obtain better drilling results.

ROP is primarily affected by changes in the weigh-on-bit (WOB), the total downward force that the bit is being subjected to. However, the relation is not linear for all WOB ranges. Figure 2.2a shows a typical plot of ROP vs. WOB with all other variables held constant. At first, no significant penetration is obtained. When the threshold formation stress is exceed (point a), ROP increases linearly with WOB until a point where the subsequent increases in WOB cause only slight improvements in ROP. Drilling beyond this point (point D), may cause a decrease in ROP. This is attributed to inefficient borehole cleaning due to the higher rate of cuttings generated; also, a higher depth of penetration of the bit in the rock leaves less clearance for the fluid to pass [7].

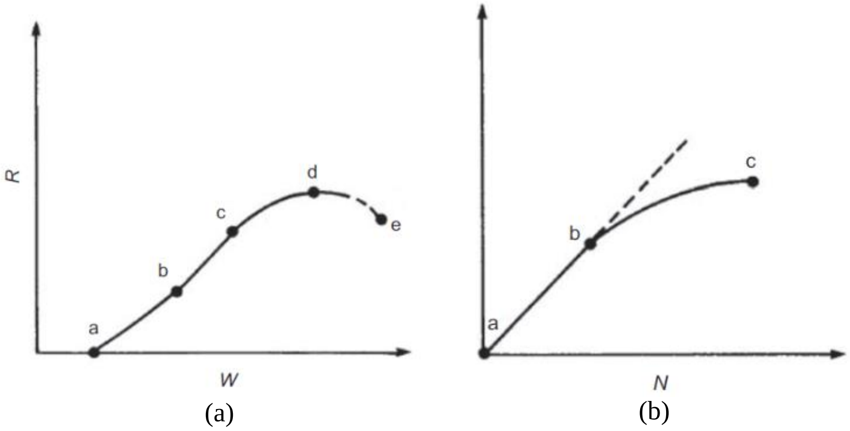

(a) (b)

Figure 2.2. Factors affecting ROP. a) WOB vs. ROP. b) Angular speed vs. ROP [7]

In terms of angular speed, rotation of the bit allows for removal of fractured rock in front of the cutter faces. A typical plot of ROP vs. angular speed is shown in Figure 2.2b. For low values of angular speed, ROP increases linearly but at higher rotary speeds, the ROP response is reduced; this phenomena is also attributed to poor bottom-hole cleaning [7].

2.2. Basic Drilling Components

2.2.1. Drilling Rig

Almost all operations in the drilling industry are performed by rotary drilling rigs, these vary widely in size, capability, level of automation, and environment in which they operate. However, all rigs have six basic systems:

(i) Power System:

Provides the required power for all the other systems by means of a combustion generator.

(ii) Hoisting System:

Provides a means for vertical movement of the drill pipes in the well (i.e., to lower or raise the drillstring and any other equipment into or out of the well)

(iii) Circulating System:

Provides hydraulic power to the drilling fluid so that it can be circulated from surface into the drillstring, all the way down the bottom- hole, and then return to surface carrying the rock cuttings.

(iv) Rotary System:

Includes all the equipment that provides torque to achieve rotation of the bit.

(v) Well-control System:

Prevents the uncontrolled flow of formation fluids from the wellbore to the surface.

(vi) Well-monitoring System:

Includes all sensors, signal transmitters, and controllers that allow the rig personnel to keep track of all the operating parameters in order to make necessary adjustments and to quickly detect and correct drilling problems.

Additionally, floating offshore rigs have a special marine system required to deal with the particularities of offshore drilling [6].

2.2.2. Drillstring

The drillstring is the main component in a drilling system. In general, drillstrings are comprised by two major sections: standard drill pipe and the Bottom-hole-assembly (BHA). The BHA consists of drill collars and a drill bit. For specific purposes, the BHA also includes stabilizers, steerable motors, and measurement and logging tools, among other features. The drill collars are thicker and heavier than the drill pipes and provide total WOB needed as a downward force [9]. Since the main function of the drillstring is to transmit the axial force and torque needed by the bit, it is susceptible to severe vibrations and consequently to failures.

2.2.3. Bit

The bit is the fundamental tool used in drilling; it performs the cutting action of the rock. Selection of the best bit and bit operation conditions is one of the problems that engineers face when drilling [7]. There is a wide variety of drilling bits that can be used according to the drilling conditions; however, for rotary drilling they are mainly classified into two categories: roller-cone bits and fixed cutter bits.

Roller-cone bits have one or more cones with cutting elements; the cutting elements rotate along the cone axis when the bit is rotated against the formation (see Figure 2.3a). Common materials used for roller-cone bit cutters are steel, which are typically used for relative soft formations; for harder and more abrasive applications, tungsten carbide is used [6].

Fixed cutter bits contain fixed blades integrated in the bit body; the bit and the blades rotate as a single unit. This represents an advantage because there is no concern for failure of moving parts. Also because of the shearing action of the cutters, these bits require a lower WOB and can be used for a wider range of formations [6]. Polycrystalline Diamond Compact (PDC) bits are a common type of fixed cutter bits (See Figure 2.3b). The cutters of a PDC bit are made out of layers of synthetic polycrystalline diamond that are bonded to a tungsten carbide substrate in a high pressure/high temperature process. The sharp planes of the diamond crystals are randomly oriented, which prevents breakage of any individual crystal from being propagated to the rest of the crystal and thus avoids shock-induced breaking of the entire cutter [7].

(a) (b)

Figure 2.3 (a) Roller-cone bit [10] (b) PDC bit [11]

2.3. Review of Drillstring Modeling Literature

2.3.1. 1950s: Static Models

Up until the 1950s, early analysis on drillstring was limited to static models, this was purposed to perform stress analysis. Models of the external environment were developed to obtain a torque and drag model that reflected the frictional contact between the drill pipe and the wall. This model determined the difference between the applied torque/weight and the actual torque/weight that the bit was being subjected to. Using the well path and a torque and drag static model, the static loads on each section were predicted to show that these loads did not lead to failure of the drillstring [12].

In these early analyses, the presence of dynamic influences was noticed and some attention was devoted to understanding the relevance of the dynamic effects. However, due to the existence of many aspects that were not easily addressed or fully understood, none of this research became standard application for stress analysis [12]. Some of these phenomena include:

- Non-linear damping effects.
- A non-linear dynamic model of the drill string lateral impact with the borehole.
- The determination and quantification of self-excited vibration phenomena.

These challenges have since been overcome and the next section provides a more detailed description.

2.3.2. First Dynamic Models: Uncoupled Vibrations

The development of basic dynamic models came with the necessity of understanding the modal contents of the drillstring dynamics in order to mitigate vibration effects. Elasto-dynamic uncoupled models were first developed in the 1960s with the purpose of studying natural frequencies and mode shapes of vibration in drillstrings. Bailey and Finnie [13] investigated the longitudinal and torsional vibrations with an analytical method that modeled the drillstring and drill collar. Simple boundary conditions were considered and a trial-and-error method was used to find natural frequencies.

The first dynamic models were developed from the simple lateral, axial and torsional vibrating beam equations. They were uncoupled, that is to say they considered only one motion direction at a time. These models did not consider excitation from the bit-rock interaction or the drillstring-wellbore contact either [14].

Lumped models were developed later. For the torsional dynamics, the common lumped model considered the drillstring and drill collar as a torsional pendulum (see Figure 2.4). In these models, the drill collar is responsible for most of the inertial mass and the drill pipe acts as a torsional spring [15], [16], [17]. Some models also considered other dynamics effects from the mass of the rotary table, the friction in the wellbore, and the mud circulation.

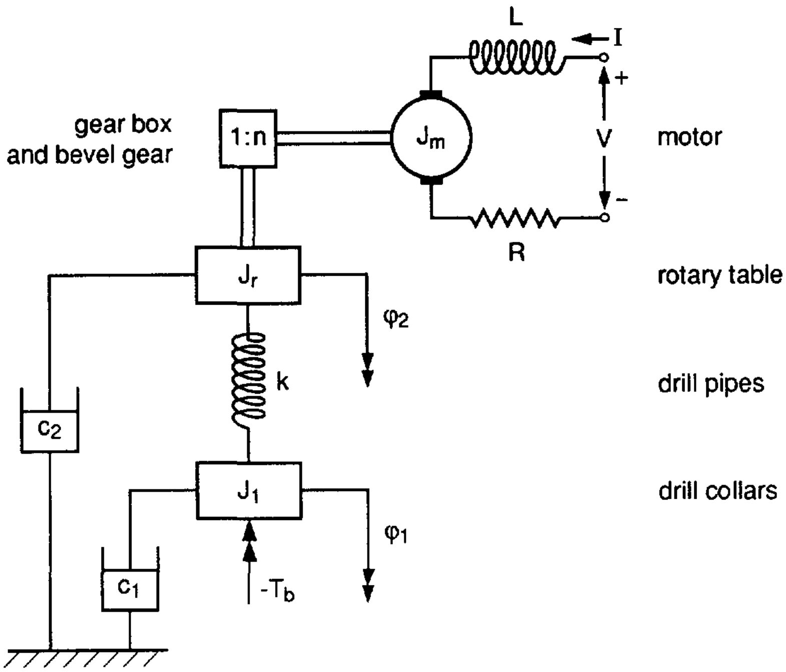

Figure 2.4. Representation of a drillstring as a torsional pendulum driven by an electric motor [15]

Although uncoupled models were of great interest, a more accurate prediction of the dynamic response was necessary for practical drilling applications. Realistic numerical modeling of phenomena such as non-linear friction and bit-rock interaction needed to be considered. The motivations for upgrading the drillstring analysis to coupled dynamic models was to be able to investigate how the real-time control in operating drilling parameters could mitigate the severe drillstring vibration levels [18].

2.3.3. Coupled Dynamic Models

One of the first investigations regarding coupling between drillstring vibration modes was performed by Aarrestad and Kyllingstad [19]. They acknowledged that the frequency spectra of axial acceleration and WOB contained dominating vibration frequencies related to the angular speed. This was explained by a non-linear coupling model between torsional and axial dynamics.

The first coupled drillstring models were developed in the 1990s. Since then, many investigations have been performed regarding coupling mechanisms and dynamics of the drillstring response to these mechanisms. Coupling has been studied between axial and bending vibrations [20], torsional and bending vibrations [21], [22], and axial and torsional vibrations [5], [23], [24]. Furthermore, integrated models have been developed [25], [26], [27] to take into account the mutual dependence of the three vibration modes based on effects such as bit-rock and drillstring-borehole interaction. These are developed in order to assess stability and design control strategies for vibration mitigation.

2.3.4. Bit-rock Interaction Modeling

One of the widely discussed subjects in coupled drillstring models is the bottom boundary condition or bit-rock interaction. The coupling nature of the bit-rock interaction has been experimentally and analytically shown to be the cause for self-excited torsional vibrations and for the development of certain vibration types when other vibrations are introduced in the system [28].

Early studies of bit-rock interaction dynamics were performed by modeling the axial reaction force from the rock as a spring-damper system. These models also included a sinusoidal displacement function that simulated the lifting action of the bit. In these studies, the frequency content of the displacement source was related to three times the angular speed as seen on tri-cone bit experimental data. Additionally, it was found that, the stiffness and damping is strongly dependent on the rock type and on the drilling parameters such as WOB and ROP [29].

Concerning torsional vibrations and stick-slip, the earliest investigations attributed these phenomena to drillstring static friction effects. Since the static friction coefficient is greater than the dynamic friction coefficient, the potential energy stored in the drill pipes could be transferred to inertial energy in the BHA. This would cause the drillstring to stick and then to accelerate to a faster speed than nominal [17]. These studies did not attribute stick-slip to the bottom-hole contact because field data showed that it could happen in off-bottom circumstances. However, later studies performed by Brett [30] showed that torsional vibrations were developed while drilling with PDC bits even if the drillstring rotated smoothly while off-bottom. This was attributed to an inherent characteristic of the PDC bits, in which a reduced torque is exhibited, with increased angular speed (see Figure 2.5). Brett’s investigation suggested that the negative slope in the Torque-RPM curve could have an effect in torsional vibrations similar to the classic static/dynamic friction approach.

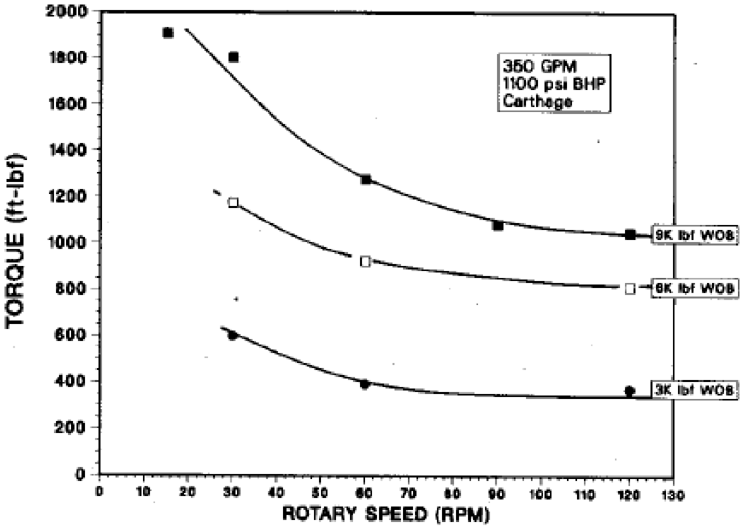

Figure 2.5. Torque variation with rotary speed for a PDC bit [30].

The first investigations regarding coupling at the bit-rock interface suggested that this interaction was characterized by the coexistence of two processes: rock cutting at the cutter face and frictional contact at the wear flat surface (see Figure 2.6) [31].

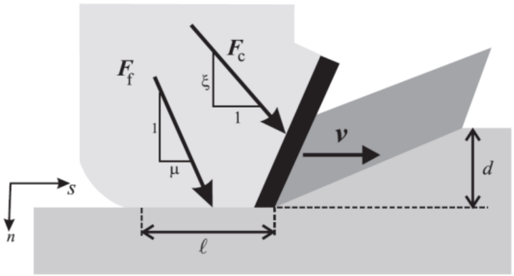

Figure 2.6 Forces acting on a single cutter [28]

The following equations were proposed by Detournay and Defourny [31] to characterize the reactions from the bit-rock interface based on the existence of these two processes. The parameters used in the equations (ζ, ε, γ, μ, a) are characteristic of formations and bit geometry, and are further described in [28] and [31].

$$W = W^c + W^f \tag{2.1}$$

$$T = T^c + T^f \tag{2.2}$$

$$W^c = \zeta \varepsilon a d \tag{2.3}$$

$$T^c = \frac{\varepsilon d a^2}{2} \tag{2.4}$$

$$d = \frac{2\pi ROP}{\omega} \tag{2.5}$$

$$T^f = \frac{W^f \gamma \mu a}{2} \tag{2.6}$$

where

W^c, T^c	Cutting components of force and torque;
W^f, T^f	Friction components of force and torque;
ω	Bit angular speed;
ζ, ε, γ, μ	Bit-rock interaction parameters
d	depth of cut per revolution
a	Bit radius.

In the bit-rock model described by equations 2.1 to 2.6, both the force and torque reactions are composed of cutting and friction components. Equations 2.3 and 2.4 suggest that the cutting component depends on the depth of cut per revolution. Equation 2.6 proposes that there is a constraint between the frictional component of the torque and the friction weight-on-bit. These premises define a set of relations between force, torque, angular velocity, and ROP.

Another approach was proposed by Christoforou and Yigit [26] for the bit-rock interaction governing equations. The WOB is composed of a static and a fluctuating component. The static component is determined by applied weight and the fluctuating component is given by bit-rock contact conditions as:

$$F_f(x,\phi) = k_c(x - x_o \sin n_b\phi) \tag{2.7}$$

where

k_c Formation contact stiffness.

In equation 2.7, the term $(x_o \sin n_b\phi)$ is a prescribed function that represents the lobed pattern observed in previous experimental tests. For the TOB, another prescribed function $f(\dot{\phi})$ is introduced to represent the decrease of torque with speed proposed by [30]:

$$T(x,\phi,\dot{\phi}) = \mu F_f(x,\phi) f(\dot{\phi}) \tag{2.8}$$

Based on previous investigations [31], Richard *et al* [32] proposed an extension of the bit-rock model where the governing equations were rate-independent. This model considered the potential loss of contact between the rock and the wear flats during bit-bounce and showed that this upward motion could route energy from axial to torsional vibration modes. It also added inertia effects of the BHA on axial vibrations. This approach introduced the axial position of the bit as a variable which allowed for calculation of the depth of cut as an instantaneous value instead of an average. The depth of cut calculation takes into account the bit position at an *a priori* unknown time, and as a consequence, introduces a delay in the system equations [32].

A later investigation on the bit-rock interaction laws by Richard *et al* [28] confirmed the instability of the bit-rock model even in trivial conditions. It was observed that any disturbance was enough to generate self-excited vibrations, and that the cause was the delayed and coupled nature of the cutting process. The main outcome of this research is that the apparent velocity-weakening effect on the torque is a consequence of the instability rather than an intrinsic property of the process.

Variation of the friction forces with instantaneous depth of cut has recently been further investigated. An extended model has been proposed, in which three distinct operating regimes affect the variation of the friction forces with d (see Figure 2.7). Phase I suggests that, on drilling regimes with a low depth of cut, there is a progressive increase of the friction forces with d due to a geometrical effect. This is seen on the figure as the directly proportional change of w_f with d for values of $d<d^*$. Phase II refers to the classic assumption that the friction forces are constant. This is presented in the figure as the vertical line where w_f is constant for $d_b.>d>d^*$. Finally, phase III indicates that there is not a unique response after phase II; therefore, the change of w_f when $d>d_b$ can be directly proportional (A) or inversely proportional (B). The lack of uniqueness in this phase is shown in experimental tests presented in [33]. In these, different results were obtained when drilling was performed under different loading conditions (kinematic control and WOB control).

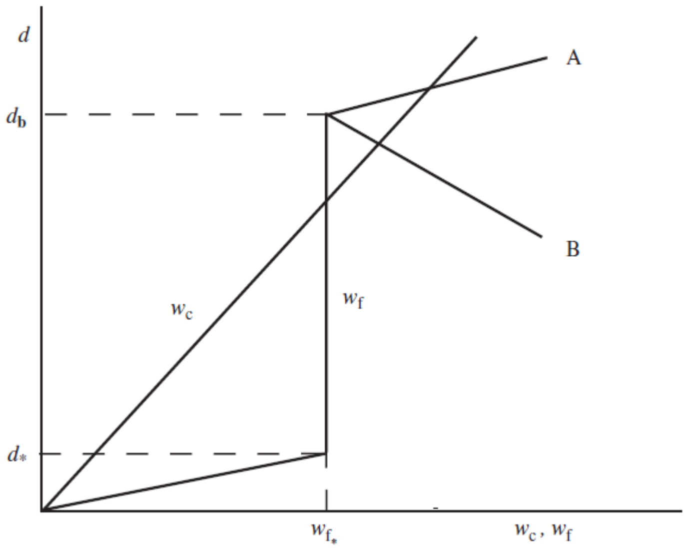

Figure 2.7. Conceptual response of the bit in the w_c–d and w_f–d spaces [33].

(i) Bit-rock Interaction Parameter Calculation.

One of the main challenges of the bit-rock interaction model is the parameter acquisition. In order to validate the model, it is necessary to compare numerical results with experimental data. In this case, bit-rock model parameters cannot be assumed but must be obtained from real experimental or field data.

In 1992, the E-S diagram was introduced by Detournay and Defourny [31] to provide a rational framework for the interpretation of field data. However, the diagram requires accurate field measurements of WOB, TOB, ROP, and angular velocity. Furthermore, the E-S diagram is based on the constraint introduced by the bit-rock interface laws. If equations 2.1 to 2.4 are substituted in 2.6, the result is:

$$\frac{2T}{a^2 d} = (1-\beta)\varepsilon + \mu\gamma\frac{W}{ad} \tag{2.9}$$

$$\beta = \mu\gamma\zeta \tag{2.10}$$

Two terms are introduced, the drilling specific energy (E) and the drilling strength (S):

$$E = \frac{2TOB}{a^2} \tag{2.11}$$

$$S = \frac{WOB}{a} \tag{2.12}$$

By substituting E and S into equation 2.9, the following relation is obtained:

$$E = E_0 + \mu\gamma S \tag{2.13}$$

where

$$E_0 = (1-\beta)\varepsilon \tag{2.14}$$

Equations 2.13 and 2.14 suggest that the drilling response of a PDC bit should be along a straight line; this is called the friction line and is shown in Figure 2.8. From the slope of the friction line, it is possible to obtain the combined term μγ. To obtain the other parameters, the cutting point needs to be found. This point corresponds to a perfect sharp cutter. Therefore, drilling must be performed with sharp and blunt cutters in order to completely characterize the bit-rock interaction under this technique, as is the case of experimental tests presented in [28], [31], [34], [35].

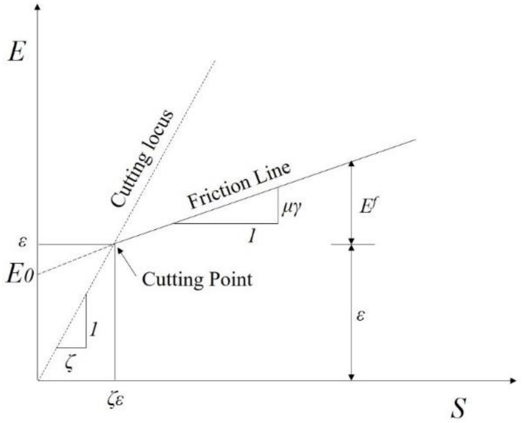

Figure 2.8. E-S diagram. Modified from [31].

A later investigation of the drilling response of drag bits presented by [33] suggested a potential for extracting bit-rock properties on the basis of the existence of the phases shown in Figure 2.7. However, it is difficult to make direct extraction of the parameters, if the information attached to the drilling data is not explicitly used. In this case, assumption of the parameter ζ is required to calculate the intrinsic specific energy ε.

Based on the presented literature, it is possible to conclude that the approach suggested by Detournay and Defourny [31], later studied by Richard *et al* [28] is more likely to better describe the real causes of this phenomenon. In other approaches, such as those presented by Brett [30] and Christoforou and Yigit [26], the velocity-weakening effect is considered as a property of the process occurring at the bit-rock interface. Although many experiments have shown this effect to be true, laboratory data was usually averaged over many rotations and the period of stick-slip vibrations is typically on a smaller time scale [32]. Another limitation of the velocity-weakening effect model is the necessity of stick-slip downhole data to adjust the parameters of the prescribed functions [36], [37].

In spite of the advantages presented by Detournay and Defourny's approach, parameter acquisition for this bit-rock model remains as a challenge as many assumptions need to be made. Furthermore, in these investigations laboratory or field drilling tests have only been performed for drilling parameter acquisition. Model simulation results have not been compared to field or laboratory drilling results in order to validate the model. This is a topic that needs to be addressed.

2.4. Bond Graph Modeling

In this thesis, the bond graph method is used for mathematical modeling of the drilling system. A bond graph can be described as a representation of subsystems that are linked together by power bonds [38]. Power is the product of flow and effort in a system, thus the power bonds relate the linked subsystems with efforts and flows. When modeling different physical systems, flow and effort may have different definitions and physical dimensions. The power however, namely the product between them, will be the same.

For example, in a mechanical system flow is defined as the velocity with dimension $[L][T^{-1}]$, while in hydraulic systems flow is given by the volumetric flow rate whose dimension is $[L^3][T^{-1}]$. However, when multiplying each flow by their respective effort, the resultant mechanical power and hydraulic power have the same dimensions: $[M][L^2][T^{-3}]$ [39]. Here lies the main advantage of bond graphs, that the same approach can be used for multi domain systems.

Bond graphs were created in the 1950s by Professor Henry Paynter. He believed that energy and power were sufficient and fundamental dynamic variables that allowed all physical interactions. His effort to develop generalized concepts and to graphically capture the electric circuit diagram notion, led him to develop the first representations of power interaction. In his early bond graphs, bonds were represented with a single line but without the operating rules of power direction and causality that are known nowadays [40]. The bond graph notation was further developed by Dean Karnopp in the 1960's with the incorporation of a half arrow to represent positive orientation of the power bonds [41].

2.4.1. Bond Graph Theory

(i) Elements, Bonds and Ports

In bond graphs, every element that constitutes the system can be connected to other elements through bonds that represent the transfer of power variables. The link between an element and each of its bonds is called a port. If the bond carries both power variables, namely effort and flow, it is called a power bond and it is shown as a line with a half arrow (see Figure 2.9). The positive direction of the power is defined by the direction of this arrow [42]. On the other hand, if the bond only carries a single variable, it is called an active bond. his means that the node is receiving either an effort or a flow variable but with negligible power so, there will be no back effect. Active bonds are symbolized with a full arrow [38].

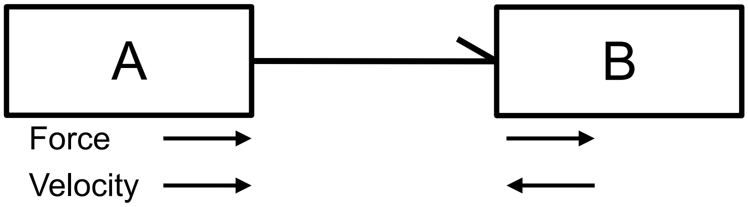

Figure 2.9. Two elements of a system linked by a power bond

Because the notation of power variables changes along different domains, it is necessary to introduce a common language to avoid confusion. Table 2.1 presents the generalized variables used in bond graphs and their common notation for a mechanical translation and rotation system.

Table 2.1. Generalized variables used in bond graphs [38]

Generalized Variables	Mechanical Translation	SI Units	Mechanical Rotation	SI Units
Effort, e	Force, F	Newtons (N)	Torque, τ	newton-meters (N-m)
Flow, f	Velocity, V	meters per second (m/s)	Angular velocity, ω	radians per second (rad/s)
Momentum, p	Momentum, P	N-s	Angular momentum, p_τ	N-m-s
Displacement, q	Displacement, X	m	Angle, θ	rad
Power, P	$F(t)V(t)$	watts (N-m/s = W)	$\tau(t)\omega(t)$	N-m/s = W

The elements in bond graph modeling are classified according to the maximum amount of ports they have. The basic bond graph elements with their constitutive equations, as well as an example of each element in the mechanical domain are summarized in Table 2.2.

Table 2.2. Elements in bond graph. Modified from [39]

Element	Symbol	Constitutive relation (linear relation)	Mechanical example
Resistor	$\longmapsto \mathrm{R}$ $\longrightarrow\!\!\mid \mathrm{R}$	$e = Rf$	Damper
Capacitor	$\longmapsto \mathrm{C}$ $\longrightarrow\!\!\mid \mathrm{C}$	$e = \frac{q}{C}$	Spring
Inertia	$\longrightarrow\!\!\mid \mathrm{I}$ $\longmapsto \mathrm{I}$	$f = \frac{p}{I}$	Mass
Source of Flow	$S_f \longmapsto$	$f = f(t)$, given $e(t)$, arbitrary	Prescribed velocity source
Source of Effort	$S_e \longrightarrow\!\!\mid$	$e = e(t)$, given $f(t)$, arbitrary	Imposed Force
Transformer	$\overset{1}{\longmapsto} TF \overset{2}{\longmapsto}$ $\overset{1}{\longrightarrow\!\!\mid} TF \overset{2}{\longrightarrow\!\!\mid}$	$e_1 = me_2$ $f_2 = mf_1$ $e_2 = e_1/m$ $f_1 = f_2/m$	Rigid lever
Gyrator	$\overset{1}{\longmapsto} GY \overset{2}{\longrightarrow\!\!\mid}$ $\overset{1}{\longrightarrow\!\!\mid} GY \overset{2}{\longmapsto}$	$e_1 = rf_2$ $e_2 = rf_1$ $f_2 = e_1/r$ $f_1 = e_2/r$	Gyroscope
1-junction	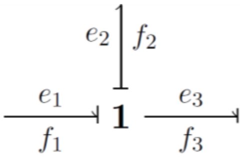	$e_1 - e_2 - e_3 = 0$ $f_1 = f_2 = f_3$	Geometric compatibility
0-junction	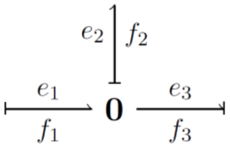	$e_1 = e_2 = e_3$ $f_1 - f_2 - f_3 = 0$	Dynamic equilibrium of forces (Newton's Law)

It is important to acknowledge that physical systems may not exhibit linear behavior at all times; although linearization is a common modeling simplification method to avoid simulation difficulties, non-linear modeling is often necessary. This can be achieved in bond graphs by changing the constitutive linear relation of the element to the desired non-linear function. When doing this, care must be taken to properly use the inverse function and to avoid indeterminations such as divisions by zero.

(ii) Causality Considerations

With a closer look at the symbols of Table 2.2, it is possible to see an orthogonal mark on each bond. These are called causal strokes and define which of the effort and flow signals at a port is the input. The element on the causal stroke's side receives effort as an input from that bond. Consequently, the element on the other end receives flow as an input variable. Note that the position of the stroke is independent of the arrow direction [38].

Some elements, such as sources of flow and effort, have only one causality option by definition; other elements have a preferred integral causality, this means that a certain variable input is preferred in order to avoid numerical differentiation during equation solving. In some cases, causality can be chosen arbitrarily. Finally, multiport elements can have causal constraints between their ports. Examples of this are the 1 and 0- junctions: only one flow out at a 0-junction and only one effort out at a 1-junction is possible. In transformers, only one effort out or one flow out is allowed, and in gyrators both bonds must be either effort out or flow out [41].

2.4.2. Modeling Mechanical Systems using Bond Graphs

Mechanical systems are frequently composed of elements such as masses, springs, dampers, levers, gears, shafts, and so forth. When modeling a mechanical system, it is necessary to identify the elements and to relate their energy and power characteristics to the basic bond graph elements, to put together the components, and to appropriately represent the kinematics of the system [38].

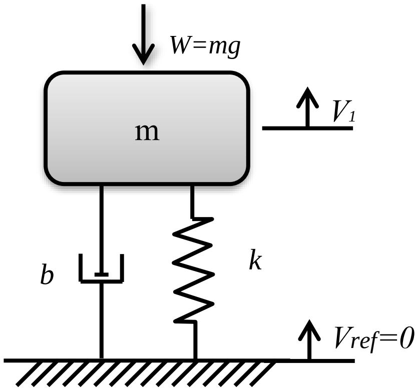

Figure 2.10. Mass-spring-damper element.

For mechanical systems, force is the effort variable and absolute velocity is the flow variable. A simple way to construct a mechanical system bond graph is to represent the system velocities with 1-junctions, and develop the appropriate relative velocities with 0-junctions in between [38]. The system elements can be attached to 1-junctions and 0-junctions according to their velocity. Figure 2.10 shows a mass-spring-damper system. The mass *m* is subjected to the force of gravity *W* and attached to the ground through a spring with constant *k* and damper of constant *b*.

Figure 2.11a shows an initial bond graph of the mass-spring-damper system. The elements moving with V_1 are attached to the V_1 1-junction, these are the mass and the weight. The ground is identified with a velocity as well and a source of flow that enforces the constraint of zero velocity is connected to it. The spring and damper are both moving with a relative velocity between the mass and the ground so they are attached to 0-junctions between the 1-junctions, this can be seen in Figure 2.11b. The direction in the arrows is set so that the extension of the elements yields a positive value.

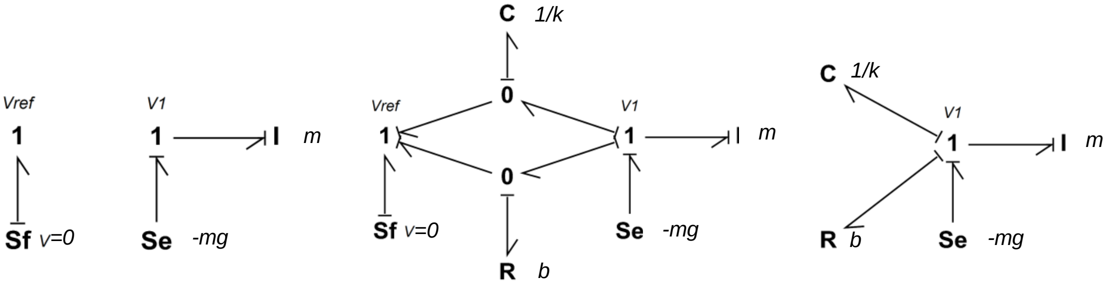

(a) (b) (c)

Figure 2.11. Bond graph construction for mass-spring-damper system.

Finally, a simplification is made by eliminating the ground velocity. The spring and damper end up subjected to one absolute velocity and are attached to the V_1 1-junction.

By following the previous approach, chapter 3 will further detail how a simple rotary drilling system can be modeled with the bond graph technique. This is done by defining the inertial elements, the compliant elements, the energy dissipation phenomena such as friction or damping, and the gravity acting on these elements. Torsional dynamics can be modeled in a similar fashion by considering the angular velocities as flows and torques as efforts.

CHAPTER 3

NUMERICAL FORMULATION OF DRILLING SYSTEM

A drilling system is comprised by two main subsystems: the rig that controls the drilling parameters and the drillstring that provides downward force and transfers the rotary motion to the bit. It is not in the scope of this research to analyze the way in which the rig supplies rotation or controls the input parameters. Therefore, modeling of the rig system will be limited to an imposed set of parameters as a top boundary condition for the drillstring. At the other end of the drillstring, the bit interacts with the formation and produces the desired drilling. This is considered as the bottom boundary condition for the drillstring subsystem. Due to the complexity and relevance to this research, the bit-rock interaction will be considered as a subsystem itself.

3.1. Drillstring Model

This section relates the characteristics of a drillstring to the basic mechanical elements described in the bond graph technique in order to create a simplified model. The axial and torsional dynamics are modeled individually. Coupling between these two modes will be given with the bit-rock interaction model described in section 3.2.

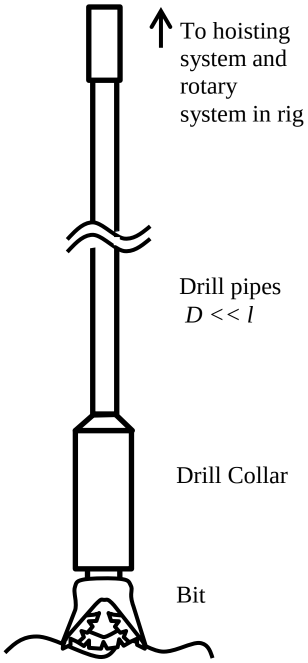

Figure 3.1. Drillstring schematic picture.

Figure 3.1 shows a common drillstring arrangement. Although not shown to scale, the diameter-to-length ratio of the drill pipes section is extremely small. Therefore, if the applied forces are within the elastic range of the pipe material, the drill pipe will act as a flexible element. This is modeled as a spring, both in torsional and axial modes. Reduction of the entire drillstring to a spring instead of a continuous approach is justified by the premise that, torsional vibrations in a drillstring are dominated by the first natural frequency [28], [43]. The spring constants, also known as drillstring stiffness, are obtained from:

$$k_{axial} = \frac{l_p}{EA_p} \tag{3.1}$$

$$\boldsymbol{k_{torsional}} = \frac{\boldsymbol{l_p}}{\boldsymbol{GJ}} \tag{3.2}$$

where

E Young's modulus of pipe;

A_p Cross sectional area of the drill pipe;

l_p Length of the pipe;

G Shear modulus pipe;

J Area moment of inertia of the cross section.

Compared to the drill pipes, the drill collar is much shorter and much heavier. This provides the necessary WOB, but also incorporates an inertial dynamic effect. The inertia for axial dynamics is the mass of the element and for torsional dynamics is the mass moment of inertia.

For the drillstring model, a vertical borehole is assumed. As mentioned in the previous chapter the bit rock-interaction provides coupling between axial and torsional vibrations, therefore only these two modes are analyzed and lateral vibrations are not included in the model. Additionally, in order to study only the effect of bit-rock interaction in torsional vibrations, no contact or friction between the drillstring and the borehole is considered. On the other hand, structural damping of the drillstring and viscous damping due to mud circulation is neglected. This is justified by the low contribution of these phenomena to the total damping of the system compared to the damping due to frictional and cutting processes occurring at the bit-rock interface [44][45].

The top boundary conditions are set as fixed for the torsional mode and free for the axial mode. For a typical drilling rig, a constant speed is desired and the driving unit adjusts its output torque by means of a feedback controller. This system is idealized as a constant angular velocity supplier. For the axial condition a downward constant force, that accounts for the applied weight-on-bit (WOB_o), is set. Figures 3.2a and 3.2b show the axial and torsional simplification and the coordinates used. U and V represent the bit axial position and velocity; they are considered positive downwards. θ and Ω, measured in the counter-clockwise direction represent the bit angular position and velocity.

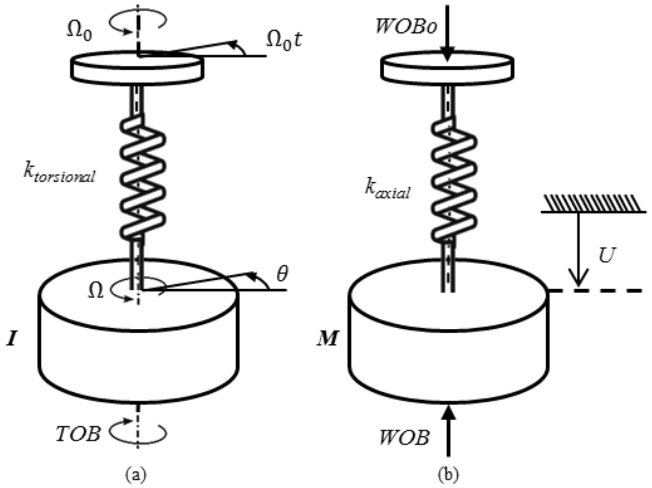

Figure 3.2. Drillstring model simplification (a) Torsional model (b) Axial model.

The torsional and axial models of the drillstring can be modified for specific purposes. In this investigation two variants of this model are considered. The first one is based on a previous drillstring model by Richard *et al* [28] that neglects axial compliance. This choice is justified by the selection of a free axial boundary condition for the drillstring top.

The second variant of the drillstring model is developed by considering the physical characteristics of a laboratory scale drilling apparatus used for experimental validation in this investigation. The main characteristic of this apparatus is a short and rigid drillstring and the inclusion of an axial compliance tool. These premises suggest the use of a drillstring model that is torsionally rigid but axially compliant. In this case, the axial compliance is not given by the elastic properties of the pipe, but by the spring constant of the compliant tool. For a more detailed description of the lab scale apparatus, refer to section 5.1.

Variant 1 of the drillstring model is primarily used to confirm if implementation of the bit-rock interaction model could be done with the available simulation tools, and to evaluate the best way to simulate the model using bond graph modeling. However, in order to obtain the parameters to validate the bit-rock model application, variant 2 was necessary.

3.1.1. Bond Graph of Drillstring

Figure 3.3 shows the Bond Graph for variant 1 of the drillstring model. The 1-junctions in the top of the model represent the angular velocities of the top of the drillstring (Ω_o) and the bit (Ω). There is a relative velocity between them due to compliance introduced by the torsional spring, this is symbolized by the 0-junction and the C element attached to it. The C element parameter is governed by equation 3.2. The bottom row represents the axial motion; the 1-junction accounts for the axial velocity at the bit (V), which is assumed to be the same along the drillstring. The source of effort represents the downward force applied to the system by the BHA weight (WOB_o).

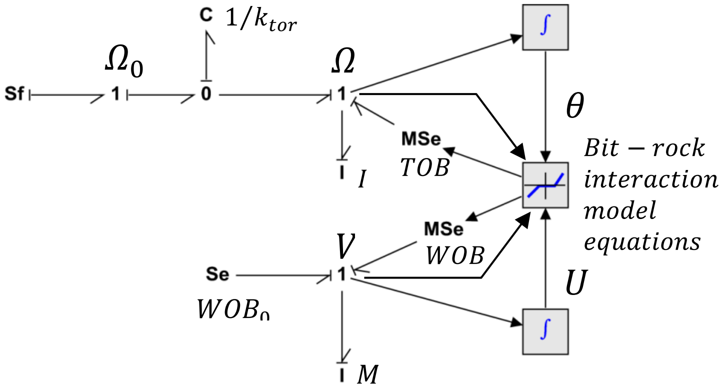

Figure 3.3. Bond graph model of variant 1 of drillstring.

In the bond graph shown in Figure 3.3, both axial and torsional dynamics have an inertia element acting at the bit axial and angular velocity. For the axial velocity, the inertia parameter is the BHA mass and for the torsional dynamics, the inertia parameter is the BHA mass moment of inertia. Finally, the reacting forces are applied at the bit as modulated sources of effort. The output of the sources is dependent on variable modules that will be defined later in the bit-rock interaction model. Note that axial and torsional dynamics are modeled separately and coupling is given by the bit-rock interaction.

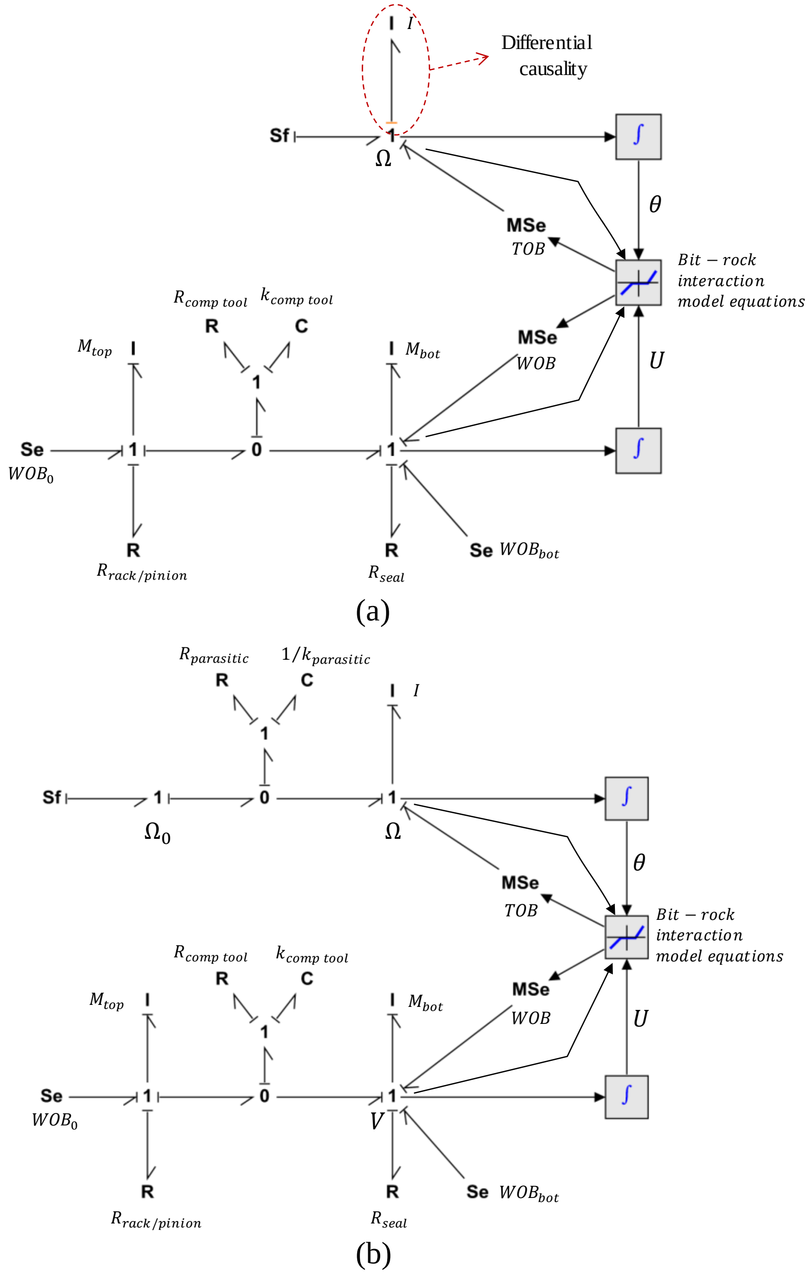

Figure 3.4. Bond graph model of variant 2 of drillstring (a) With differential causality (b) Differential causality solved by adding parasitic elements.

Figure 3.4a shows an initial bond graph for variant 2 of the drillstring model. In this bond graph, the torsional dynamics are defined by one angular speed (Ω) imposed by the source of flow. Note that this imposed velocity introduces a non-preferred differential causality in the inertia element. This can be solved by applying a method detailed in [46], which consists in adding a parasitic compliance and resistance element in order to avoid the non-preferred causality. Figure 3.4b shows the resultant bond graph with the introduction of the parasitic elements.

The axial dynamics in variant 2 are defined by two distinct velocities: V_o is the axial velocity of the top of the drilling rig and V the bit axial velocity. The relative motion between these two elements is governed by the compliant tool. In this case there is a C element that represents the compliance given by the springs of the tool and an R element that represents the energy dissipation (damping) given by the tool rubber elements. Two R elements are introduced in this model. The first one, attached to the V_o 1-junction, represents the friction between the pinion and rack where the top section is attached to. The second one, acting at V, is the friction between the bottom of the drillstring and the drilling cell seal. Further details on the lab scale drilling apparatus and parameters calculation will be given in chapter 5. The *WOB* and *TOB* effort sources are modeled in the same way as in variant 1.

3.2. Bit-rock Interaction Model Formulation

The bit-rock interaction model presented in this research is based on a model by Detournay and Defourny [31], later modified by Richard *et al* [32] to include the determination of friction forces and calculation of depth of cut from the state variables.

The present model is based on the following premises: (i) There are two surfaces in the bit that produce reaction forces: the cutter face that produces purely the cutting action and a flat surface under the bit responsible for the friction. Each of these processes contributes to *WOB* and *TOB*. (ii) The decrease of *TOB* with angular speed is not an intrinsic property of the bit-rock interface. Therefore, this effect is not modeled as an input. (iii) The reaction forces on a single cutter depend on the path that the previous blade has left behind. This assumption suggests a history-dependent nature of the bit-rock interaction.

Equations 3.3 and 3.4 summarize the proposed model for the generalized forces acting on a drill bit when the effects from the individual cutters are integrated. *TOB* and *WOB* are decomposed into friction forces designated with the subscript *f* and cutting forces denoted by the subscript *c*. Note that the second term of each equation (friction component) is dependent on the total length of the wearflat surface (*l*) and that the cutting component is dependent on the portion of the cutter that is in contact with the rock at a certain time, this is the instantaneous depth of cut (*d*). Note also that these equations are only valid when both the cutter face and the wear flat surface are in complete contact with the formation.

$$TOB = TOB_c + TOB_f = \frac{\varepsilon d a^2}{2} + \frac{a^2 \gamma \mu l \sigma}{2} \tag{3.3}$$

$$WOB = WOB_c + WOB_f = \zeta \varepsilon a d + a l \sigma \tag{3.4}$$

where,

ε	Rock intrinsic specific energy;
d	Instantaneous depth of cut;
a	Drill bit radius;
γ	Orientation and spatial distribution of the frictional contact surfaces associated with the cutters;
μ	Coefficient of friction of the rock;
l	Total wearflat length;
σ	Maximum contact pressure at the wearflat/rock interface;
ζ	Orientation of the cutting reaction.

3.2.1. Determination of Instantaneous Depth of Cut for a PDC Bit

Figure 3.5 shows a section of two successive blades of a drill bit symmetrically distributed around the axis of revolution. The blades are considered to be identical and regularly spaced by an angle of $2\pi/n$ where n is the total number of blades in the bit. Each blade is characterized by a cutting surface and a chamfer that is orthogonal to this surface. When the bit is drilling, depth of cut (d) is assumed to be constant along the blade and identical for each blade.

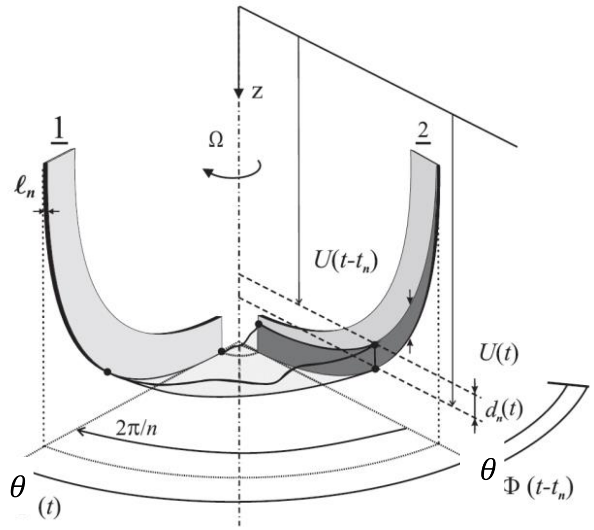

Figure 3.5. Schematic picture of 2 successive blades on a PDC bit. [28]

The instantaneous depth of cut (d) integrates the effect of forces of all individual cutters by the following equation:

$$d = nd_n \tag{3.5}$$

where d_n is the depth of cut per blade.

The term d_n is the depth of rock layer in front of the cutter. Based on this, the depth of cut per blade is calculated by:

$$d_n = U(t) - U(t - t_n) \tag{3.6}$$

where,

$U(t)$ Current axial position of the blade;

$U(t - t_n)$ Axial position of the blade at a previous time.

The previous time $(t - t_n)$ described in equation 3.6 is determined by a time delay t_n. This is the time that the blade takes to rotate an angle of $2\pi/n$. For a double cutter PDC bit, the time delay (t_n) is calculated by obtaining the delay angle value from the angular motion history and then its corresponding time (see equation 3.7)

$$\theta(t) - \theta(t - t_n) = \frac{2\pi}{n} \tag{3.7}$$

3.2.2. Bit-rock Interaction Cases

Equations 3.3 and 3.4 are only applicable if there is full contact between the bit surfaces and the rock. This section describes the possible cases of contact loss and how this model addresses the change in reaction forces for each case.

(i) Case 1: Loss of Contact between Wear Flat and Surface

When the axial velocity is negative ($V<0$), the frictional components acting at the wearflat disappear. This is captured in the friction terms with the inclusion of a sigmoidal function to avoid discontinuity problems in the transition zone ($V=0$). Equation 3.8 shows the sigmoidal function used. Constants c_1 and c_2 have been set to -20e4 and -1.5 respectively. c_1 was calibrated by varying the values until obtaining the minimum transition zone without introduction of instabilities in the model simulation. c_2 was obtained in a similar manner, to reduce the value of the function to 0 when $V<1$.

$$S(V) = \frac{1}{1+e^{(c_1 V + c_2)}} \tag{3.8}$$

(ii) Case 2: Complete Loss of Contact

If V is negative for enough time to allow for a complete loss of contact between the bit and the rock (bit-bounce), depth of cut becomes zero or negative. In this case the cutting components vanish. This is captured by a similar sigmoidal function in WOB_c and TOB_c.

$$S(d) = \frac{1}{1+e^{(c_1 d + c_2)}} \tag{3.9}$$

(iii) Case 3: Stick-slip and Backward Rotation

If torsional vibrations are present, the bit might develop stick-slip. Experimental and field data show that the bit can rotate backwards in the presence of torsional vibrations [30]. If this occurs, even in the minimal case, the cutter face loses contact with the rock and the cutting components are vanished. Equation 3.10 is used for capturing this effect.

$$S(\Omega) = \frac{1}{1+e^{(c_1 \Omega + c_2)}} \tag{3.10}$$

In the case of backward rotation, the frictional forces must be negative; to account for a sign change and avoid zero or negative values when $\Omega \approx 0$, equation 3.11 is used:

$$F(\mathit{\Omega}) = tanh(c_3 \mathit{\Omega} + c_4) \tag{3.11}$$

In equation 3.11, c_3 and c_4 where calibrated in a similar manner as c_1 and c_2. In this case, $c3$ limits the transition period when $\mathit{\Omega} \approx 0$ and c_4 avoids having zero values at zero angular velocity.

The bit-rock interaction model described by the combination of Equations 3.3 to 3.11 is included in the general drillstring bond graph model as the reaction forces WOB and TOB occurring at the bit (see Figures 3.3 and 3.4) the required inputs for the bit-rock model, such as angular and axial velocity and position, are obtained from the drillstring model outputs. In order to use this model for prediction of the vibration response, the differential equations need to be solved, this is part of the computer implementation and will be discussed in the next chapter.

CHAPTER 4

SIMULATION ANALYSIS AND MODEL VERIFICATION

This section details the procedure for simulation of the drillstring and bit-rock interaction numerical model, and the analysis performed in order to verify the model implementation.

4.1. Solution of the Numerical System

In order to perform the dynamic simulation of the model, the system equations for the bond graph are derived (See Appendix A), these equations have the following shape:

$$\dot{x}(t) = Ax(t) + By(t) \tag{4.1}$$

In this equation, $x(t)$ are state variables and $y(t)$ are the known inputs. Both are functions of time.

Now considering that the input reactions of the bit-rock interaction model (*WOB* and *TOB*) are not known inputs, they cannot be included in $y(t)$. In equations 3.3 and 3.4 of the previous chapter, it can be observed that *WOB* and *TOB* are functions of the depth of cut (d), which is a variable that arises from comparing the current position of the bit $U(t)$ with a previous position $U(t-t_n)$. This implies that *WOB* and *TOB* are actually functions of the state variables history, this is denoted here as ${}_0^t x(t)$. The resulting system equations look like:

$$\dot{x}(t) = Ax(t) + By(t) + C\,{}_0^t x(t) \tag{4.2}$$

A system composed by equations such as Equation 4.2 represents a system of delayed differential equations (DDE), in which the derivative of the state variables is given in terms of a function of the state variables at previous times [47]. In addition, the delay in this system is not constant but depends on the state variables as well. In order to simulate this numerical model with ordinary differential equation (ODE) numerical methods, the third term of equation 4.2 needs to be solved separately from the state variables history. The next section describes a proposed method for this implementation.

4.2. Co-simulation of Bit-rock Model and Drillstring Model using 20-Sim/Matlab

The implementation of the drillstring and bit-rock model involves co-simulation of the system by two different software programs. In co-simulation, every subsystem that forms a coupled system is simulated in a different manner. Since the elements are connected, there is a communication pattern between them. Figure 4.1 shows how the output variables from the drillstring model simulation are input to the bit-rock model simulation and the latter feeds back the former with the reaction variables (*WOB* and *TOB*). Both simulations are run simultaneously in different software programs. The drillstring system is simulated using 20-sim [48] with an Euler-forward finite differences scheme. A constant step size of 1^{-5} s was used in order to avoid numerical instabilities resulting from the rapid change of *d*. By using 20-sim for the drillstring model, change of drillstring configuration, inclusion of any other distributed load, and change of the top boundary conditions can be easily performed with the system equations being automatically regenerated by the software program.

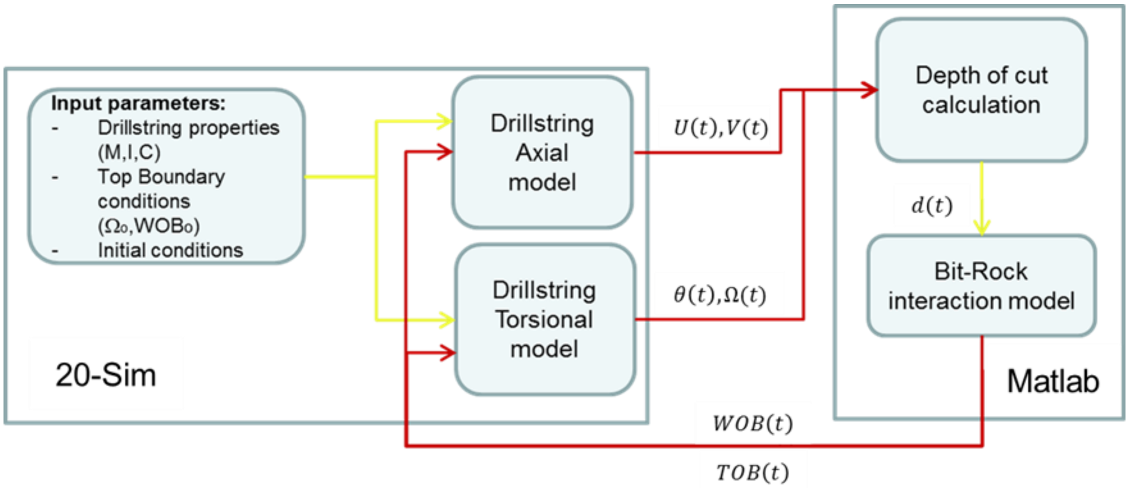

Figure 4.1. Model co-simulation using two software programs.

In addition, the bit-rock model is solved with a numerical solver such as Matlab [49]. During the simulation, the drillstring model outputs are kept in the time history. The time delay and axial position of the bit at the delayed time are found by interpolating the time history of the variables.

4.3. Model Verification

In modeling, verification and validation is performed in order to increase confidence in the model rather than demonstrating its absolute accuracy [50]. Although there is a common ultimate goal in both processes, the implications of verification and validation are different. Verification is the process of ensuring that the design of the model has been captured by the computer implementation with sufficient accuracy [51]. Validation refers to confirming that the model is accurate enough for the required purpose [52].

Verification implies confirmation that the physical laws, the observed phenomena, and the initial assumptions are being captured in a logical and systematic manner. A good example of this is modeling a free falling object. Verification would imply to ensure that the object actually goes down and accelerates as it falls. Confirming that the object hits the floor with the same speed and force as a real life object would be part of the validation process.

Some verification methods are: checking the code to ensure the right data and inputs, running the model and analyzing the behavior of each element according to the expected behavior, modifying the initial conditions to force certain events, and comparing the model against other simulation models of a similar system [50]. Some mathematical errors made during the model implementation can yield the correct answer for erroneous reasons. Therefore, verification should be performed to a sufficient level before the validation activity begins [53].

4.3.1. Verification against Similar Models

Table 4.1 shows the parameters used to perform verification against the model presented in [32]. This model is formulated in a dimensionless form with a set of scaled parameters. Therefore, it is not possible to compare the numerical results directly. In this case, verification was performed by corroborating that changes in the main input variables reflect similar behavior to those reported in [32].

Table 4.1. Parameters used in simulations 1 to 6

Parameter	**Simulation**					
	1	**2**	**3**	**4**	**5**	**6**
Ω_o (rad/s)	63.83	21.28	19.15	21.28	21.28	21.28
WOB_o (N)	76 900	76 900	76 900	30 000	50 000	90 000
M (Kg)	25 000	25 000	25 000	25 000	25 000	25 000
I (Kgm^2)	103.8	103.8	103.8	103.8	103.8	103.8
k_{tor} (Nm/rad)	470	470	470	470	470	470
ε (Mpa)	60	60	60	60	60	60
a (m)	0.108	0.108	0.108	0.108	0.108	0.108
ζ	1.1	1.1	1.1	1.1	1.1	1.1
γ	1	1	1	1	1	1
μ	0.25	0.25	0.25	0.25	0.25	0.25
σ (Mpa)	2.67	2.67	2.67	2.67	2.67	2.67
l_n (m)	0.005	0.005	0.005	0.005	0.005	0.005
n	6	6	6	6	6	6

Evolution of bit angular velocity for simulations 1 to 3 is shown in Figure 4.2. It is observed that the magnitude of the imposed angular velocity can strongly affect the development of torsional vibrations, as a slight decrease of angular velocity leads to stick-slip.

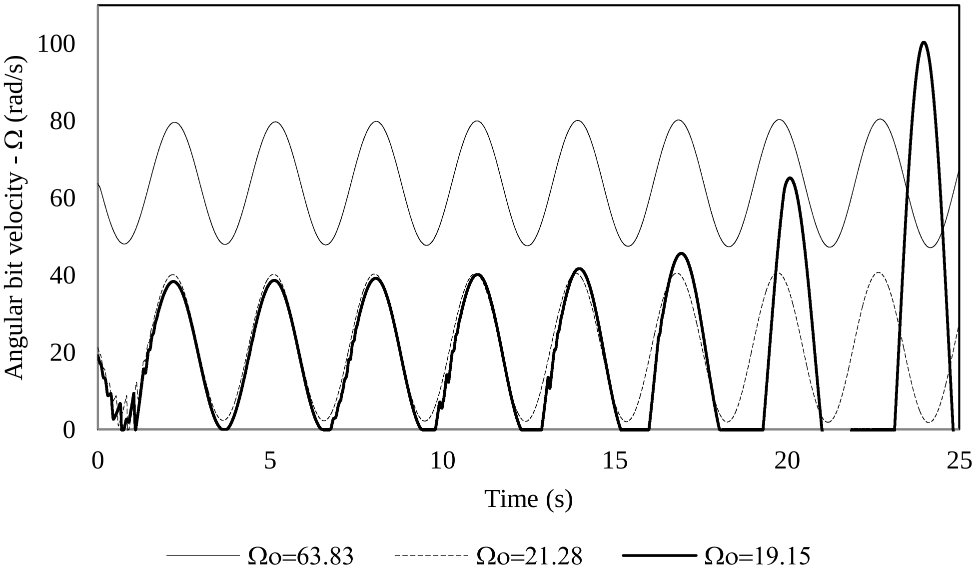

Figure 4.2. Influence of Ω_o in the development of stick-slip vibrations

Figure 4.3 shows a zoomed section of angular and axial velocity during stick phases of simulation 3. In this Figure, the coupling nature of the bit-rock interface can be observed. When the bit sticks ($\Omega \approx 0$), all the energy from the torsional motion is transferred to the axial motion and bit-bounce is developed. During bit-bounce, there is no friction torque reaction. Therefore, there is a dramatic increase in the amplitude of the torsional vibration when the bit abandons the stick slip phase. As a consequence of this, the severity of stick slip is also increased for the next cycle. These results are consistent with observations made in [32].

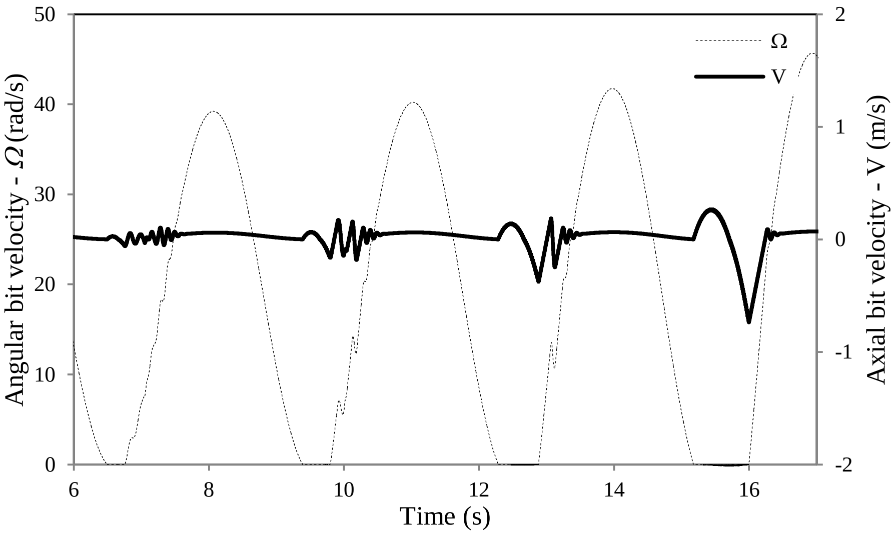

Figure 4.3. Angular and axial velocity during stick-slip

Simulations 4 to 6 evaluate the influence of applied weight in the torsional response. Similarly to previous models [32], as well as field observations [3], a decrease in the applied weight can eliminate stick slip oscillations (see Figure 4.4). Indeed, an increase of the *WOB* brings more energy in the pure cutting process, magnifying the self-excited vibrations [28].

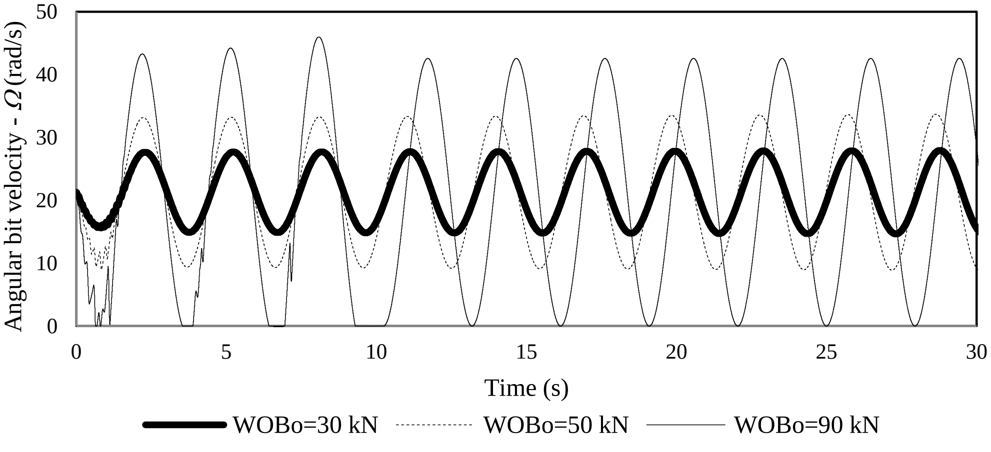

Figure 4.4. Influence of WOB_o on the development of stick-slip vibrations

4.3.2. Verification against Distinct Models

A different approach for the bit-rock interaction model was presented by [24], in which the reactions are composed of a static and a fluctuating component, and the fluctuating component is based on a prescribed sinusoidal function. For this reason, there is a lack of information about the bit-rock interface parameters. Some of these parameters were assumed to give similar results and the operational parameters and drillstring configuration were kept comparable, in order to make a qualitative comparison between this model and the present research Table 4.3 presents the parameters used for these simulations.

Table 4.2. Parameters used in simulations 7 to 9

Parameter	**Simulation**			
	7	**8**	**9**	**10**
Ω_o (rad/s)	11.6	14.7	11.6	35
WOB_o (N)	100 000	100 000	100 000	100 000
M (Kg)	87 000	87 000	87 000	87 000
I (Kgm^2)	415	415	415	415
k_{tor} (Nm/rad)	708	708	708	708
ε (Mpa)	303.03	303.03	151.52	151.52
a (m)	0.22	0.22	0.22	0.22
ζ (assumed)	1.5	1.5	1.5	1.5
γ (assumed)	1	1	1	1
μ	0.06	0.06	0.06	0.06
σ (Mpa) (assumed)	30.3	30.3	11.15	11.15
l (m) (assumed)	0.002	0.002	0.002	0.002
n (assumed)	6	6	6	6

Figure 4.5a shows the angular speed and depth of cut per revolution of simulation 7. Although the simulations presented in [24] considered axial compliance of the drillstring, the results in torsional motions are similar. Angular speed experiences large fluctuations

until reaching stick-slip vibrations. In the present simulations, the bit cutter remains in contact with the formation for the first 33 seconds. However after this, the torsional vibrations excite the axial mode and bit-bounce is developed. This is evidenced by negative values of *d*. Bit-bounce is not observed in [24], but the continuous increase in the WOB fluctuations presented in [24] indicates that this could be developed if the simulation was longer. In order to mitigate stick slip vibrations, simulation 8 is conducted with a higher angular speed. Figure 4.5b shows the results of this implementation. This approach is effective for decreasing the amplitude of the torsional vibrations and is consistent with the literature [3], [24], [28], [32].

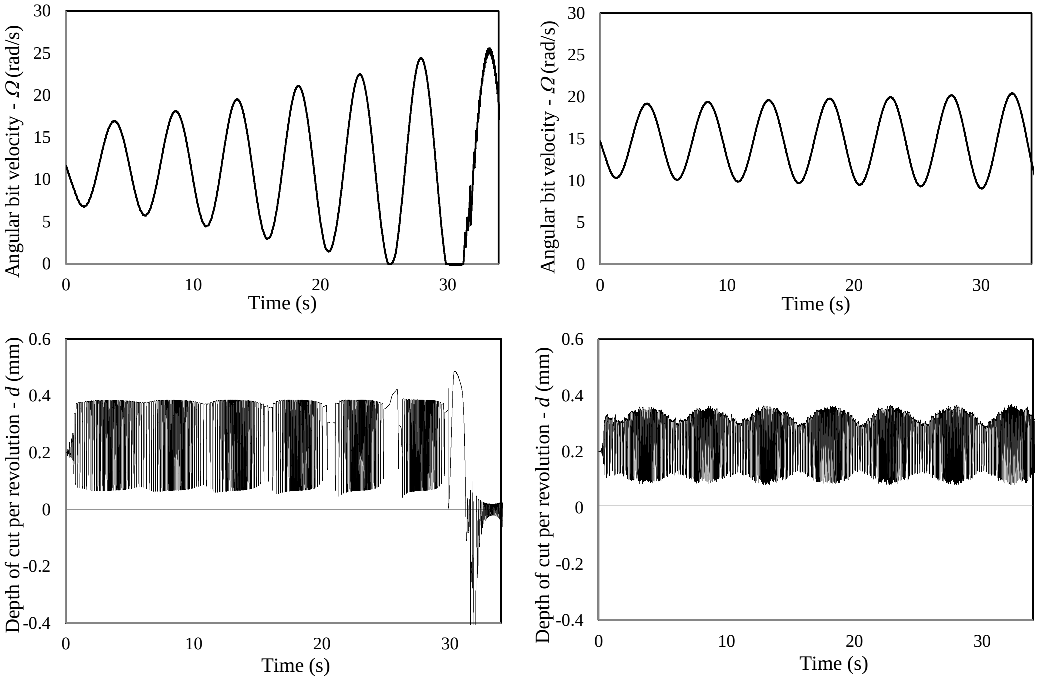

(a)

(b)

Figure 4.5. (a) Stick-slip vibrations (b) Stick-slip vibrations and bit-bounce mitigated by increasing the angular velocity

Simulations 9 and 10 are carried out in a softer formation. Once more, increasing the angular speed increases the time before torsional vibrations and stick slip occurs (see Figure 4.6). However in this case, a lower value of intrinsic specific energy (ε) and maximum contact pressure at the wearflat/rock interface (σ) is responsible for the development of bit-bounce vibrations which are not mitigated by the increase of angular speed. Both results are also consistent with those observed in [24].

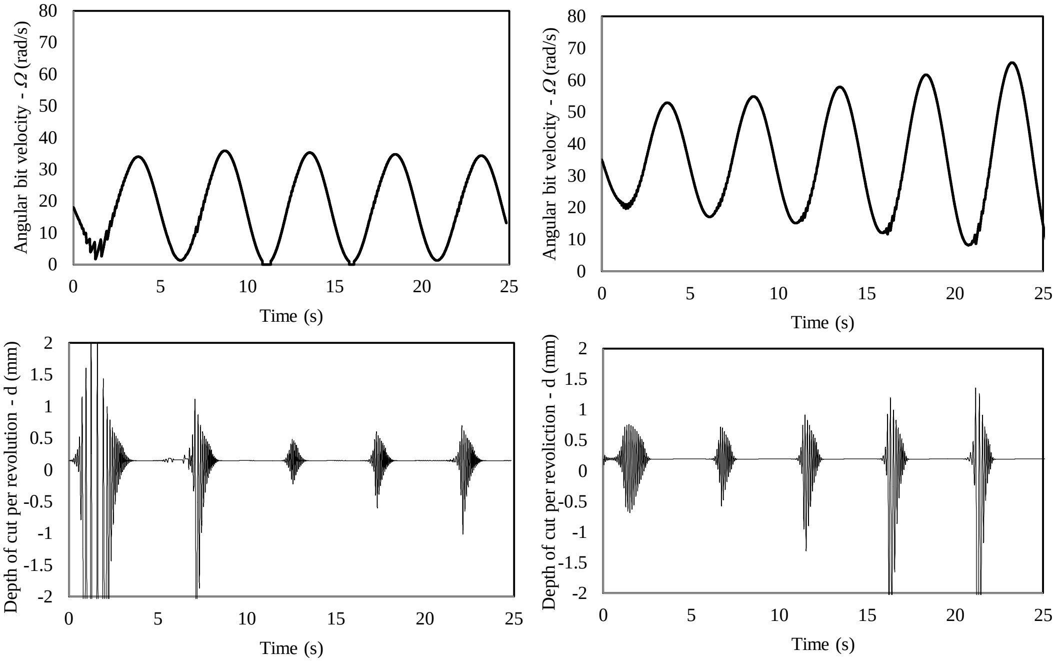

(a) (b)

Figure 4.6. (a) Stick-slip vibrations with bit-bounce (b) Stick-slip vibrations delayed by increasing the angular velocity

4.3.3. Influence of Bit-rock Parameters in Stick-Slip and Bit-bounce

It is clear that *WOB* and Ω_o are determinant factors in the development of vibrations [24], [3], [30]. It has also been shown that the properties of the drilled rock affect the development of bit-bounce vibrations. In this section, the bit-rock interaction parameters are analyzed in order to evaluate their influence on vibration severity.

(i) Bit Wear

The wearflat surface length (l_n) is a measure of wear in the bit. A sharp cutter exhibits no wearflat, while a worn cutter has a larger wearflat surface. Simulations with different states of bit wear were carried out in order to show the influence of bit wear in the development of vibrations, (See Figure 4.7).

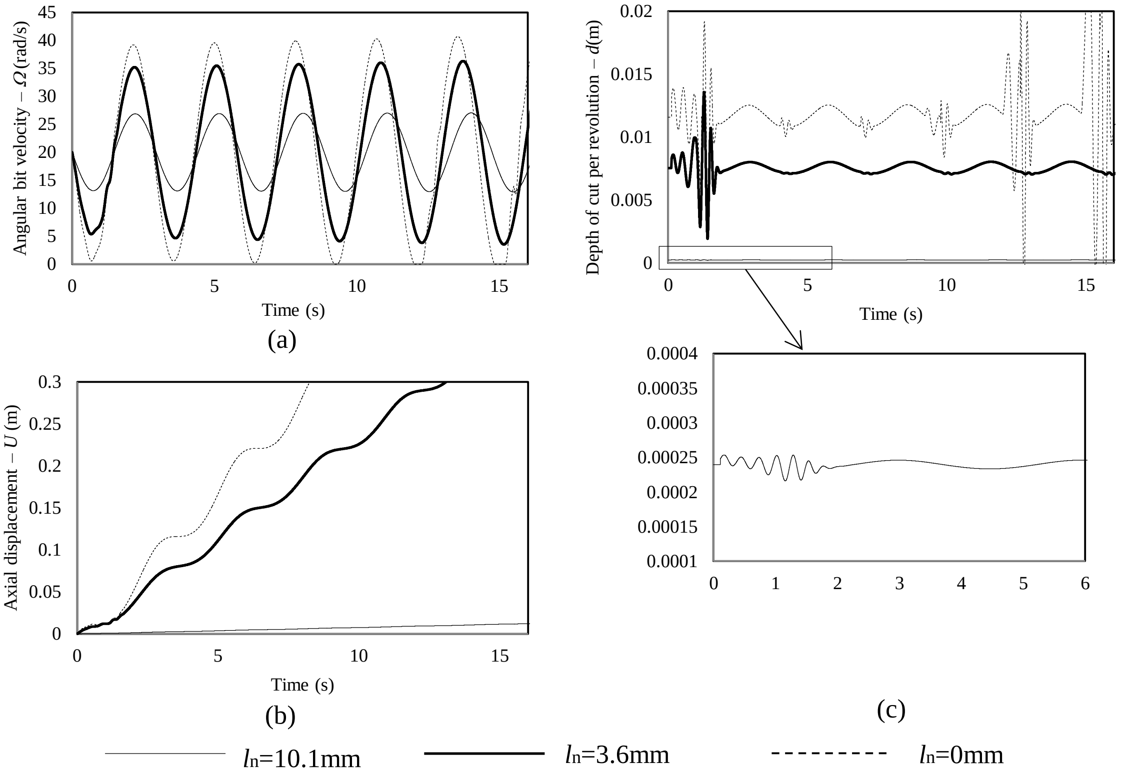

Figure 4.7. Simulation results for different states of bit wear. (a) Angular bit velocity. (b) Axial displacement. (c) Depth of cut per revolution.

Torsional vibrations are decreased as l_n increases (see Figure 4.7a). This is consistent with the explanation that frictional contact dampens self-excited torsional vibrations [32]. There is more energy dissipated by the frictional process components with a larger wearflat surface. In terms of vibration mitigation this is a good outcome, but also means that there will be less available energy for the cutting process. This in turn means lower drilling efficiency in terms of performance. To confirm this, average ROP values are calculated for each bit wear state from the slope of the axial displacement in Figure 4.7b. As expected, higher ROP values are obtained with a sharp cutter (see Table 4.3).

Table 4.3. Influence of l_n in drilling performance

Wear flat length l_n (mm)	**Average ROP (m/s)**
0	0.0303
3.6	0.0242
10.1	0.0008

(ii) Bit Geometry and Material

There are two bit-rock interaction parameters that depend on bit geometry and material, these are ζ and γ. ζ characterizes the orientation of the cutting forces [32]. It depends on the cutter angle and the friction coefficient between the cutter material and the formation [34]. On the other hand, γ is a bit geometry number (greater than 1) that characterizes the orientation and spatial distribution of the frictional contact surfaces associated with the cutters.

Previous investigations have defined β as the product of γ, ζ, and μ, where μ is the coefficient of friction [31], [28]. If β is greater than 1, the amplitude of torsional vibrations is reduced. Conversely if β is less than 1, torsional vibrations will be amplified until an eventual appearance of stick-slip [32]. Figure 4.8 show angular velocity and depth of cut for four simulations carried out with different values of ζ and β.

By comparing the different drilling regimes in Figure 4.8, it is possible to see that β>1 is a necessary but not a sufficient condition for stick-slip mitigation. Consistent with the literature, β dampens the torsional and axial vibrations. However, the term ζ affects the amplitude of these vibrations and the development of axial vibrations as well. Therefore if conditions are favorable (low Ω and high *WOB*), a higher value of ζ may lead to stick-slip vibrations. These vibrations will be self-sustained then by the development of other modes, such as bit-bounce. This can happen even if β is greater than 1 as in Figure 4.8b.

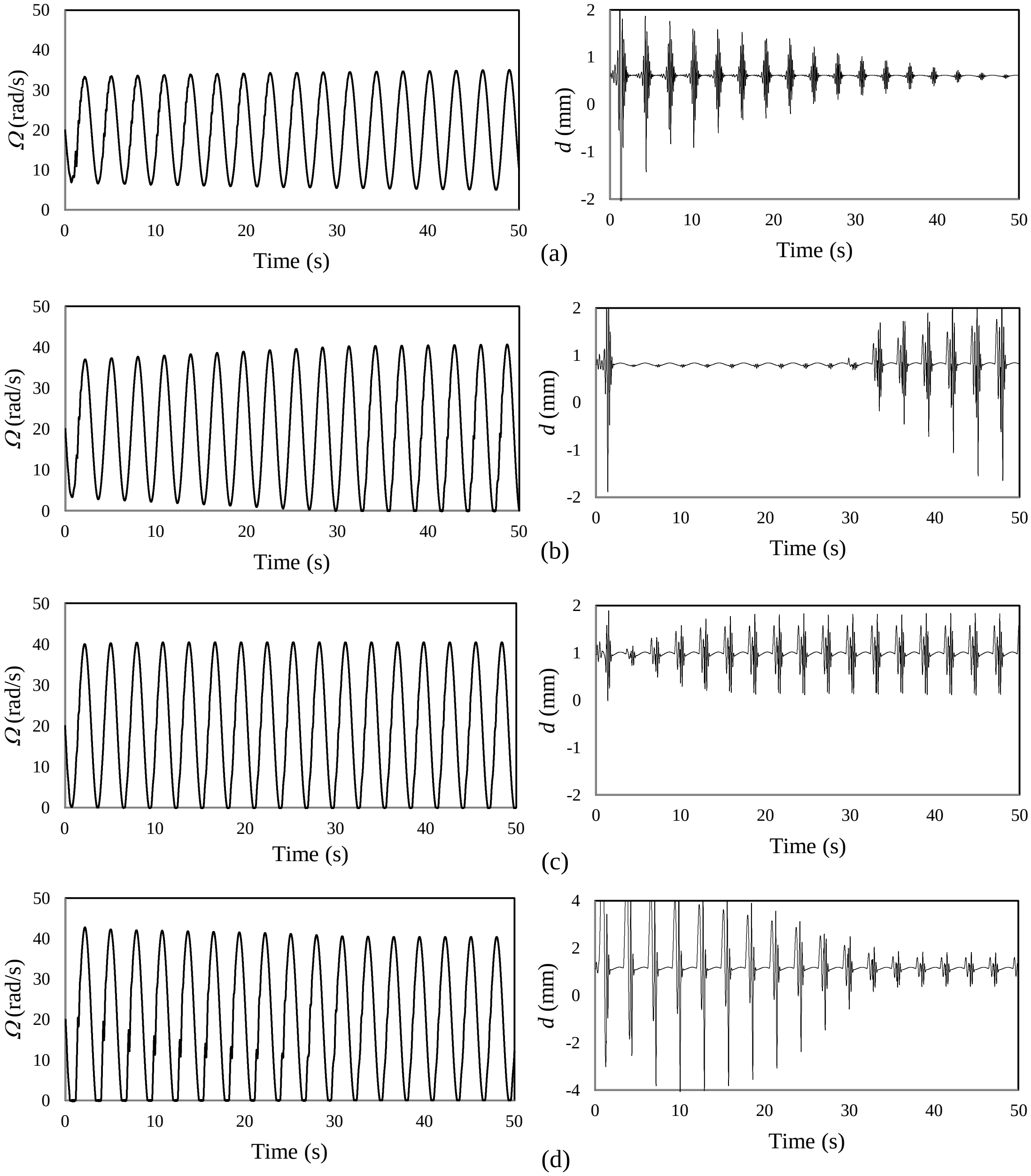

Figure 4.8. Influence of ζ and β in the development of torsional and axial vibrations.
(a) ζ=0.9, β >1. (b) ζ=1.2, β >1. (c) ζ=0.75, β <1. (d) ζ=1, β <1

4.3.4. Rate-independency Verification

One of the premises of the present model is the independency of frictional torque on angular speed. This model relies on the statement that; although the decrease of the average torque is a real effect observed in experimental tests and in the field, this is a consequence of the excited vibrations rather than a cause for them. Figure 4.9 shows the results of average torque from simulations carried out under different values of $\Omega_{o.}$

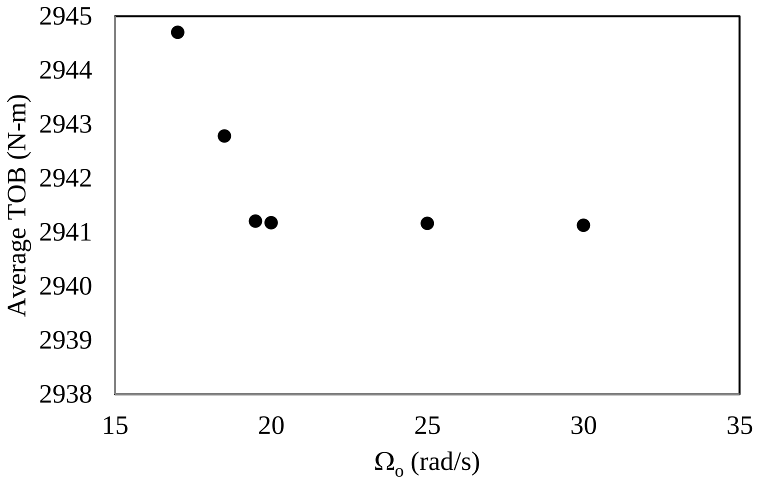

Figure 4.9. Evolution of average *TOB* with Ω_o

Although this premise was not included in the numerical model, the result of decreasing *TOB* with angular velocity is in agreement with the initial assumptions. Figure 4.10 shows the oscillations in depth of cut for these values of angular speed. By analyzing these figures, it can be confirmed that the increase of TOB with decreasing angular speed is closely related to an increase the axial vibrations that leads to intermittent losses of contact between the wearflat and the rock (d<0).

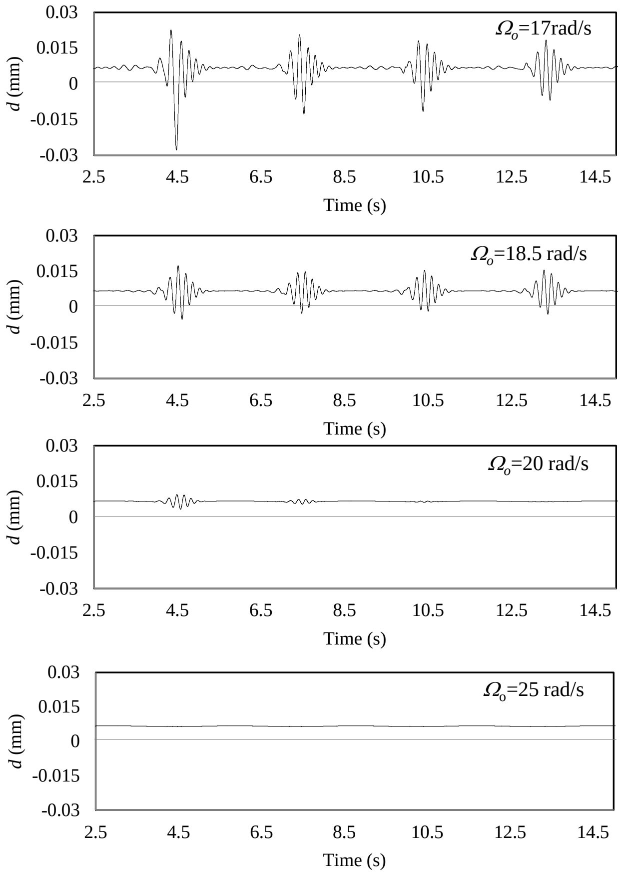

Figure 4.10. Increase of axial vibrations with reduced angular speed

Simulation results presented above, confirm that the design of the numerical model of a drillstring with bit-rock interaction was captured by the computer implementation with sufficient accuracy and yields expected results for known inputs. The next step for increasing confidence in the model is to compare simulation results with real drilling experiment results. This procedure is called validation and will be detailed in the next section.

CHAPTER 5

MODEL VALIDATION

Validation is the process of determining the degree of accuracy of a model against the real world. The goal of validation is to measure the predictive capability of the model by comparison of simulation results with experimental data and quantification of the error between them [52]. In order to validate the model presented in this investigation, an experimental drilling program was performed. The results were then compared with corresponding simulations of the system.

5.1. Experimental Test Setup

An existing laboratory drilling rig was used for the experimental tests. The drilling rig includes a rotary head, a loading system, a drilling fluid circulation system, a bottom-hole pressure cell, and a data acquisition system. Figure 5.1 shows a schematic illustration of the setup.

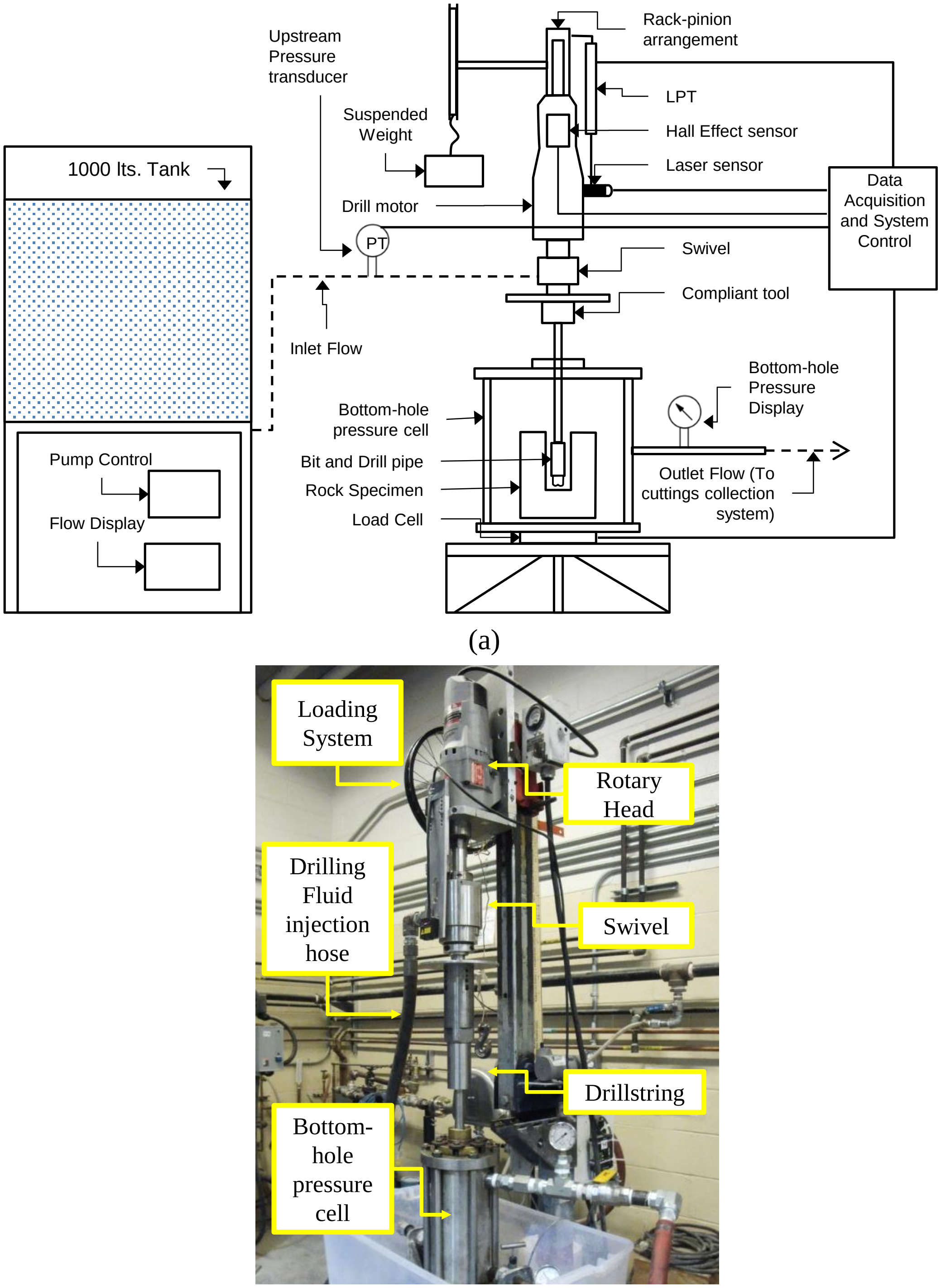

(a)

(b)

Figure 5.1. Schematic illustration and picture of the experimental test setup

The system is powered by a vertical motor that can travel along a steel column. The loading system provides a downward force to the motor by means of a rack-pinion arrangement and a suspended weight. Elements of the drillstring are shown in Figure 5.2. The swivel provides a way for fluid injection trough the drill pipe down to the bit nozzles, the compliant tool provides a relative motion between the top system and the drill pipe by a set of coned-disc springs and rubber damping elements, and the drill pipe connects the bit with the rest of the system. A two-cutter PDC drilling bit was used for the experiments. Details about the bit are given in Figure 5.3.

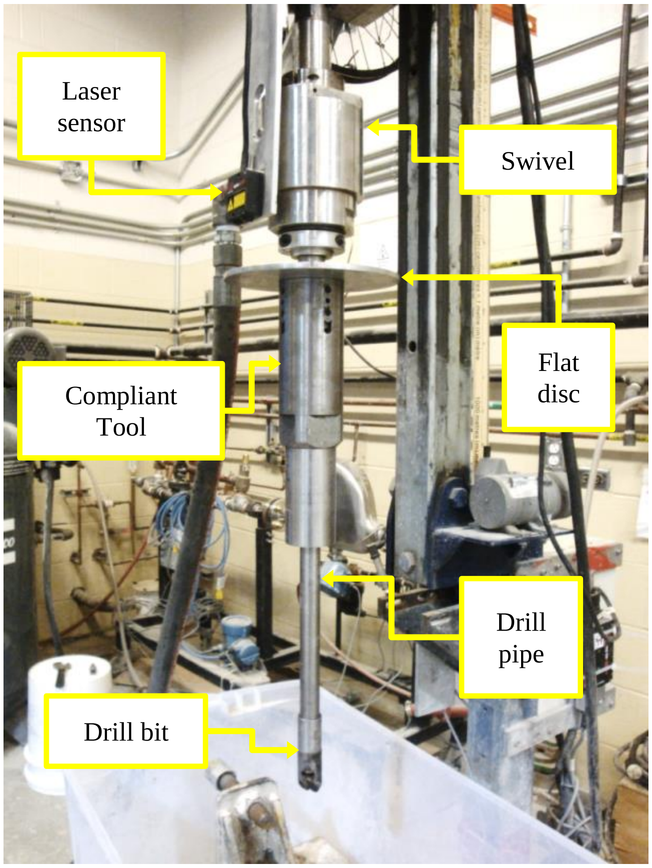

Figure 5.2. Elements of the drillstring

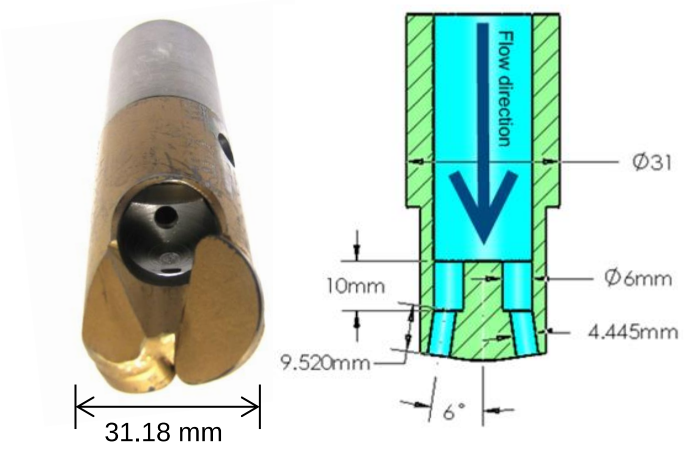

Figure 5.3. (a) Dimensions of drill bit. (b) Schematic figure of bit nozzle [55]

An enclosed cell is located at the bottom of the system. The cell holds the rock specimen in place and provides the required bottom-hole pressure. The drill pipe is inserted through the center of the upper cap of the cell where a rotary seal is placed to avoid leaks and to keep the drill pipe centered. Figure 5.4 shows the bottom-hole pressure cell.

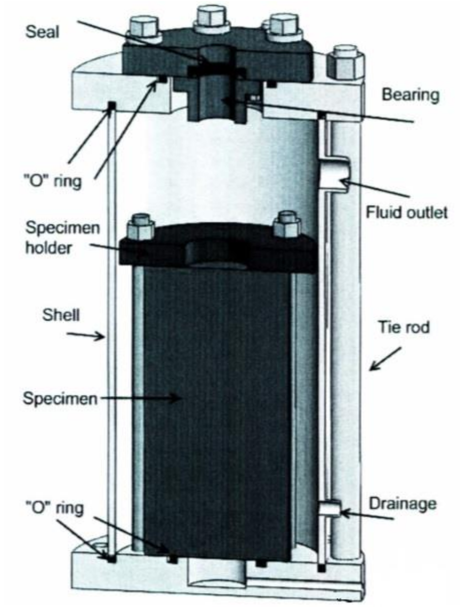

Figure 5.4. Bottom-hole pressure cell [55]

5.1.1. Sensors and Data Acquisition

The drilling system is equipped with a set of sensors that can record drilling parameters. Axial displacement of the motor head is measured by a draw wire linear position transducer (LPT). Relative displacement between the motor head and the drill pipe is measured by a laser triangulation sensor whose signal is reflected on a flat steel disc (see Figure 5.2). This sensor is also capable of providing data for angular velocity calculation by means of three grooves located on the steel disc. The system has a Hall Effect sensor in line with the electric motor for current measurements. The motor current is used to calculate the output torque (see Appendix B for details on torque calculation). Finally, a pancake-style load cell is placed under the drilling cell to measure the dynamic *WOB*. All data is recorded with a sampling rate of 1000Hz on a data acquisition (DAQ) system. This sampling rate is the minimum required to capture the peaks in the axial displacement signal coming from the grooves in the disc in order to calculate the angular velocity. More details about the sensors and DAQ system of the drilling rig can be found in [54].

5.2. Determination of Physical Parameters for Simulation

All the experimental equipment elements were analyzed in order to obtain the simulation parameters. Table 5.1 summarizes all the parameters required for the simulation and its values. Determination of the parameter values depends on their nature: direct parameters require only a straight forward measurement, input parameters depend on the input value used during the experimental test, and tuned parameters require preliminary experimental tests to obtain the value. Details of the preliminary tests are given in the next section.

Table 5.1. Parameters used in experimental tests

Parameter	Definition	Nature	Value	Unit
Ω_o	Imposed angular speed	Input	25-29	rad/s
WOB_o	Applied WOB	Input	330-1575	N
WOB_{TOP}	Weight of motor head, swivel, and top of compliant tool	Direct	362.47	N
WOB_{BOT}	Weigh of bottom of compliant tool, drill pipe, and bit	Direct	84.06	N
M_{TOP}	Mass of motor head, swivel and, top of compliant tool	Direct	36.95	kg
M_{BOT}	Mass of bottom of compliant tool, drill pipe, and bit	Direct	8.57	kg
I	Mass moment of inertia of all rotating components	Direct	0.0176	kgm^2
a	Drill bit radius	Direct	0.0156	m
n	Number of cutters of the bit	Direct	2	
l_n	Length of bit cutters wearflat surface	Direct	0.00488	m
k_{spring}	Spring constant of compliant tool	Tuned	See Table 5.2	N/m
R_{damp}	Damping coefficient of compliant tool	Tuned	2500	Ns/m
F_{BHP}	Force due to bottom hole pressure	Tuned	See Figure 5.8b	N
F_P	Pump-off force	Tuned	See Figure 5.8a	N
R_{RP}	Friction force between rack and pinion	Tuned	170	N
R_{seal}	Friction force between seal and drill pipe	Tuned	750	N
ζ	Orientation of the cutting reaction	Tuned	0.8269	
ε	Rock intrinsic specific energy	Tuned	116.729	MPa
μ	Coefficient of friction	Tuned	0.25	
γ	Orientation of the frictional contact surfaces associated with the cutters	Tuned	7.4473	
σ	Maximum contact pressure at the wearflat/rock interface	Tuned	11.682	MPa

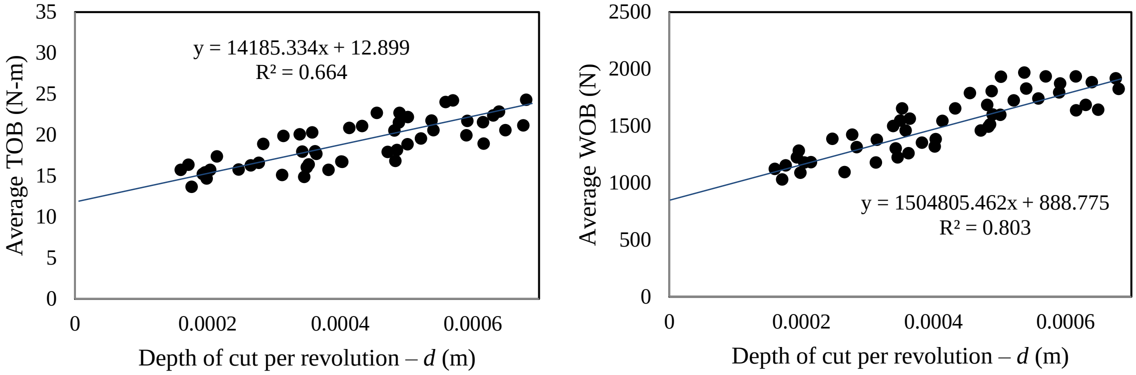

(a) (b)

Figure 5.5. Preliminary test for bit-rock parameter calculation. (a) Average TOB vs. *d* (b) Average WOB vs. *d*

5.2.1. Bit-rock Parameters

Preliminary drilling tests were carried out under controlled conditions in order to obtain the bit-rock interaction parameters. For every test, a different weight was applied in order to obtain various values of depth of cut (*d*). Average values of *WOB*, *TOB*, and *d* were measured from the data acquisition system. Numerical relations for the bit-rock interaction described in previous chapters (Equations 3.3 and 3.4) establish that if the surfaces are assumed to be in contact with the rock at all times, plots of the average value of *WOB* vs. *d* and TOB vs. *d* should yield straight lines. The slopes of these lines represent the change of cutting components with depth of cut and the y-intercepts represent the frictional components.

Preliminary test results are shown in Figures 5.5a and 5.5b. For both data sets, a linear regression was done using the least squares method and the parameters of the straight lines, namely slope and y-intercept, were obtained. By using the slopes (m_1, m_2) and y-intercept (b_1, b_2), the bit-rock interaction parameters were calculated from the following equations:

$$\sigma = \frac{b_1}{al} \tag{5.1}$$

$$\gamma\mu = \frac{2b_2}{a^2 l\sigma} \tag{5.2}$$

$$\varepsilon = \frac{2m_2}{a^2} \tag{5.3.}$$

$$\zeta = \frac{m_1}{\varepsilon a} \tag{5.4}$$

where

b_1, b_2	y-intercept of the WOB and TOB vs. d plot;
m_1, m_2	slope of the WOB and TOB vs. d plot.

Parameters γ and μ are never used separately so an individual calculation is unnecessary. However, if this is required, μ can be found from the conventional rock triaxial test as:

$$\mu = \tan\varphi \tag{5.5}$$

where

φ	internal friction angle of the rock.

Using the straight line parameters shown in Figure 5.5 as well as Equations 5.1 to 5.4, all the required parameters for the bit-rock interaction model were obtained. Resultant values are given in Table 5.1.

5.2.2. Drilling System Parameters

(i) Compliant Tool Constants

The compliant tool is comprised of two kinds of elements: a set of coned disc springs and a set of rubber rings (See figure 5.6). By varying the configuration of the coned disc springs, different spring constants can be achieved. The compliant tool has been individually tested in a test bench where various levels of compressive force and displacement were applied to measure the response. Detailed information about the test can be found in [56].

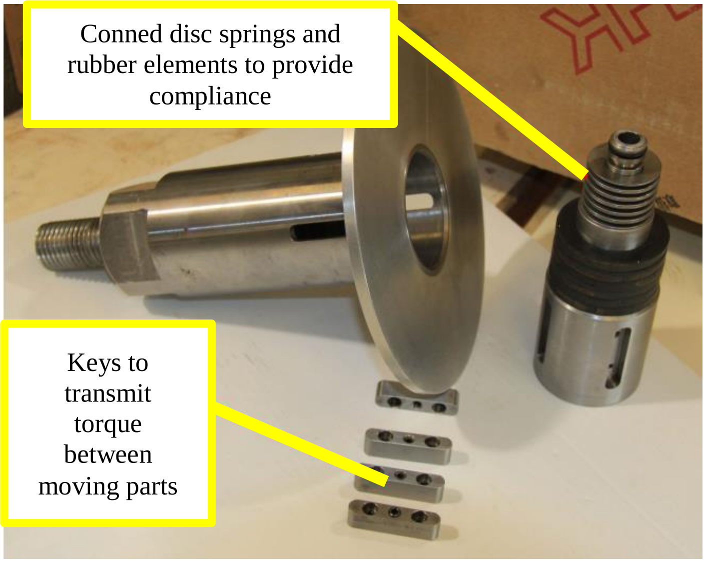

Figure 5.6. Compliant tool internal elements

Three different configurations were used in the experimental tests and simulations. Table 5.2 summarizes the compliant tool spring constants.

Table 5.2. Compliant tool parameters

Parameter	Configuration 1 (Rigid)	Configuration 2 (Single strong)	Configuration 3 (Double strong)
k_{spring} (N/m)	30 000 000	277 984.99	662 428.95
R_{damp} (Ns/m)	2500	2500	2500

(ii) Friction Effects

The frictional contact that takes place between the rack and pinion teeth when the motor is traveling down was measured by performing free fall tests of the motor and by measuring the displacement curve of the motor. Figure 5.7 shows a schematic illustration of the test system and its equivalent bond graph.

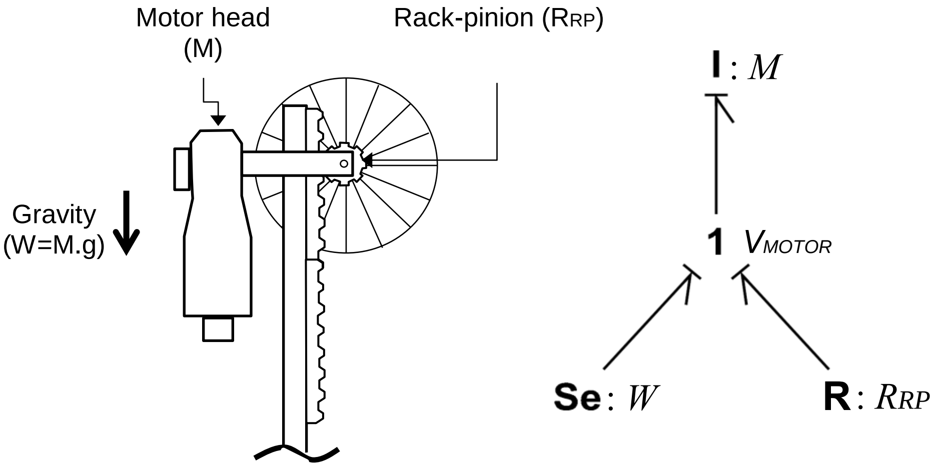

(a) (b)

Figure 5.7. Drop test for rack-pinion friction. (a) Schematic figure of test system. (b) Equivalent bond graph

Friction between the pinion and rack is considered to be dry friction. This is modeled as a resistance element. By tuning the value of R_{RP} to match the simulation results with the free fall tests, it was possible to find a value that represented the dissipation of energy due to this friction. Figure 5.8 shows a plot of position vs. time obtained from the LPT and the equivalent simulation result after tuning the value of $\mathrm{R_{RP}}$.

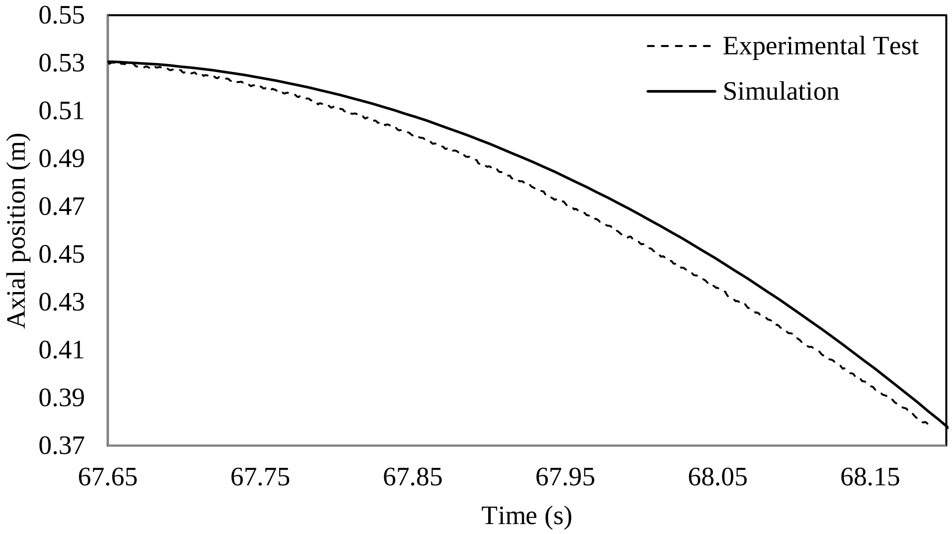

Figure 5.8. Axial position of motor head for drop test 1

Friction between the drilling cell seal and the drill pipe (R_{seal}) was calculated in a similar way. In this occasion, the drop test was performed with all the rig system elements and with the drillstring inside the drill cell to calculate the resistance force of the cell seal. Figure 5.9 shows the test results and the equivalent simulation result after tuning the parameter.

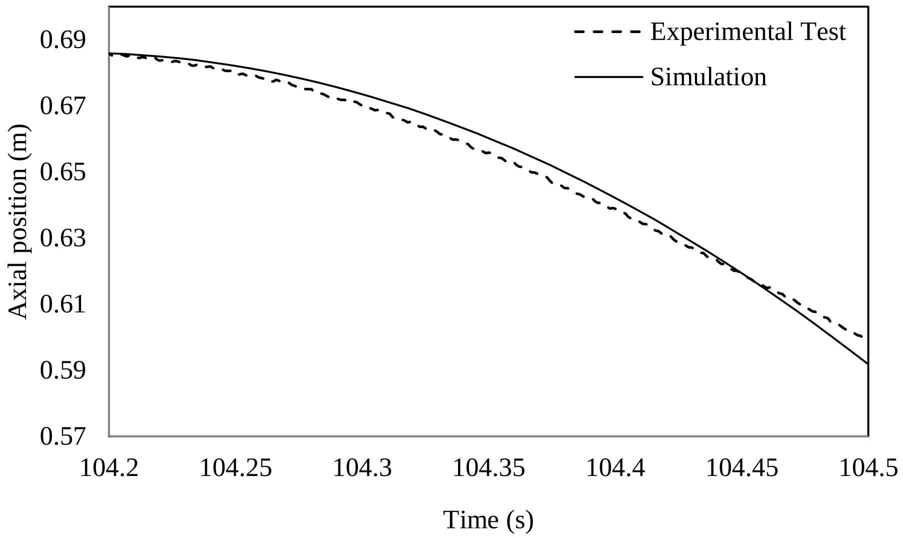

Figure 5.9. Axial position of bit for drop test 2

(iii) Hydraulic Forces

When the drilling system is in operation, a drilling fluid is pumped through the drill pipe to the bit nozzles. This high velocity water flow creates an upward force (F_P) that depends on the nozzles' diameter and the flowrate. Additionally, the pressure inside the drilling cell also acts on the bit bottom area as an upward force (F_{BHP}). These two forces need to be included in the simulation as they counteract the total applied weight.

For the pump-off force calculation, the bit is restricted to be fixed and close to the rock sample (<3mm). Load cell readings are taken as the flowrate is changed along the desired range. In these tests, the bottom-hole pressure was kept to zero. The equivalent pump-off force for different flowrate values is shown in Figure 5.10a. The bottom-hole pressure force was calculated in a similar fashion. In this case, a very low flowrate was used to avoid any pump-off force effects. Load cell readings were taken for different values of bottom-hole pressure. The results are shown in Figure 5.10b.

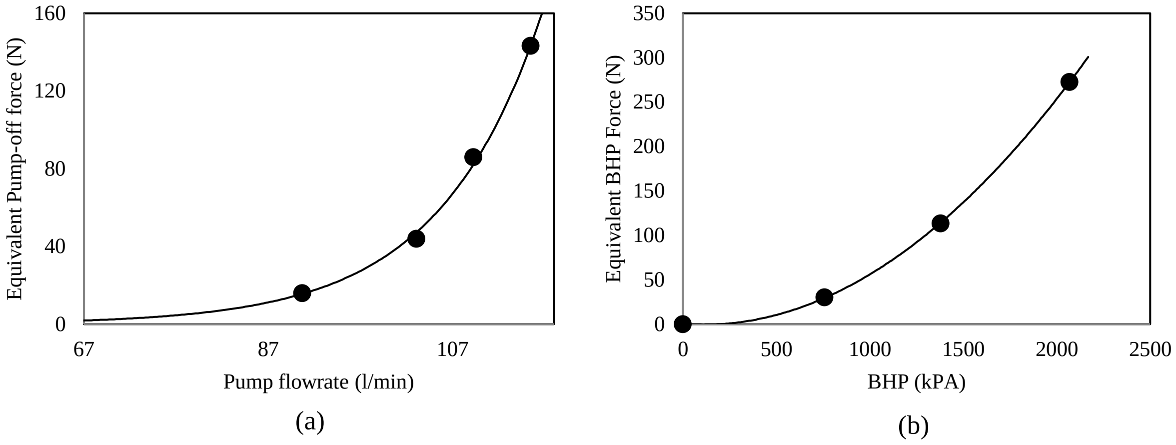

Figure 5.10. Hydraulic forces calculation. (a) Equivalent pump-off force. (b) Equivalent BHP force.

5.3. Experimental Tests

5.3.1. Sample Preparation

During the experimental tests, drilling was performed in synthetic rock materials. The samples were prepared by pouring concrete slurry in molded cylinders with 100 mm diameter. The concrete mixture includes aggregate, cement, water, and a high range water reducer also known as superplasticizer. The design material quantities of these materials are presented in table 5.3. A standardized procedure, further detailed in [57], was used for sample preparation in order to guarantee that all prepared samples had the same properties. The physical properties of the samples are presented in Table 5.4.

Table 5.3. Design quantities for synthetic rock material [57]

Material	**Design quantities**
Aggregate	30 kg
Cement	10 kg
Water	4.5 kg = 4500 ml
Superplasticizer (Daracem 19)	60 ml

Table 5.4. Properties of synthetic rock materials [57]

Property	**Value**
Unconfined Compressive Strength (UCS)	78 MPa
Density	2313 kg/m^3
Mohr Friction Angle	≈ 42°

5.3.2. Test Procedure

Drilling tests were conducted on the synthetic rock samples. The length of the drilled holes was selected to make sure there was complete contact between the bit cutters and the rock. This was also done in order to ensure that a constant *ROP* and angular speed was achieved. Three different configurations of the compliant tool were tested. Table 5.5 summarizes the tests parameters.

Table 5.5. Experimental test parameters for model validation

Nominal depth of each run (mm)	40
Nominal angular speed (rad/s)	31.41
Bottom hole Pressure (psi)	100
Flowrate (gpm)	23.95
Range of applied Weight (N)	1223.21 - 2295.37

Real angular speed, *ROP*, average depth of cut, and axial displacement of the bit was obtained from the recorded data. Results are presented in the following section.

5.4. Validation of Simulated Model against Experimental Tests

5.4.1. Performance Results

Simulations of the lab scale drilling system were carried out using the same input parameters as in experimental tests: applied weight, angular speed, bottom-hole pressure, and flowrate. The simulations results were analyzed to obtain average *ROP* values and steady state depth of cut for every test in order to be compared with experimental results.

Table 5.6 and 5.7 show the results for the drilling system experimental tests and simulations using the rigid configuration of the compliant tool. The first two simulations with this configuration were done with no C or R element in the axial dynamics. Ideally this would be true, but the real test setup is not completely rigid. There are bearings and seals that contribute to the overall axial compliance of the system. Due to the limitations of the test system, it was not possible to physically measure the stiffness coefficient of the overall system with the rigid configuration. However it is possible to observe that when including stiffness and damping in the rigid configuration (see Table 5.6), the difference between experimental and simulation results is decreased from 46.72% to 10.24% in ROP values and from 47.77% to 7.98% in depth of cut per revolution (*d*).

Table 5.6. Experimental and simulation results for tests with rigid configuration

Test Parameters				Experimental Results		Simulation Results		% Absolute Difference	
Axial Stiffness (kN/m)	Total Applied Weight (N)	BHP (psi)	Angular Speed Ω (rad/s)	Average ROP (mm/s)	*d* (mm)	Average ROP (mm/s)	*d* (mm)	ROP	*d*
None	1433.254	100	26.133	1.679	0.4037	0.564	0.130	66.41	67.80
None	1894.302	120	24.874	2.438	0.6159	1.779	0.445	27.04	27.75
							Average	46.72	47.77

Table 5.7. Experimental and simulation results for tests with rigid configuration after including stiffness

Test Parameters				Experimental Results		Simulation Results		% Absolute Difference	
Axial Stiffness (kN/m)	Total Applied Weight (N)	BHP (psi)	Angular Speed Ω (rad/s)	Average ROP (mm/s)	*d* (mm)	Average ROP (mm/s)	*d* (mm)	ROP	*d*
30 000	1433.254	100	26.133	1.679	0.4037	1.870	0.356	11.38	11.81
30 000	1505.702	120	25.805	1.996	0.4861	1.718	0.420	13.95	13.60
30 000	1587.670	135	25.150	2.459	0.6143	1.979	0.506	19.51	17.62
30 000	1721.428	120	25.338	2.383	0.5908	2.493	0.610	4.65	3.25
30 000	1894.302	120	24.874	2.438	0.6159	2.600	0.630	6.63	2.28
30 000	2127.370	135	24.602	3.124	0.7979	3.557	0.907	13.85	13.67
							Average	10.24	7.98

Figure 5.11 shows the results of *d* and *ROP* for different values of applied *WOB* for the rigid configuration after including compliance in the simulation. It is possible to see that the relation between *WOB* and *ROP* is positive but not totally linear. This is an expected result due to the nonlinearities introduced by the delay equations and the friction forces. Additionally, for higher values of applied *WOB* the simulation predicts better performance

than the experimental results. The numerical model assumes that all cuttings are successfully removed by the drilling fluid. Therefore, a lower performance in experimental results at higher WOB is possibly due to poor cleaning of cuttings.

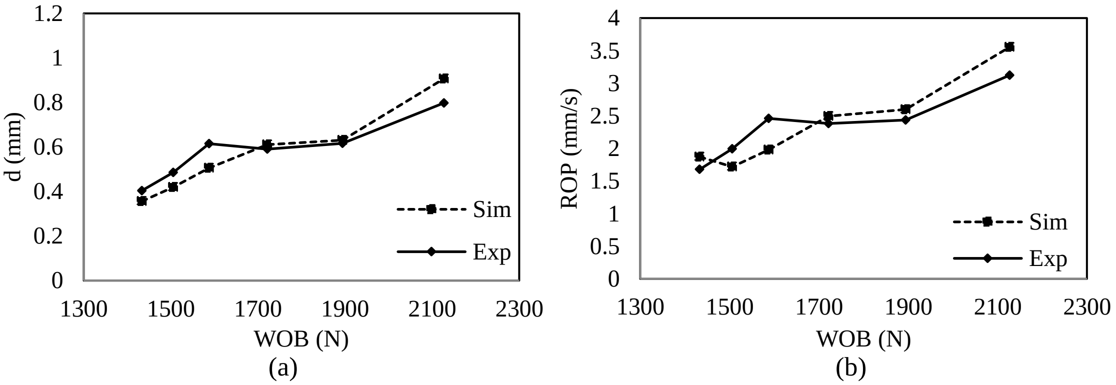

Figure 5.11. Rigid configuration performance results. (a) Depth of cut. (b) ROP.

Figures 5.12 and 5.13 show the results of *ROP* and *d* vs. applied *WOB* for the single strong and the double strong configuration. It is possible to see that both parameters are equivalent values for analyzing the drilling performance. However, this affirmation is only true when the angular speed is kept constant for all *WOB* ranges. If changes of angular speed are expected, only *d* should be considered as a performance parameter since it is independent of the angular velocity.

For the analyzed ranges of *WOB*, simulations are in good agreement with experimental results. Considering the limited capabilities of the test setup, these results are encouraging and show that a close prediction of the drilling response of a PDC bit is possible under the proposed model. In both cases, greater difference is observed for higher values of applied WOB. In the literature, it is well described how the increase of ROP with applied weight can be affected by poor cleaning at higher ranges. Therefore, this is considered as the main factor of the mentioned difference at higher ranges of WOB.

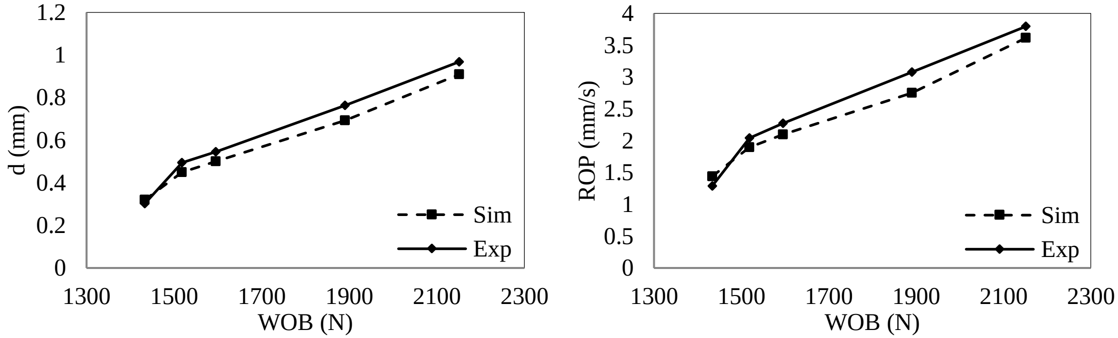

(a) (b)

Figure 5.12. Single strong configuration performance results. (a) Depth of cut. (b) ROP.

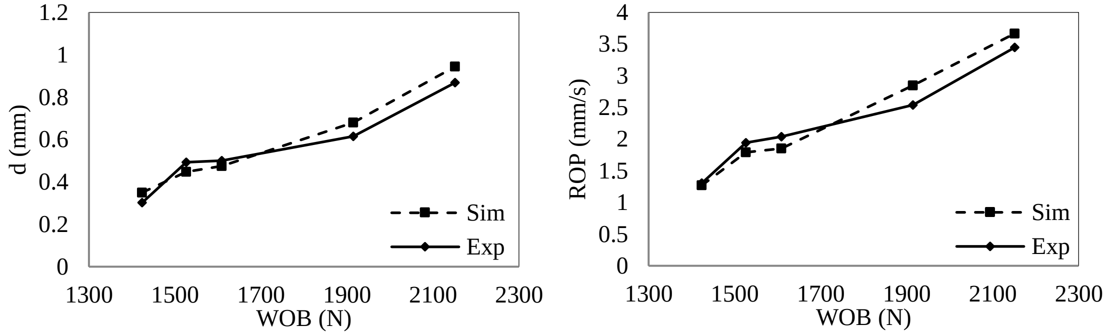

(a) (b)

Figure 5.13. Double strong configuration performance results. (a) Depth of cut. (b) ROP.

It is not in the scope of this research to analyze the difference in performance results between the different configurations of the compliant tool. However, simulations and experimental tests results allow for comparison of the different configurations. Simulation tools can also help to study why under same applied weights, a different compliance in the tool yields better performance results. Performance analysis of the compliant tool has been done by Rana *et al* [58]. This investigation reports that axial vibrations generated by the tool play an important role in the removal of cuttings and drilling performance. This explains why under simulated conditions of perfect cutting removal the compliant tool does not yield better results than the rigid configuration (see Figure 5.14) and in experimental tests the more compliant configuration outperforms the rigid configurations.

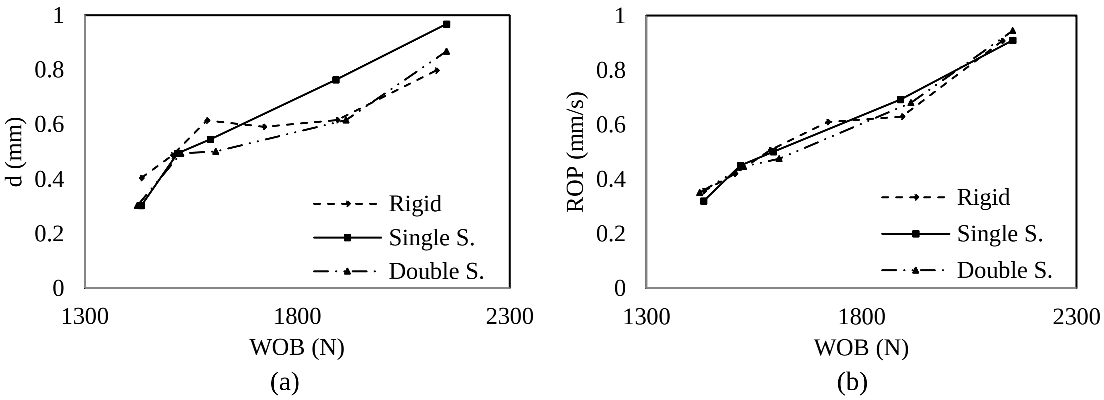

Figure 5.14. Comparative results between different configurations.
(a) Experimental results. (b) Simulation results

There is still much to investigate about how axial vibrations can enhance drilling performance. Certainly, the use of this model is a promising tool for evaluation of the different mechanisms if cutting removals and compliance characterization is considered.

5.4.2. Frequency Analysis

An important aspect to perform validation of the simulation results is the frequency content of the resultant vibration signals. Due to the limitations of the data acquisition system of the test setup, only axial vibrations were registered and analyzed.

By performing a Fast Fourier Transform (FFT), it is possible to convert the vibration signals, from its original time domain, to a representation in the frequency domain. This allows for identification of the different frequencies in a complex signal.

Figure 5.15 shows an example of the bit axial displacement obtained for one of the simulations. This plot contains the axial vibration signal but also the overall axial displacement of the bit. In order to perform a FFT analysis of this signal, it is necessary to eliminate the overall axial displacement in order to leave only the axial vibration content. This is done by applying the following equation:

$$U_{vib} = \left(t \times ROP_{avg}\right) - U \tag{5.6}$$

where

U_{vib}	Bit axial vibration;
t	time;
ROP_{avg}	Average ROP;
U	Bit axial displacement.

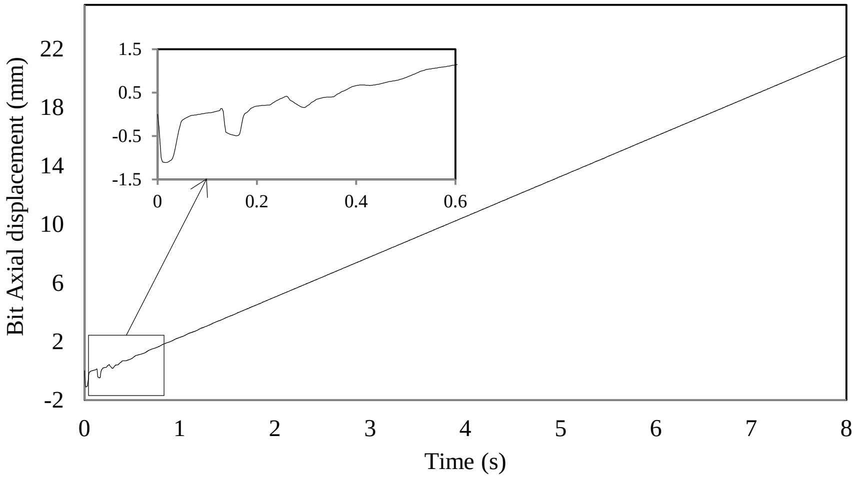

Figure 5.15. Example of bit axial displacement obtained from simulations.

By applying equation 5.6, the overall displacement of the bit is eliminated leaving only the axial oscillations of the bit whose frequency content can now be analyzed by performing a FFT (See Figure 5.16).

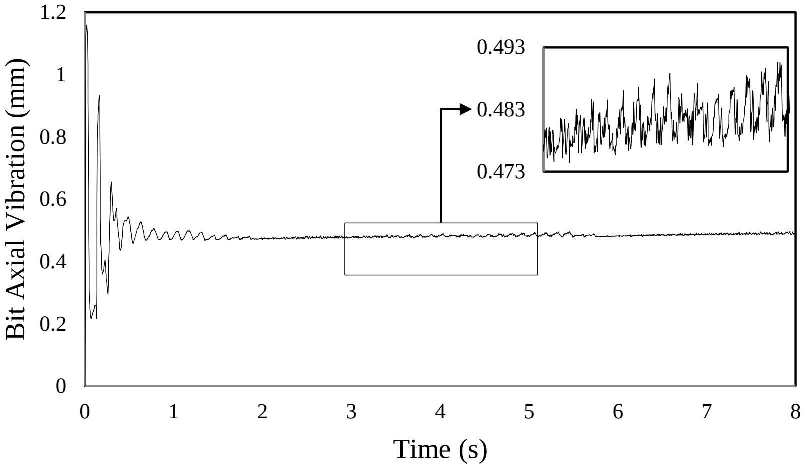

Figure 5.16. Bit axial vibration from simulations.

Figure 5.17 shows a FFT of the bit axial vibration for three simulations, one for each compliant tool configuration. In the compliant configurations (Figures 5.17a and 5.17b), the dominant frequency is found at 2 times the angular velocity which is related to the number of cutters of the bit. The other peaks are multiples of the main frequency. In the rigid configuration (see Figure 5.17c) the signal presents great amounts of noise, this is probably caused by the high frequency introduced by the stiff C-element. As expected, the amplitude of the vibrations is decreased as the tool configuration becomes more rigid.

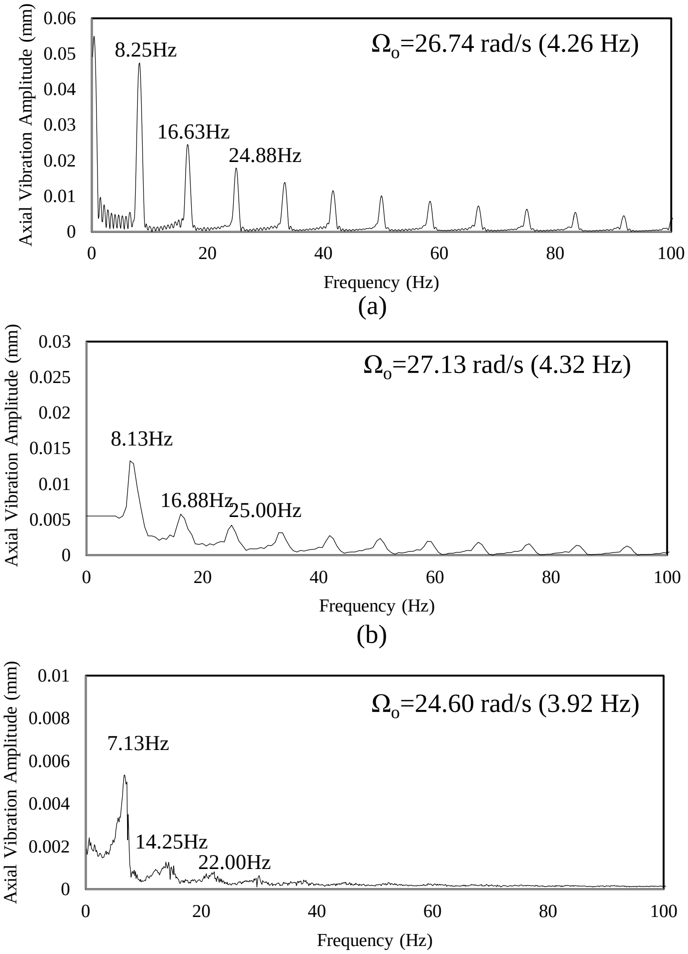

(a)

(b)

(c)

Figure 5.17. FFT of axial vibrations in simulations. (a) Single strong configuration. (b) Double strong configuration. (c) Rigid configuration.

The frequency results help to confirm the existence of coupling between torsional and axial modes of vibration occurring at the bit-rock interaction and related to the angular speed (input) and the amount of cutters (bit characteristic).

Figure 5.18 shows the FFT from the corresponding experimental tests of Figure 5.17. In all experimental results, the dominant frequency is found around the angular velocity and its multiples. This pattern is not consistent with simulation results. Additionally, the amplitude of the main peak is ten times greater than those observed in simulations. A further study on the matter led to believe that these peaks were not due to bit-rock interaction but due to mass unbalance in the rotor.

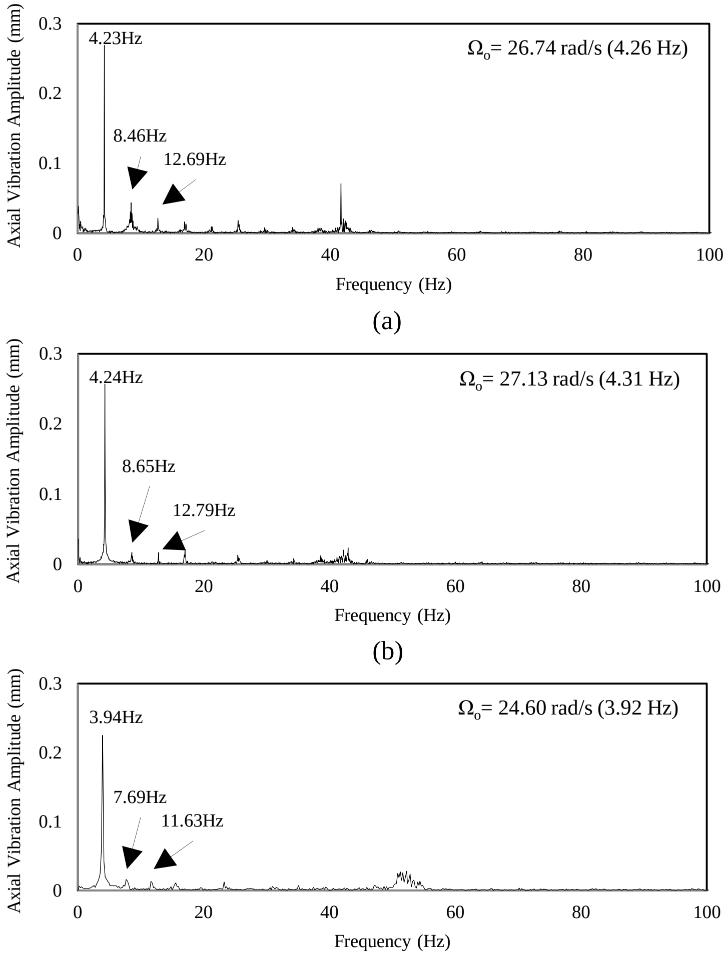

(a)

(b)

(c)

Figure 5.18. FFT of axial vibrations in experimental tests. (a) Single strong configuration. (b) Double strong configuration. (c) Rigid configuration.

To confirm the unbalanced rotor hypothesis, the drilling setup was run with the bit off bottom. FFT analysis of the axial vibrations registered in this test is shown in Figure 5.19. Without any bit-rock interaction present, the peaks at 1, 2, and 3 times the angular speed still appeared on the graph with similar amplitude than those observed while drilling. This confirms that the high peaks observed in Figure 5.18 are not due to bit-rock interaction but they are the primary symptom of mass unbalance as described in [59].

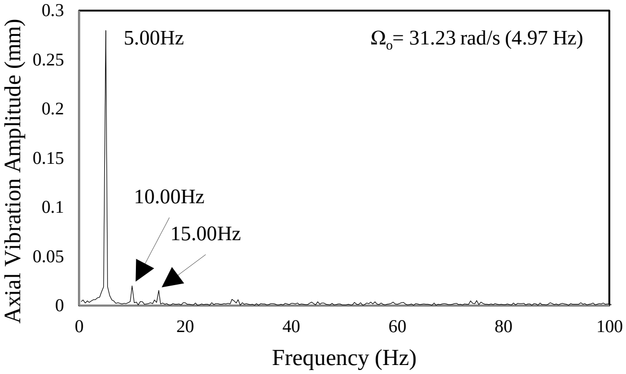

Figure 5.19. FFT of axial vibrations in experimental test with off-bottom bit

Finally, the peaks due to rotor unbalance (1x, 2x, and 3x angular velocity) and a high frequency peak possibly related to roller elements on the motor bearings (10x angular speed) were subtracted from Figure 5.18b. The amplitude and dominant frequencies from the experimental test, become more consistent with those observed in the simulations (see Figure 5.20).

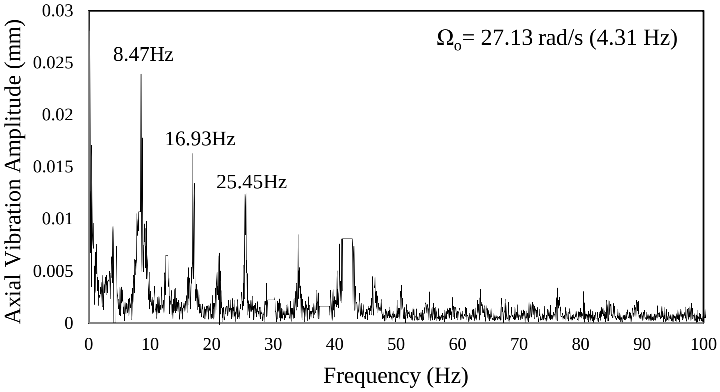

Figure 5.20. FFT of axial vibrations in experimental test for double strong configuration after removing unbalanced rotor and bearing wear effects.

When performing an FFT analysis from a discrete signal such as the ones obtained from simulations and experiments, the spectrum computed from the sampled signal has a frequency resolution. This refers to the ability of the plot to distinguish between two peaks that lie in the vicinity of each other. The frequency resolution depends solely on the acquisition time. One important aspect of the FFT analysis is to make sure that two close peaks will not look as one due to a low plot resolution. For the studied signals, the minimum frequency related to the angular velocity was found at 3.92 Hz and the expected signals are all multiples of it. For the signals shown in Figures 5.17 and 5.18, the maximum resolution is 0.2 Hz. This confirms that no low-resolution issues were present.

CHAPTER 6

SUMMARY AND CONCLUSIONS

6.1. Summary of Present Work

The increased complexity of processes in hydrocarbon production has lead the oil and gas industry to focus on drilling optimization, which represents a major portion of their operations. In this context, analysis of vibrations in drillstrings and downhole equipment play a major role due to the consequences of severe vibration on equipment failure and drilling performance. The goal of vibration analysis is to understand the circumstances under which severe vibrations occur in order to develop drilling strategies and tools to prevent failure. By developing numerical models that simulate dynamic drilling conditions, it is possible to project and to understand these circumstances.

When modeling dynamic conditions in a drillstring, the reaction forces that occur at the bit-rock interface are a critical input. This is because, according to experimental evidence, torsional vibrations are caused by the instabilities introduced by the bit-rock interaction. However, despite the critical nature of this aspect, the bit-rock interaction modeling is often done with overly simple treatment or with models for which parameter identification is difficult. For this reason, this research presented a drillstring numerical model in which the bit-rock interaction parameters are not assumed, but can be obtained from drilling tests.

In this numerical model, no lateral motions are considered, only the axial and torsional dynamics are modeled. For this, the drillstring is modeled as a spring, both in axial and torsional modes. The drill collar, being heavier than the drill pipes, is modeled as a rigid mass that provides WOB and Inertia effects. The torsional and axial dynamics of the system are modeled separately using the bond graph technique. Coupling between axial and torsional dynamics is given by the bit-rock interaction model.

The bit-rock interaction model is based on a previous research by Richard *et al* [28]. This is based on the premise that reaction forces at the bit are composed of a cutting component occurring at the bit cutter and a friction component occurring at the bit wearflat surface. In this model, the friction torque is assumed to be independent of the angular speed. Based on these premises, the cases for contact loss at the different bit surfaces were analyzed and included as numerical functions to account for bit-bounce and stick-slip during drilling. These functions are considered in order to avoid discontinuities that could introduce instabilities during the simulation.

A new implementation of the model is proposed. This involves co-simulation with two different software programs. Co-simulation allows the drillstring system equations to be solved with ODE numerical models and the bit-rock interaction system equations to be solved separately with Matlab. By using this approach the drillstring configuration and boundary conditions can be modified easily. This research also proposes a methodology for obtaining bit-rock parameters from drilling tests and physical measurements. This allows for simulation of any real drilling system without making great assumptions of the simulation parameters. Finally, the model was validated against experimental tests to confirm their applicability for prediction of drilling response.

6.2. Concluding Remarks

- The bond graph model of a drillstring provides a practical way to evaluate drillstring dynamics. Modification of boundary conditions, external forces or drillstring configuration can be done easily without altering the model equations.
- Verification of the model confirmed that the design of the model was captured by the computer implementation with sufficient accuracy and that it yields predictable results for known inputs.
- Similarly to previous numerical models of drillstrings, as well as field tests, the magnitude of the imposed angular velocity and *WOB* showed a strong effect in the development of torsional vibrations and stick-slip.

- The model shows that during stick slip, energy from the torsional motion is transferred to the axial motion and other types of vibration, such as bit-bounce, are developed. This observation shows that the model is capable of capturing coupling between axial and torsional motion through the bit-rock interaction.
- Parameters related to the bit geometry and bit wear are also shown to influence in the development and sustainability of vibrations. Wear in the bit dissipates energy in the form of friction which dampens torsional vibrations but also reduces the drilling performance.
- The initial assumption that friction forces are independent of the angular speed is confirmed. In fact, the increase of *TOB* with decreasing angular speed showed to be closely related to the increase of axial vibrations. This confirms that the velocity weakening effect is a consequence rather than the cause for stick-slip oscillations.
- Availability of a method to obtain bit-rock parameters from real drilling conditions allowed for validation of the model against experimental tests. For the analyzed ranges of applied WOB, the simulations were in good agreement with the experimental results. Considering the limited capabilities of the test setup, these results are encouraging and show that a close prediction of the drilling response of a PDC bit is possible under the considered model.

- Greater difference between experiments and simulations is observed for higher values of applied WOB. At higher ranges of WOB, poor cleaning of cuttings is an important factor that was not considered in the model.

6.3. Limitations of the Work

Among the limitations of the numerical model is the effect of a higher *WOB* in removal of cuttings. This was not considered in the model and seems to be significant for drilling performance results. On the other hand, the limited capacity of the laboratory setup did not allow for testing of higher *WOB* ranges in order to confirm the previous affirmation.

The measurement of torsional oscillations was not possible with the experimental setup. This limited the frequency analysis to only axial vibrations. It is known that comparison of the frequency content between torsional and axial oscillation could deepen the investigation regarding coupling due to bit-rock interaction in the system.

Validation of the model was limited to ROP, depth of cut, and axial frequency content. Conditions under which stick-slip vibrations are developed were not validated mainly due to the laboratory setup limitations. The drillstring in the lab scale setup is not long enough to be torsionally compliant. This makes the angular velocity of the bit to be controlled by the rotary head at all times. Therefore, stick-slip could not be observed in experimental tests.

6.4. Future Work

Further study on the effect of poor cuttings removal at higher WOB rates is required. Additionally, inclusion of this in the numerical model would produce a more accurate model for all WOB ranges.

Validation of the model using drilling bits with different geometrical characteristics such as number of cutters, radius of the bit, and back rake angle would help to further study the implications of bit geometry on the bit-rock interaction parameters.

Development of a drillstring with scaled characteristics of torsional compliance would allow drilling under field-like circumstances. This would enable the validation of stick-slip conditions.

A new lab scale drilling rig has been developed in the research facilities and is under testing. Drillstring vibration analysis on this setup would allow further validation of the numerical model and experimental investigation of the conditions for stick-slip development. On this basis, a set of sensors for *WOB* and *TOB* measurements are required. The new scaled drilling system currently has a torque sensor built in the drive unit and an incremental optical encoder built in the motor. However, if a flexible drillstring were to be included, load and torque measurements would need to be taken right before the bit. This could be done by an attached tool that, with a set of strain gages, would measure the force and torque on the bit.

Modification of the drillstring model to a multibody lumped segment model is among the future work in this area. Also, extension of the model to an integrated model that includes other equipment related to drilling operation such as drilling riser and blow-out preventer. This would allow for calculation of the forces that this equipment is subjected to while drilling. Some work has been done in this field and is shown in Appendix C.

Experimental investigation on the topic of cuttings removal when using different configurations of the compliant tool is recommended. This would allow to confirm if the suggestions made in this investigation are true for experimental tests. Previous work has been performed by the author on this matter and is shown in Appendix D. Based on the procedures and analysis proposed in Appendix D, further analysis on the cuttings obtained during the experimental drilling tests could help to better understand the mechanism by which the more compliant configuration of the tool yields better performance results.

References

[1] S. Lambert, J. Rogers, J. Williamson, C. Boyer and J. Frantz, "Benchmarking deep drilling technologies," presented at SPE Annu. Tech. Conf. and Exhibition, Dallas, TX, USA, Oct. 9-12, 2005.

[2] J. M. Kamel and A. S. Yigit, "Modeling and analysis of stick-slip and bit bounce in oil well drillstrings equipped with drag bits," *J. Sound Vibrat*., vol. 333, no. 25, pp. 6885-6899, Dec. 2014.

[3] S. K. Vogel and A. P. Creegan, "Case study for real time Stick/Slip mitigation to improve drilling performance," presented at SPE/IADC Middle East Drilling Technology Conference and Exhibition, Abu Dhabi, UAE, Jan, 26-28, 2016.

[4] T. Richard and E. Detournay, "Stick–slip motion in a friction oscillator with normal and tangential mode coupling," *Comptes Rendus De l'Académie Des Sciences-Series IIB-Mechanics*, vol. 328, no. 9, pp. 671-678, Sep. 2000.

[5] T. Richard, C. Germay and E. Detournay, "Self-excited stick–slip oscillations of drill bits," *Comptes Rendus MECANIQUE,* vol. 332, no. 8, pp. 619-626, Aug. 2004.

[6] R. F. Mitchell and S. Miska, "Introduction to Rotary Drilling," in *Fundamentals of Drilling Engineering*, SPE Textbook Series No. 12 Richardson, TX, USA: Society of Petroleum Engineers, 2011, ch. 1.

[7] A. T. Bourgoyne, K. K. Millheim, M. E. Chenevert and F. S. Young, "Rotary Drilling Bits," in *Applied Drilling Engineering*, SPE Textbook Series No. 2 Richardson, TX, USA: Society of Petroleum Engineers, 1986, ch. 5.

[8] W. Sölken, "Oil and Gas Well Drilling," in *Fossils into Fuels - Oil & Gas extraction,* 2008 [online] Available: http://www.wermac.org/others/oil_and_gas_well_drilling.html.

[9] J. J. Azar and G. R. Samuel, "Drill String Design," in *Drilling Engineering*, Tulsa, OK, USA: PennWell Corp., 2007, ch. 9.

[10] National Oilwell Varco, “RockForce™ Bits,” in *Products*, 2014 [online] Available: http://www.nov.com/Segments/Wellbore_Technologies/Downhole/Drill_Bits/Roller_Cone/RockForce_Bits/RockForce.aspx.

[11] J. Liou, “The Hughes Christensen Talon PDC”, 2016 [online]. Available: http://www.drillingcontractor.org/new-bits-look-beyond-design-at-overall-wellbore-16693.

[12] P. Paslay, “Stress analysis of drillstrings,” presented at University of Tulsa Centennial Petroleum Engineering Symp., Tulsa, OK, USA, Aug. 29-31, 1994.

[13] J. Bailey and I. Finnie, “An analytical study of drill-string vibration,” *J. Eng. Ind.,* vol. 82, no. 2, pp. 122-127, May 1960.

[14] D. Dareing and B. J. Livesay, “Longitudinal and angular drill-string vibrations with damping,” *J. Eng. Ind.,* vol. 90, no. 4, pp. 671-679, Nov. 1968.

[15] J. Jansen and L. Van den Steen, “Active damping of self-excited torsional vibrations in oil well drillstrings,” *J. Sound Vibrat.,* vol. 179, no. 4, pp. 647-668, Jan. 1995.

[16] A. Kyllingstad and G. W. Halsey, “A study of Slip/Stick motion of the bit,” presented at SPE Annu. Technical Conf. and Exhibition, Dallas, TX, USA, Sep. 27-30, 1987.

[17] G. Halsey, A. Kyllingstad, T. Aarrestad and D. Lysne, “Drillstring torsional vibrations: Comparison between theory and experiment on a full-scale research drilling rig,” presented at SPE Annu. Technical Conf. and Exhibition, New Orleans, LA, USA, Oct, 5-8, 1986.

[18] A. Ghasemloonia, D. G. Rideout and S. D. Butt, “A review of drillstring vibration modeling and suppression methods,” *J. Pet. Sci. Eng.,* vol. 131, pp. 150-164, Jul. 2015.

[19] T. V. Aarrestad and A. Kyllingstad, “An experimental and theoretical study of a coupling mechanism between longitudinal and torsional drillstring vibrations at the bit,” *SPE Drilling Eng.,* vol. 3, no. 1, pp. 12-18, Mar. 1988.

[20] A. Yigit and A. Christoforou, "Coupled axial and transverse vibrations of oilwell drillstrings," *J. Sound Vibrat.,* vol. 195, no. 4, pp. 617-627, Aug. 1996.

[21] A. Yigit and A. Christoforou, "Coupled torsional and bending vibrations of drillstrings subject to impact with friction," *J. Sound Vibrat.,* vol. 215, no. 1, pp. 167-181, Aug. 1998.

[22] A. Yigit and A. Christoforou, "Coupled torsional and bending vibrations of actively controlled drillstrings" *J. Sound Vibrat.,* vol. 234, no. 1, pp. 67-83, Jun. 2000.

[23] R. Tucker and C. Wang, "The excitation and control of torsional slip-stick in the presence of axial-vibrations," Lancaster University, Bailrigg, UK, 1997.

[24] A. S. Yigit and A. P. Christoforou, "Stick-slip and bit-bounce interaction in oil-well drillstrings," *J. Energy Resour. Technol.,* vol. 128, no. 4, pp. 268-274, Feb. 2006.

[25] W. Tucker and C. Wang, "An integrated model for drill-string dynamics," *J. Sound Vibrat.,* vol. 224, no. 1, pp. 123-165, Jul. 1999.

[26] A. P. Christoforou and A. S. Yigit, "Active control of stick-slip vibrations: The role of fully coupled dynamics," presented at SPE Middle East Oil Show, Manama, Bahrain, Mar. 17-20, 2001.

[27] A. Christoforou and A. Yigit, "Fully coupled vibrations of actively controlled drillstrings," *J. Sound Vibrat*., vol. 267, no. 5, pp. 1029-1045, Nov. 2003.

[28] T. Richard, C. Germay and E. Detournay, "A simplified model to explore the root cause of stick–slip vibrations in drilling systems with drag bits," *J. Sound Vibrat.,* vol. 305, no. 3, pp. 432-456, Aug. 2007.

[29] F. Clayer, J. Vandiver and H. Lee, "The effect of surface and downhole boundary conditions on the vibration of drillstrings," presented at SPE Annu. Technical Conf. and Exhibition, New Orleans, LA, USA, Sep. 23-26, 1990.

[30] J. F. Brett, "The genesis of bit-induced torsional drillstring vibrations" *SPE Drilling Eng.,* vol. 7, no. 3, pp. 168-174, Sep. 1992.

[31] E. Detournay and P. Defourny, “A phenomenological model for the drilling action of drag bits,” *Int. J. Rock Mech. Min. Sci. & Geomech. Abstracts*, vol. 29, no. 2, pp. 13-23, Jan 1992.

[32] T. Richard, E. Detournay, M. Fear, B. Miller, R. Clayton and O. Matthews, “Influence of bit-rock interaction on stick-slip vibrations of PDC bits,” presented at SPE Annu. Technical Conf. and Exhibition, San Antonio, TX, USA, Sep. 29- Oct. 2, 2002.

[33] E. Detournay, T. Richard and M. Shepherd, “Drilling response of drag bits: Theory and experiment,” *Int. J. Rock Mech. Min. Sci.*, vol. 45, no. 8, pp. 1347-1360, Dec. 2008.

[34] J. I. Adachi, E. Detournay and A. Drescher, “Determination of rock strength parameters from cutting tests,” in *2nd North American Rock Mechanics Symp.*, Rotterdam, 1996, pp. 1517-1523.

[35] G. Schei, E. Fjær, E. Detournay, C. Kenter, G. Fuh and F. Zausa, “The scratch test: An attractive technique for determining strength and elastic properties of sedimentary rocks,” presented at SPE Annu. Technical Conf. and Exhibition, Dallas, TX, USA, Oct. 1-4, 2000.

[36] D. Pavone and J. Desplans, “Application of high sampling rate downhole measurements for analysis and cure of stick-slip in drilling,” presented at SPE Annu. Technical Conf. and Exhibition, New Orleans, LA, USA, Sep. 25-28, 1994.

[37] N. Challamel, H. Sellami, E. Chenevez and L. Gossuin, “A stick-slip analysis based on rock/bit interaction: Theoretical and experimental contribution,” presented at IADC/SPE Drilling Conf., New Orleans, LA, USA, Feb. 23-25, 2000.

[38] D. C. Karnopp, D. L. Margolis and R. C. Rosenberg, “Basic Bond Graph Elements,” in *System Dynamics: Modeling, Simulation, and Control of Mechatronic Systems*, 5th ed., Hoboken, NJ, USA: John Wiley & Sons, Inc., 2012, ch. 3.

[39] S. Skjong, “Modeling, simulation and control of hydraulic winch system,” M.S. thesis, Dept. Marine Technology, NTNU, Trondheim, Norway, 2014.

[40] J. Montbrun-Di Filippo, M. Delgado, C. Brie and H. M. Paynter, “A survey of bond graphs: Theory, applications and programs,” *J. Franklin Inst.*, vol. 328, no. 5, pp. 565-606, 1991.

[41] P. Breedveld, "Bond Graphs," in Encyclopedia of Life Support System, Enschede, Netherlands, 2003. [online]. Available: http://doc.utwente.nl/99988/1/Breedveld_03_BGConcepts.pdf

[42] X. Zhang, “Modeling, Control, Fault Detection and Isolation of Chemical Processes using a Bond Graph Framework,” PhD. Dissertation, Graduate Faculty, Texas Tech University, Lubbock, TX, 2009.

[43] M. Fear, F. Abbassian, S. Parfitt and A. McClean, “The destruction of PDC bits by severe slip-stick vibration,” presented at SPE/IADC Drilling Conference. Amsterdam, Netherlands, Mar. 4-6, 1997.

[44] L. C. D. Tianhuai, “Effect of damping boundary conditions on acoustic transmission of drill strings,” *J Vibrat. Shock*, vol. 25, no. 6, pp. 17-20, 2006.

[45] T. Ritto, R. Sampaio and C. Soize, “Drill-string dynamics coupled with the drilling fluid dynamics,” in *XIII International Symposium on Dynamic Problems of Mechanics*, Brazil, 2009, pp. 1-10.

[46] D. Karnopp and D. Margolis, “Analysis and simulation of planar mechanism systems using bond graphs,” *J. Mech. Design*, vol. 101, no. 2, pp. 187-191, Apr. 1979.

[47] L. F. Shampine, S. Thompson and J. Kierzenka, “Solving delay differential equations with dde23”, 2000. [Online]. Available: http://www.Runet.Edu/~thompson/webddes/tutorial.pdf

[48] Controllab Products, Enschede, Netherlands. *20-SIM.* (2016) [Online]. Available: http://www.20sim.com/download/20sim.html.

[49] The MathWorks, Inc., Natick, MA, USA. *MATLAB 2014b*. (2014) [Online]. Available: https://www.mathworks.com/products/matlab/whatsnew.html?s_tid=tb_16b

[50] S. Robinson, “Simulation model verification and validation: Increasing the users' confidence,” in *29th Conf. on Winter Simulation*, Washington, DC, 1997, pp. 53-59.

[51] P. K. Davis, “Generalizing Concepts and Methods of Verification, Validation, and Accreditation (VV&A) for Military Simulations,” National Defense Research Inst., Santa Monica, CA, USA, Rep. R-4249-ACQ, 1992.

[52] J. S. Carson, "Model verification and validation," in *Simulation Conference, 2002. Proceedings of the Winter*, San Diego, CA, USA, 2002, pp. 52-58.

[53] B. H. Thacker, S. W. Doebling, F. M. Hemez, M. C. Anderson, J. E. Pepin and E. A. Rodriguez, “Concepts of Model Verification and Validation,” Los Alamos National Laboratory, Springfield, VA, USA, Rep. LA-14167-MS, 2004.

[54] Q. Gao, “Development of laboratory and field drilling tools to measure bit operating conditions and drill string motions,” M.Eng. thesis, Faculty of Engineering and Applied Sciences., MUN, St. John’s, NL, 2015.

[55] H. Khorshidian, “Phenomena affecting penetration mechanisms of polycrystalline diamond compact bits,” M.Eng. thesis, Faculty of Engineering and Applied Sciences, MUN, St. John’s, NL, 2012.

[56] J. Zhong, “Investigation of Bit-Rock Interaction for Rotary Drilling and Influence on Penetration Rate,” M.Eng. thesis, Faculty of Engineering and Applied Sciences, MUN, St. John’s, NL, 2016.

[57] Z. Zhang, “Development and Characterization of Synthetic Rock-Like Materials for Drilling and Geomechanics Experiments,” M.Eng. thesis, Faculty of Engineering and Applied Sciences, MUN, St. John’s, NL, 2016.

[58] P. Rana, A. Abugharara, J. Molgaard and S. Butt, “Experimental evaluation of passive-vibration assisted rotary drilling (p-VARD) tool to enhance drilling performance,” Presented at 49th US Rock Mechanics/Geomechanics Symp., San Francisco, CA, USA, Jun. 28- Jul. 1, 2015.

[59] M. L. Adams, “Rotor Unbalance and Critical Speed Case Studies,” in *Rotating Machinery Vibration: From Analysis to Troubleshooting*, New York, NY, USA: Marcel Dekker Inc., 2009, ch. 10.

APPENDIX A

20-SIM PROGRAMMING CODES

A.1. 20-Sim Code for Variant 1

Note that Matlab equations are embedded in the 20 sim code with the commands: *toMatlab*, *doMatlab*, and *fromMatlab*.

//Bit_rock_parameters//

```
parameters
        real Bit_radius = 0.10795;
        real Zeta = 1.1;
        real Epsilon = 70000000;
        real Mu = 0.75;
        real Gamma = 1.2;
        real Blade_number = 3;
        real Sigma = 9000000;
        real Flat_lenght = 0.0018;

variables
        real global a;
        real global zeta;
        real global epsilon;
        real global mu;
        real global gamma;
        real global n;
        real global sigma;
        real global l;
```

//Drillstring_parameters//

```
parameters
        real Rotary_Interia = 103.8;
        real Mass = 40000;
        real Torsional_compliance = 470;

variables
        real global J;
        real global M;
```

```
        real global C;

                        //Top_Imposed_Parameters//

parameters
        real top_omega = 19;
        real top_WOB = 60000;
        real initial_angle = 0;

variables
        real global OMEGAo;
        real global WOBo;
        real global phio;

                        //Continuous-time equations//

initial equations:
//define initial values of variables from bit-rock parameters//
a = Bit_rock_parameters\Bit_radius;
zeta = Bit_rock_parameters\Zeta;
epsilon = Bit_rock_parameters\Epsilon;
mu = Bit_rock_parameters\Mu;
gamma = Bit_rock_parameters\Gamma;
n = Bit_rock_parameters\Blade_number;
sigma = Bit_rock_parameters\Sigma;
l = Bit_rock_parameters\Flat_lenght * n;

//take bit-rock variables to Matlab for future bit-rock model calculations//
toMatlab (a, 'a');
toMatlab (zeta, 'zeta');
toMatlab (epsilon, 'epsilon');
toMatlab (mu, 'mu');
toMatlab (gamma, 'gamma');
toMatlab (n, 'n');
toMatlab (sigma, 'sigma');
toMatlab (l, 'l');

//define initial values of variables from drillstring parameters//
J = Drillstring_parameters\Rotary_Interia;
M = Drillstring_parameters\Mass;
C = Drillstring_parameters\Torsional_compliance;
```

```
//define initial values of variables from top imposed parameters//
OMEGAo = Top_Imposed_Parameters\top_omega;
WOBo = Top_Imposed_Parameters\top_WOB;
phio = Top_Imposed_Parameters\initial_angle;

//create an empty matrix for OMEGA, PHI, V, U, time, WOB, TOB, tn, and D historic
values in Matlab//
doMatlab ('OMEGA=[];');
doMatlab ('PHI=[];');
doMatlab ('V=[];');
doMatlab ('U=[];');
doMatlab ('time=[];');
doMatlab ('WOB=[];');
doMatlab ('TOB=[];');
doMatlab ('tn=[];');
doMatlab ('D= [];');

//calculate steady state delay time and depth of cut and take values to matlab //
tno = (2 * pi) / (OMEGAo * n);
dno = (WOBo - ((a * l) * sigma)) / ((a * epsilon) * zeta);
toMatlab (dno, 'dno');
toMatlab (tno, 'tno');

//Set initial values in Matlab for bit-rock cases functions//
doMatlab ('Hd=1;');
doMatlab ('Hw=1;');
doMatlab ('Hv=1;');
doMatlab ('Hw2=1;');
```

dynamic equations:

```
//take values of omega, phi, v, u and time to Matlab and fill in historical values matrix//
toMatlab(omega,'omega');
doMatlab ('OMEGA=[OMEGA omega];');
toMatlab (phi, 'phi');
doMatlab ('PHI=[PHI phi];');
toMatlab(v,'v');
doMatlab ('V=[V v];');
toMatlab (u, 'u');
doMatlab ('U=[U u];');
toMatlab (time, 't');
doMatlab ('time=[time t];');

//calculate depth of cut from historical values//
```

```
doMatlab ('if phi<(2*pi/n);
                d=dno;tn=[tn tno];
        else;
                phit_tn=phi-(2*pi/n);                   //find delay angle//
                t_tn=interp1(PHI,time,phit_tn);         //find delay time//
                ut_tn=interp1q(time, U,t_tn);           //find delayed axial position//
                d=n*(u-ut_tn);                          //compute depth of cut//
                tn=[tn (t-t_tn)];                       //fill in delay time matrix//
        end;
                D=[D d];');                             //fill in depth of cut matrix//

//calculate current value for bit-rock cases functions//
doMatlab ('Hd=1/(1+exp((-200000*d)-1.5));
                Hw=1/(1+exp((-200000*omega)-1.5));
                Hv=1/(1+exp((-200000*v)-1.5));
                Hw2=tanh((70000*omega)+2);');

//take all required values for WOB and TOB from matlab to 20-sim//
fromMatlab (d, 'd');
fromMatlab (Hd, 'Hd');
fromMatlab (Hw, 'Hw');
fromMatlab (Hv, 'Hv');
fromMatlab (Hw2, 'Hw2');
```

bond graph equations:

```
OMEGA\flow = J\state / J;
k_torsional\p.e = k_torsional\state * C;
V\flow = M\state / M;
WOBc = ((((a * zeta) * epsilon) * d) * Hd) * Hw;
WOBf = (((a * l) * sigma) * Hv) * Hd;
TOBc = (((((a ^ 2) * epsilon) * d) * Hd) * Hw) / 2;
TOBf = ((((((((a ^ 2) * gamma) * mu) * l) * sigma) * Hv) * Hd) * Hw2) / 2;
WOB = WOBc + WOBf;
TOB = TOBc + TOBf;
Se1\effort = [-TOB; -WOB];
 [PowerDemux\output1.e; PowerDemux\output2.e] = Se1\effort;
k_torsional\p.f = OMEGAo - OMEGA\flow;
PowerDemux\input.f = [OMEGA\flow; V\flow];
M\p.e = PowerDemux\output2.e + WOBo;
J\p.e = PowerDemux\output1.e + k_torsional\p.e;
```

system equations:

```
J\state = int (J\p.e, J\state_initial);
```

k_torsional\state = int (k_torsional\p.f, k_torsional\state_initial);
M\state = int (M\p.e, M\state_initial);
phi = int (OMEGA\flow, phio);
u = int (V\flow, u_initial);

removed equations:
OMEGAo\p.f = OMEGAo;
Se1\p.e = Se1\effort;
WOBo\p.e = WOBo;
ZeroJunction2\p1.f = OMEGAo;
OMEGA\p1.f = OMEGA\flow;
OneJunction\p1.e = k_torsional\p.e;
PowerDemux\input.e = Se1\effort;
V\p1.f = V\flow;
V\p2.e = WOBo;
OMEGA\p2.f = OMEGA\flow;
OMEGA\p3.f = OMEGA\flow;
V\p2.f = V\flow;
V\p3.f = V\flow;
J\p.f = OMEGA\flow;
omega = OMEGA\flow;
OneJunction\p2.e = k_torsional\p.e;
M\p.f = V\flow;
v = V\flow;
ZeroJunction3\p1.e = PowerDemux\output1.e;
ZeroJunction4\p1.e = PowerDemux\output2.e;
WOBo\p.f = V\flow;
ZeroJunction2\p2.f = OMEGA\flow;
ZeroJunction2\p3.e = k_torsional\p.e;
ZeroJunction3\p2.f = OMEGA\flow;
ZeroJunction4\p2.f = V\flow;
ZeroJunction2\p1.e = k_torsional\p.e;
ZeroJunction3\p2.e = PowerDemux\output1.e;
ZeroJunction4\p2.e = PowerDemux\output2.e;
WOBo\flow = V\flow;
ZeroJunction2\effort = k_torsional\p.e;
ZeroJunction3\p1.f = OMEGA\flow;
ZeroJunction3\effort = PowerDemux\output1.e;
ZeroJunction4\p1.f = V\flow;
ZeroJunction4\effort = PowerDemux\output2.e;
OMEGAo\p.e = k_torsional\p.e;
PowerDemux\output1.f = OMEGA\flow;
PowerDemux\output2.f = V\flow;

```
OneJunction\p2.f = k_torsional\p.f;
OMEGA\p3.e = PowerDemux\output1.e;
V\p3.e = PowerDemux\output2.e;
OneJunction\p1.f = k_torsional\p.f;
ZeroJunction2\p2.e = k_torsional\p.e;
OMEGAo\effort = k_torsional\p.e;
OneJunction\flow = k_torsional\p.f;
ZeroJunction2\p3.f = k_torsional\p.f;
Se1\p.f = PowerDemux\input.f;
V\p1.e = M\p.e;
OMEGA\p2.e = k_torsional\p.e;
Se1\flow = PowerDemux\input.f;
OMEGA\p1.e = J\p.e;
```

A.2. 20-Sim Code for Variant 2

```
                    //Bit_rock_parameters//

parameters
        real Bit_radius = 0.0156;
        real Zeta = 0.8269;
        real Epsilon = 116728615.4469;
        real Mu = 0.25;
        real Gamma = 7.4473;
        real Blade_number = 2;
        real Sigma = 11682235.0919;
        real Flat_lenght = 0.00488;
variables
        real global a;
        real global zeta;
        real global epsilon;
        real global mu;
        real global gamma;
        real global n;
        real global sigma;
        real global l;
                    //Drillstring_parameters//

parameters
        real Rotary_Interia = 0.01764155;
        real Mass_Top = 36.94922;
        real Mass_Bottom = 8.56905;

variables
        real global J;
        real global MTOP;
        real global MBOT;

                    //Top_Imposed_Parameters//

parameters
        real top_omega = 26.0132;
        real top_WOB = 362.4718741;
        real Bottom_WOB = 84.0623805;
        real initial_angle = 0;
        real plates = 7;
        real pump_flowrate_gpm=23.954;
```

```
        real bottomhole_pressure_psi= 105;

variables
        real global Fp;
        real global Fbhp;
        real global mass_plates;
        real global WOB_plates;
        real global OMEGAo;
        real global WOBo;
        real global WOBo1;
        real global phio;

                        //Continuous-time equations//

initial equations:
//define initial values of variables from bit-rock parameters//
a = Bit_rock_parameters\Bit_radius;
zeta = Bit_rock_parameters\Zeta;
epsilon = Bit_rock_parameters\Epsilon;
mu = Bit_rock_parameters\Mu;
gamma = Bit_rock_parameters\Gamma;
n = Bit_rock_parameters\Blade_number;
sigma = Bit_rock_parameters\Sigma;
l = Bit_rock_parameters\Flat_lenght * n;

//take bit-rock variables to Matlab for future bit-rock model calculations//
toMatlab (a, 'a');
toMatlab (zeta, 'zeta');
toMatlab (epsilon, 'epsilon');
toMatlab (mu, 'mu');
toMatlab (gamma, 'gamma');
toMatlab (n, 'n');
toMatlab (sigma, 'sigma');
toMatlab (l, 'l');

//define initial values of variables from drillstring parameters//
J = Drillstring_parameters\Rotary_Interia;
MTOP = Drillstring_parameters\Mass_Top;
MBOT = Drillstring_parameters\Mass_Bottom;

//Define values for hydraulic forces//
Fp = (0.001 * exp (0.339 * Top_Imposed_Parameters\pump_flowrate_gpm)) * 4.44822;
```

```
Fbhp = (0.001 * (((0.7 * Top_Imposed_Parameters\bottomhole_pressure_psi ^ 2) - (7.4 *
Top_Imposed_Parameters\bottomhole_pressure_psi)) + 93.8)) * 4.44822;
//Calculate applied WOB//
mass_plates = 2.2 + (Top_Imposed_Parameters\plates * 1.5);
WOB_plates = ((1.0456 * mass_plates ^ 3) - (27.147 * mass_plates ^ 2)) + (291.05 *
mass_plates);

//define initial values of variables from top imposed parameters//
OMEGAo = Top_Imposed_Parameters\top_omega;
WOBo = Top_Imposed_Parameters\top_WOB + WOB_plates;
WOBo1 = Top_Imposed_Parameters\Bottom_WOB;
phio = Top_Imposed_Parameters\initial_angle;

//create an empty matrix for OMEGA, PHI, V, U, time, WOB, TOB, tn, and D historic
values in Matlab//
doMatlab ('OMEGA=[];');
doMatlab ('PHI=[];');
doMatlab ('V=[];');
doMatlab ('U=[];');
doMatlab ('time=[];');
doMatlab ('WOB=[];');
doMatlab ('TOB=[];');
doMatlab ('tn=[];');
doMatlab ('D= [];');

//calculate steady state delay time and take values to matlab //
tno = (2 * pi) / (OMEGAo * n);
toMatlab (tno, 'tno');

//Set initial values in Matlab for bit-rock cases functions//
doMatlab ('Hd=1;');
doMatlab ('Hw=1;');
doMatlab ('Hv=1;');
doMatlab ('Hw2=1;');
```

dynamic equations:

```
//take values of omega, phi, v, u and time to Matlab and fill in historical values matrix//
toMatlab(omega,'omega');
doMatlab ('OMEGA=[OMEGA omega];');
toMatlab (phi, 'phi');
doMatlab ('PHI=[PHI phi];');
toMatlab (time, 't');
doMatlab ('time=[time t];');
```

```
//calculate depth of cut from historical values//
doMatlab ('if phi<(2*pi/n);
                d=dno;tn=[tn tno];
        else;
                phit_tn=phi-(2*pi/n);                //find delay angle//
                t_tn=interp1q(PHI, time,phit_tn);    //find delay time//
                ut_tn=interp1q(time, U,t_tn);        //find delayed axial position//
                d=n*(u-ut_tn);                       //compute depth of cut//
                tn=[tn (t-t_tn)];                    //fill in delay time matrix//
        end;
                D=[D d];');                          //fill in depth of cut matrix//

//calculate current value for bit-rock cases functions//
doMatlab ('Hd=1/(1+exp((-200000*d)-1.5));
                Hw=1/(1+exp((-200000*omega)-1.5));
                Hv=1/(1+exp((-200000*v)-1.5));
                Hw2=tanh((70000*omega)+2);');

//take all required values for WOB and TOB from matlab to 20-sim//
fromMatlab (d, 'd');
fromMatlab (Hd, 'Hd');
fromMatlab (Hw, 'Hw');
fromMatlab (Hv, 'Hv');
fromMatlab (Hw2, 'Hw2');
doMatlab ('V=[V v];');
toMatlab (u, 'u');
doMatlab ('U=[U u];');
```

bond graph equations:

```
Fp_Fbhp\p.e = -(Fp + Fbhp);
C\p.e = C\state / C\c;
pVard_Stiffness\p.e = pVard_Stiffness\state * pVard_Stiffness\k;
OMEGA\flow = J\state / J;
V\flow = MBOT\state / MBOT;
MTOP\p.f = MTOP\state / MTOP;
WOBc = ((((a * zeta) * epsilon) * d) * Hd) * Hw;
WOBf = (((a * l) * sigma) * Hv) * Hd;
TOBc = (((((a ^ 2) * epsilon) * d) * Hd) * Hw) / 2;
TOBf = ((((((((a ^ 2) * gamma) * mu) * l) * sigma) * Hv) * Hd) * Hw2) / 2;
WOB = WOBc + WOBf;
TOB = TOBc + TOBf;
Se1\effort = [-TOB; -WOB];
```

```
[PowerDemux\output1.e; PowerDemux\output2.e] = Se1\effort;
Rack_pinion_Resistance\p.e = Rack_pinion_Resistance\r * MTOP\p.f;
C\p.f = OMEGAo - OMEGA\flow;
pVard_Stiffness\p.f = MTOP\p.f - V\flow;
PowerDemux\input.f = [OMEGA\flow; V\flow];
Seal_resistance_axial\p.e = Seal_resistance_axial\r * V\flow;
R\p.e = R\r * pVard_Stiffness\p.f;
R1\p.e = R1\r * C\p.f;
OneJunction4\p3.e = pVard_Stiffness\p.e + R\p.e;
OneJunction8\p3.e = C\p.e + R1\p.e;
MTOP\p.e = (WOBo - OneJunction4\p3.e) - Rack_pinion_Resistance\p.e;
MBOT\p.e = (((Fp_Fbhp\p.e + OneJunction4\p3.e) + PowerDemux\output2.e) +
WOBo1) - Seal_resistance_axial\p.e;
J\p.e = PowerDemux\output1.e + OneJunction8\p3.e;

system equations:
C\state = int (C\p.f, C\state_initial);
J\state = int (J\p.e, J\state_initial);
MBOT\state = int (MBOT\p.e, MBOT\state_initial);
MTOP\state = int (MTOP\p.e, MTOP\state_initial);
phi = int (OMEGA\flow, phio);
pVard_Stiffness\state = int (pVard_Stiffness\p.f, pVard_Stiffness\state_initial);
u = int (V\flow, u_initial);

removed equations:
OneJunction4\p1.e = pVard_Stiffness\p.e;
OneJunction8\p1.e = C\p.e;
OMEGAo\p.f = OMEGAo;
Se1\p.e = Se1\effort;
WOBo\p.e = WOBo;
WOBo1\p.e = WOBo1;
V\p1.e = Fp_Fbhp\p.e;
OneJunction9\p1.f = OMEGAo;
OMEGA\p1.f = OMEGA\flow;
OneJunction2\p1.f = MTOP\p.f;
PowerDemux\input.e = Se1\effort;
V\p3.f = V\flow;
V\p4.e = WOBo1;
OneJunction2\p4.e = WOBo;
OMEGA\p2.f = OMEGA\flow;
OMEGA\p3.f = OMEGA\flow;
OneJunction2\p2.f = MTOP\p.f;
OneJunction2\p3.f = MTOP\p.f;
```

```
OneJunction2\p4.f = MTOP\p.f;
OneJunction9\p2.f = OMEGAo;
V\p1.f = V\flow;
V\p4.f = V\flow;
V\p5.f = V\flow;
V\p6.f = V\flow;
J\p.f = OMEGA\flow;
omega = OMEGA\flow;
OneJunction2\flow = MTOP\p.f;
OneJunction9\flow = OMEGAo;
MBOT\p.f = V\flow;
v = V\flow;
Fp_Fbhp\p.f = V\flow;
ZeroJunction5\p1.f = MTOP\p.f;
ZeroJunction1\p1.f = OMEGAo;
ZeroJunction3\p1.e = PowerDemux\output1.e;
ZeroJunction4\p1.e = PowerDemux\output2.e;
Rack_pinion_Resistance\p.f = MTOP\p.f;
WOBo1\p.f = V\flow;
WOBo\p.f = MTOP\p.f;
ZeroJunction1\p2.f = OMEGA\flow;
ZeroJunction3\p2.f = OMEGA\flow;
ZeroJunction4\p2.f = V\flow;
ZeroJunction5\p3.f = V\flow;
V\p2.f = V\flow;
ZeroJunction3\p2.e = PowerDemux\output1.e;
ZeroJunction4\p2.e = PowerDemux\output2.e;
Fp_Fbhp\flow = V\flow;
WOBo\flow = MTOP\p.f;
WOBo1\flow = V\flow;
ZeroJunction3\p1.f = OMEGA\flow;
ZeroJunction3\effort = PowerDemux\output1.e;
ZeroJunction4\p1.f = V\flow;
ZeroJunction4\effort = PowerDemux\output2.e;
PowerDemux\output1.f = OMEGA\flow;
PowerDemux\output2.f = V\flow;
OneJunction2\p3.e = Rack_pinion_Resistance\p.e;
Seal_resistance_axial\p.f = V\flow;
OneJunction8\p3.f = C\p.f;
OMEGA\p3.e = PowerDemux\output1.e;
V\p5.e = PowerDemux\output2.e;
OneJunction4\p3.f = pVard_Stiffness\p.f;
OneJunction4\p1.f = pVard_Stiffness\p.f;
```

```
OneJunction8\p1.f = C\p.f;
OneJunction4\flow = pVard_Stiffness\p.f;
OneJunction8\flow = C\p.f;
ZeroJunction5\p2.f = pVard_Stiffness\p.f;
ZeroJunction1\p3.f = C\p.f;
Se1\p.f = PowerDemux\input.f;
V\p2.e = Seal_resistance_axial\p.e;
OneJunction4\p2.f = pVard_Stiffness\p.f;
OneJunction8\p2.f = C\p.f;
Se1\flow = PowerDemux\input.f;
R\p.f = pVard_Stiffness\p.f;
R1\p.f = C\p.f;
OneJunction4\p2.e = R\p.e;
OneJunction8\p2.e = R1\p.e;
ZeroJunction1\p3.e = OneJunction8\p3.e;
ZeroJunction5\p2.e = OneJunction4\p3.e;
ZeroJunction1\p1.e = OneJunction8\p3.e;
ZeroJunction5\p1.e = OneJunction4\p3.e;
ZeroJunction5\p3.e = OneJunction4\p3.e;
ZeroJunction1\effort = OneJunction8\p3.e;
ZeroJunction5\effort = OneJunction4\p3.e;
OneJunction2\p2.e = OneJunction4\p3.e;
OneJunction9\p2.e = OneJunction8\p3.e;
V\p6.e = OneJunction4\p3.e;
ZeroJunction1\p2.e = OneJunction8\p3.e;
OneJunction9\p1.e = OneJunction8\p3.e;
OMEGAo\p.e = OneJunction8\p3.e;
OneJunction2\p1.e = MTOP\p.e;
V\p3.e = MBOT\p.e;
OMEGA\p2.e = OneJunction8\p3.e;
OMEGAo\effort = OneJunction8\p3.e;
OMEGA\p1.e = J\p.e;
```

APPENDIX B

PROCEDURE FOR TORQUE CALIBRATION PERFORMED ON LAB SCALE DRILL RIG MOTOR

B.1. Test objectives

To characterize the output Torque of the lab scale drill rig motor based on current consumption and measured angular speed.

B.2. Test equipment and arrangement

- Lab scale drill rig arrangement at atmospheric pressure. (see Figure B.1)
- Sample holder (see Figure B.1)
- MC6 Load and torque Cell (see Figure B.2)

Figure B.1. Lab scale drill rig and sample holder.

Figure B.2. MC6 Load and torque cell

B.3. Test procedure

- Drilling was performed with load and torque cell under the sample holder in order to transmit TOB and WOB to the cell.
- 14 drilling tests were performed covering all the range of applied *WOB*
- Low flowrate for cuttings removal was used in order to avoid any hydraulic force.
- Rotary speed was set at 300 rpm
- The following variables were measured:
    - Motor Current
    - Motor speed
    - Axial Load under sample (Dynamic WOB)
    - Torque under sample (Dynamic TOB)

B.4. Results

An equal timeframe was taken from each plot where constant values where observed. Root mean square (RMS) of current was calculated as:

$$i_{rms} = \sqrt{\frac{1}{n}\left({i_1}^2 + {i_2}^2 + \cdots + {i_n}^2\right)}$$

(B.1)

where

i_{rms}`	RMS of motor current
n	number of data points
i_n	instantaneous value of motor current

Average load and torque was obtained from the load cell. Rotary speed was calculated from the peaks in the acceleration plot. Values of Torque vs. Motor speed and Torque vs. RMS current were plotted (see Figure B.3)

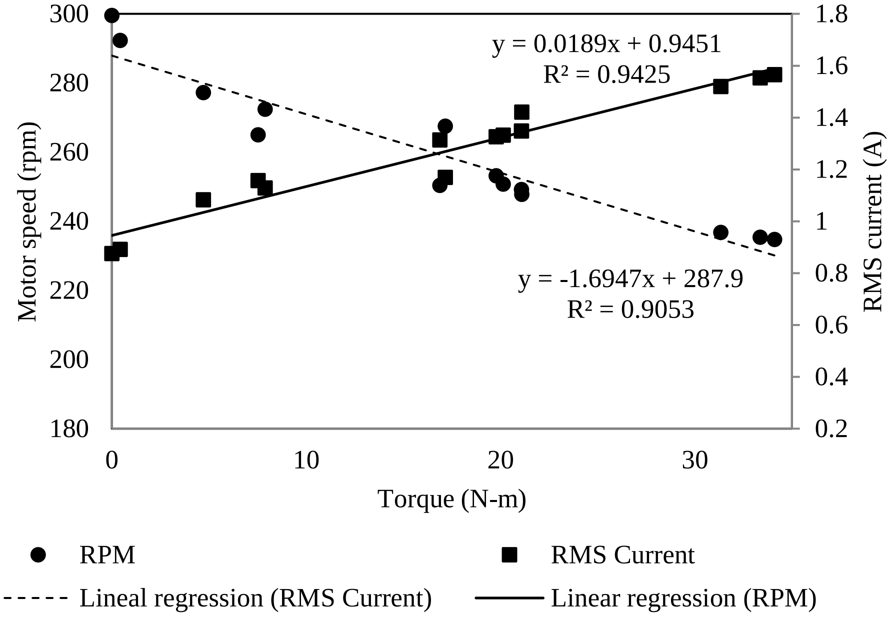

Figure B.3. Torque vs. Motor speed and RMS current

Using the least square method, a linear regression was calculated for the torque/speed and torque/current curves. Equations of the straight lines are shown in Figure B.3. From torque/speed and torque/current linear regressions, torque is defined as a function of speed and current as:

$$T(\Omega) = \frac{287.9 - \Omega}{1.6947} \qquad \text{(B.2.)}$$

$$T(i_{rms}) = \frac{i_{rms} - 0.9451}{0.0189} \qquad \text{(B.3)}$$

Assuming that both angular speed (Ω) and current (i_{rms}) contribute equally to torque values, equations B.2 and B.3 are combined. The resultant function is:

$$T(\Omega, i_{rms}) = 59.985 - 0.295\Omega + 26.48 i_{rms} \qquad \text{(B.4)}$$

Equation B.4 can be used in the future for all drilling experiments performed in the lab scale drilling rig in order to find output torque values from current and speed measurements.

APPENDIX C

Dynamic Analysis of a Deep Water Marine Riser using Bond Graphs

Rosana A. Reyes
M.Eng. Candidate
Faculty of Engineering and Applied Science
Memorial University
St. John's, NL Canada A1B 3X5
rarn02@mun.ca

Geoff Rideout
Associate Professor
Faculty of Engineering and Applied Science
Memorial University
St. John's, NL Canada A1B 3X5
gdrideout@mun.ca

ABSTRACT

This paper describes a lumped segment model of a deep water riser using the bond graph method. The model allows calculation of the dynamic response, and resulting normal stress, of the riser pipe due to bending, tension and compression. Marine risers are subjected to diverse dynamic loads such as the force exerted by the waves and the vessel's motion. The cyclic nature of these loads will induce fluctuating stresses that, after a certain time, will result in failure by fatigue. Therefore, the dynamic analysis of the riser's response is very important for the prediction of the fatigue life. In this paper, the riser is modeled as a beam with both lateral and axial degrees of freedom. The beam is divided into lumped segments that are modeled as planar rigid bodies joined together by springs representing the pipe's compliance in shear, tension, and bending. An analysis of the common external loads is made. A 16-inch diameter marine riser for deep water conditions is modeled to verify the usefulness of the lumped model technique, and then simulated using the software 20-Sim©. Results show that the external axial loads significantly affect not only the axial response but also the lateral vibrations.

Author Keywords

Riser; top tension; bond graph; wave force; stress.

ACM Classification Keywords

I.6.3 Applications

INTRODUCTION

A marine riser is a subsurface pipe employed in offshore drilling and production for connecting the drilling or production unit with the blow-out prevention stack (BOP) that is placed on the seabed [1]. Marine risers are subjected to static loads such as their weight, the top tension, and internal and external pressures, but also to loads whose amplitude changes in time, for example, the force exerted by the sea waves or the motion of the floating vessel [2]. These loads may not be large enough to overcome the allowable stress of the pipe structure but their cyclic nature will induce fluctuating stresses that, after a certain time, will result in failure by fatigue. Therefore, the dynamic analysis of these loads and the riser's response is very important for the prediction of the fatigue life of these structures.

Early riser design and analysis studies were done primarily in the static field highlighting the importance of the top tension in a riser to prevent its deformation due to the weight of the riser itself. These studies also recognized some dynamic effects but argued that they were negligible for shallow depths (<330 m). As oil resources became more available in deeper water, and operations moved towards this field, the dynamic effects were considered more and more [3]. The complexity of dynamic analysis was also more achievable due to the advance of computer technology [4]. Previous studies have had different approaches to the analysis model for a riser but two of them seem to be very common. Numerical integration of the motion equation along the length of the riser [1] and Finite Differences Scheme. In the latter approach the riser is divided into elements of finite length with discrete degrees of freedom at the connections and the resulting equations of each element are solved simultaneously [2, 5, 6].

As the computing capacity increases, the use of finite element methods has become the most commonly used technique and the riser's dynamics are now coupled with the dynamics of the vessel which are also simulated and controlled under dynamic positioning systems [7]. Nowadays, dynamic analyses are performed not only in order to study the response under fluctuating loads but also to design controllers that can accurately regulate the horizontal displacement of the risers to prevent collision with other offshore structures. [8]

This paper describes a multi-body lumped segment technique for modeling deep water risers using the bond graph method. The purpose of this procedure is to calculate the dynamic response and subsequent normal stress of the riser pipe due to bending, tension and compression; considering relevant steady and time-varying loads. The software 20-Sim© is used to simulate a riser under realistic conditions.

MODEL ANALYSIS

In this paper, the riser is modeled as a combined beam/rod subjected to lateral and axial loads, some of which are distributed along the system. An analytical solution would require solution of partial differential equations. In this paper, a numerical solution is obtained by a lumped segment approximation that captures axial, bending and shear motions.

The global coordinate system used for the riser is illustrated in Figure 1. The vertical coordinate, *x*, has its origin at the still water level which has also been selected as the top of the riser. This coordinate is positive downward. The horizontal coordinate, *y*, is measured from the center of the riser at its base as shown in Figures 1 and 2.

The riser is represented by a series of rigid bodies of equal length; each rigid body has the same properties as the corresponding proportion of the riser pipe and its contents. As the number of segments approaches infinity, the behavior of the lumped segment model will converge to that of the continuous riser. The length of each segment will be defined by the number of rigid bodies, *n*. For each segment, three points are defined: A and B in the top and the bottom respectively and G in the center of mass of the element. Moments of inertia are calculated about points G. Points B of element *i* and A of element *i+1* are linked by one torsional and two linear springs. The torsional spring represents the bending compliance or flexural rigidity of the beam over the plane *x-y*, and the linear springs in *x* and *y* represent the axial and shear compliance respectively. Each spring is complemented with a damper acting in parallel to it that acts as the pipe material damping. Figure 2 shows how segments are joined by the mentioned springs and includes simple supports in the ends that model the rotary joints of the ends of the riser. For simplicity purposes, the dampers are not shown in the figure.

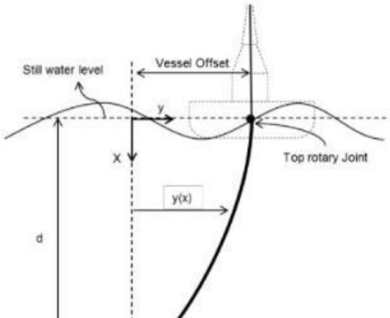

Figure 1. Coordinate system and riser arrangement

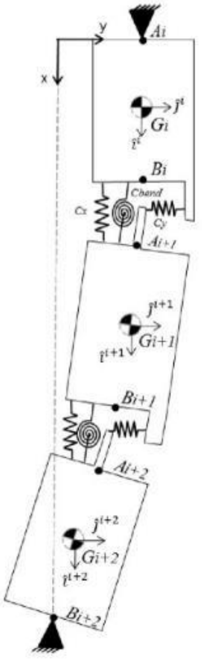

Figure 2. Multibody elements joint by shear, bending and axial compliance.

As described in the next section, the velocity and force vectors for each segment are expressed in inertial components. While the actual direction of a vector such as the axial spring force would be aligned with the segment and not with the inertial components, the assumption that the vector is aligned with the inertial *x* direction – as shown in Figure 2 – introduces a negligible error if small lateral deflections of the riser are assumed.

Riser Compliance

The numerical formulation for the compliance of the springs and the inertia of the masses is developed in [3]; the resulting parameters for the compliance are the following:

$$C_x = \frac{EA_p}{l} \tag{1}$$

$$C_y = \frac{\kappa G A_p}{l} \tag{2}$$

$$C_{bend} = \frac{EI}{l} \tag{3}$$

where

C_x = axial compliance of riser section
C_y = shear compliance of riser section
C_{bend} = bending compliance of the riser section
E = Young's modulus of pipe
A_p = cross sectional area of the riser pipe
l = length of the pipe segment
G = shear modulus pipe

κ = shear coefficient
I = area moment of inertia of the cross section

Riser Inertia

The translational inertia parameters of the lumped segments are defined as their mass. In the formulation of the mass equations, two terms are considered: the structural mass of the riser pipe m_p and the internal fluid mass m_m. For the horizontal inertia, another term is considered, the hydrodynamic added mass, m_h. This term was introduced by Morison *et al.* [9] and accounts for the accelerative force proportional to the mass of water displaced by the riser. The resulting equation for the inertia is the sum of these three parameters:

$$I_x = \frac{\pi l}{4}\left[\rho_p({D_o}^2 - {D_i}^2) + \rho_m {D_i}^2 + C_m \rho_w {D_o}^2\right] \quad (4)$$

$$I_y = \frac{\pi l}{4}\left[\rho_p({D_o}^2 - {D_i}^2) + \rho_m {D_i}^2\right] \quad (5)$$

where

ρ_p, ρ_m, ρ_w = mass density of the pipe, the drilling mud and the water.
D_o, D_i = external and internal diameter of the pipe.
C_m = inertia coefficient for a fixed cylinder in an accelerating flow.

For the rotary inertia, the properties of the pipe, mud, and hydrodynamic mass are also to be taken into consideration. The resulting equation is:

$$I_{rotary} = \frac{\pi l}{64}\left[\rho_p({D_o}^4 - {D_i}^4) + \rho_m {D_i}^4 + C_m \rho_w {D_o}^4\right] \quad (6)$$

Riser Damping

Damping in the riser is due to the material damping associated with the hysteresis energy losses in the material when it experiences fluctuating stresses. For convenience it is usually assumed as viscous in nature and expressed as a percentage of the critical damping [10]. In this paper, the material damping is modeled as a resistance element that has been tuned to give approximately 1% to 3% damping ratio for the first few modes of bending and axial vibration.

MULTIBODY BOND GRAPH MODEL

Figure 3 shows a pipe segment with the velocity vector of points G and A. If rotation of the segment is considered as a vector going out of the page, from this diagram the velocity of the connection point A can be defined as:

$$\begin{bmatrix} Vx_A \\ Vy_A \end{bmatrix} = \begin{bmatrix} Vx_G \\ Vy_G \end{bmatrix} + \begin{bmatrix} AG\ sin\theta\ \dot{\theta} \\ -AG\ cos\theta\ \dot{\theta} \end{bmatrix} \begin{matrix} \hat{\imath} \\ \hat{\jmath} \end{matrix} \quad (7)$$

where

Vx_A, Vx_G = vertical component of the velocity of A and G.
Vy_A, Vy_G = horizontal component of the velocity of A and G.
AG = distance between points A and G
θ = angular displacement of the segment

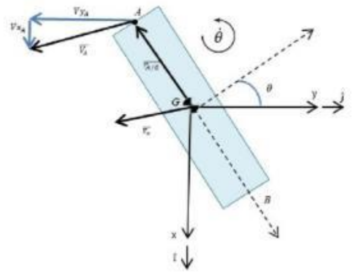

Figure 3. Velocity vectors and relative position vector of a segment

The velocity of point B is defined similarly. A single element can undergo both transverse and axial motion, with the assumption that the transverse and axial compliances separately derived for decoupled beam and rod elements in Karnopp *et al.* [11] are applicable. The constraints defined previously will be modeled as modulated transformers that will relate the lateral and longitudinal velocities of each segment through their angular velocity. The changing modulus is dependent on the current value of angular displacement of the segment. Having defined the endpoint velocities, their relative motions are constrained by axial, bending and shear springs and dampers as shown in Figure 2.

Figure 4 illustrates the bond graph for two segments linked together. The formulation for a complete riser consists of joining as many elements as required and including sources of flow or effort on the ends as the desired boundary conditions. For some boundary conditions, derivative causality might be introduced; this can be solved by applying the Karnopp–Margolis method [12] that consists of adding some parasitic compliance elements in order to avoid non-preferred *MTF* causality and algebraic loops; the left side of Figure 4 shows how parasitic elements can be added, these are optional elements.

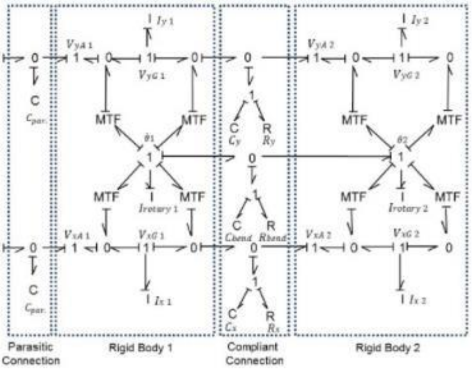

Figure 4. Bond graph of two elements joined by a compliant connection

The top row of the bond graph represents the velocities and elements in the shear (y) direction, the center row counts for the rotation (bending) of the riser and the bottom row represents the axial (x) direction.

EXTERNAL LOADS MODEL

Axial Loads

The loads applied in the x direction are: the gravity force due to the weight of the riser and its contents, the buoyancy force that water exerts on the riser, and the top tension that the vessel must maintain in order to prevent buckling of the riser.

Gravity force

The gravity force acts in the positive x direction and it is proportional to the weight of the riser and its contents. In the bond graph model this would be equivalent to including a source of effort in each $\mathrm{Vx_G}$ 1-junction.

$$W_f = \frac{g\pi l}{4}\left[\rho_p\left({D_o}^2 - {D_i}^2\right) + \rho_m {D_i}^2\right] \tag{8}$$

where

g = acceleration of gravity ≈ 9.810 m/s^2.

Buoyancy Force

Buoyancy counts for the vertical force that the water exerts on the submerged bodies. According to Archimedes' principle this force is equal to the weight of the volume of liquid displaced by the object. In the coordinate system defined in this paper, the buoyancy force has a negative value and it is applied on the $\mathrm{Vx_G}$ 1-junction of the body's bond graph.

$$W_b = \frac{g\pi l}{4}\rho_w {D_o}^2 \tag{9}$$

Top Tension

Long slender risers need a vertical tension applied in the top in order to avoid buckling or collapse due to the weight of the pipe. The top tension is set proportional to the total riser weight and drilling fluid in the water [3]. Some risers' configurations include buoyancy modules along the riser length that increase the buoyancy force and therefore reduce the required tension. For this analysis, a constant top tension will be considered, although a time varying tension could be included if, for example, the density of the internal fluid is expected to change. The constant top tension is calculated as follows:

$$T_{top} = (W_f - W_b)k_{tension} \tag{10}$$

where

$k_{tension}$ = top tension factor

The top tension factor is set between 0.8 and 1.4 by [3] as a practical range of interest; although in actual circumstances this value would be determined by the maximum capacity of the tensioning system.

For the bond graph modeling, top tension is applied as a constant source of effort in the $\mathrm{Vx_A}$ 1-junction of the top element.

Lateral Loads

The lateral loads applied in the riser are the wind force and the wave force. If the riser is assumed to be completely submerged, the wind force is negligible.

The forces exerted by the waves and the current on the riser are determined by the Morison equation [9], later modified by [3] to include the relative velocity between the water and the riser.

In his analysis, Gardner and Kotch [5] assume that the waves propagate only horizontally and the current only affects the water velocity in the y direction. That assumption is also considered in the present analysis.

The horizontal total horizontal force in an element is then:

$$F_{hyd} = \left[\rho_w C_m \frac{\pi}{4} {D_o}^2 \dot{u}\right] - \left[\rho_w C_m \frac{\pi}{4} {D_o}^2 \ddot{y}\right] + \left[\frac{1}{2}\rho_w C_D D_o (u - \dot{y})|u - \dot{y}|\right] \tag{11}$$

where

$\dot{u}, \ddot{y}$ = acceleration of the water and the riser, respectively
$u - \dot{y}$ = relative velocity between the water and the riser
C_D = drag coefficient

A detailed explanation of the terms of equation 11 can be found in [3] and [9].

The first term of the previous equation is neglected by most authors due to the fact that the wave induced water motion is negligible for deep waters [5, 6]; The second term has already been included in the inertial horizontal mass (see equation 4). Therefore, the third term, which is the drag force, is the only one considered.

From equation 11, *u(x,t)* is defined by Morison as:

$$u(x,t) = \frac{\pi H}{T}\frac{\cosh\frac{2\pi}{L}(d-x)}{\sinh\frac{2\pi d}{L}}\cos\frac{2\pi t}{T} + u_c(x) \tag{12}$$

where

H = wave height
L = wave length
T = wave period
t = time
d = still water depth
$u_c(x)$ = current profile function

Figure 5 shows the water velocity profile from 0 to 100 m deep at four different times (t) of the waveform. After 100m, the water velocity doesn't change, meaning that the acceleration is insignificant; this confirms the assumption made earlier to neglect the first term of equation 11. Also, for simplification purposes, the water velocity considered for the drag force calculations will be the value of *u(x,t)* at $x=x_G$ of each segment. Figure 6 shows an example of this simplification.

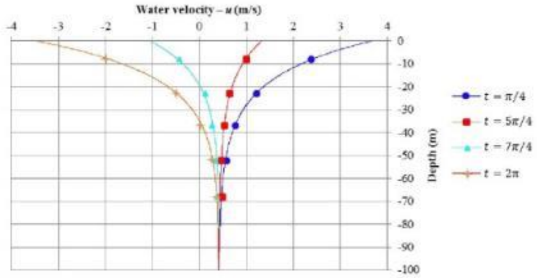

Figure 5. Water velocity profile from x= 0 to 100m.

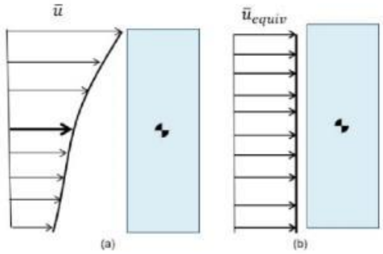

Figure 6. (a)Actual water velocity profile. (b) Equivalent water velocity profile

Equation 11 shows that the drag force is proportional to the relative velocity of the water and the riser; this can be modeled as a resistant element that dissipates energy from the system. The bond graph model of this element acting on the Vy_G 1-junction of each body is shown in Figure 7.

BOUNDARY CONDITIONS

Bottom joint

The model needs three boundary conditions in the bottom joint, two for the displacement in x and y and one for the rotation. For the lateral and axial displacement we simply set zero flow sources in the velocity of point B both in x and y. For the rotation there are two common options: a rigid connection that doesn't allow rotation and a rotary joint with certain stiffness value. For the first case, the modeling can be done by setting a torsional spring in the bottom segment with a very high stiffness, as if the segment was fixed to the seabed; for the second option, a lower rotary joint stiffness value is set. The present model used the latter approach to model a bottom joint that allows some rotation.

Top connection

The boundary conditions in the top will be defined by the way the riser is connected to the vessel and by the way the vessel responds to the wave movement. If we assume that the surge compensation system of the vessel is ideal then the riser will have zero lateral movement. Therefore a zero flow source for Vy_A of the top element has to be set. If a non-ideal surge compensation system for the vessel was modeled in a separate bond graph, connection of that model with the riser would occur at the Vy_A 1-junction through a modulated source of flow. Usually there is a horizontal static offset between the base of the riser and the position of the vessel. This can be modeled as a flow source that acts at the beginning of the simulation to obtain the desired offset and then is set to zero; this will bring an alteration of the initial response so the results should be considered after the oscillations due to this initial motion have passed. In the present model, the vessel offset is set to zero in order to study the influence of the current in the lateral response.

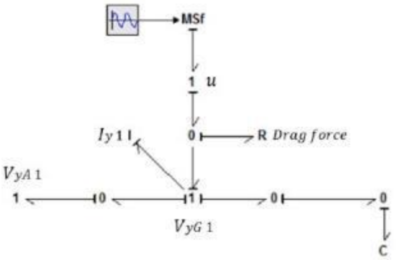

Figure 7. Bond graph model for water drag force

The rotation boundary condition of the top is defined in a similar way as in the bottom joint.

EXAMPLE OF A DEEP WATER RISER DYNAMIC ANALYSIS

A marine riser with an external diameter of 16 in (0.406 m) was modeled for deep water conditions to verify the usefulness of the lumped model technique, and then it was simulated using the software 20-Sim©. The Backward Differentiation Formula (BDF) method was selected as the integration method with tolerances of 10^{-6}. A 200 second simulation was completed in 12.24 seconds with 242,799 model calculations.

The simulation was done in order to obtain maximum horizontal displacements of the riser at different levels and the normal stress in those points due to bending, tension and compression. These outputs can be very useful for design and fatigue analysis purposes.

The values considered for the simulation are presented in Table 1. Values for the riser pipe are typical rather than representative of a specific riser, to show how the model can be used to study the effect of various factors on the riser response. During the simulation, some values were varied in order to see their effect on the response; this is specified in each case on the following sections.

Water depth (d)	920.5 m
Wave height (H)	10 m
Wave period (T)	8 s
Wave length (L)	100 m
Water density (ρ_w)	1025 kg/m^3
Coefficient of drag (C_D)	0.7
Current profile function $u_c(x)$	0.0005(d-x)
External diameter (D_o)	0.406 m
Internal diameter (D_i)	0.374 m
Pipe density (ρ_p)	8200 kg/m^3
Young Modulus (E)	207 GPa
Shear Modulus (G)	81.5 GPa
Mud density (ρ_m)	2214 kg/m^3
Number of segments (n)	10
Top tension factor (k_{top})	1.1
Rotary joints stiffness	50,000 rad/N-m
Top horizontal an velocity	0 m/s
Top vertical velocity	0 m/s

Table 1. Marine Riser Specifications

RESULTS AND DISCUSSIONS

The resulting simulation allows for calculation of the forces and moments in every compliant connection. Using these forces and the equations for stress calculation in beams, the normal stress due to axial and bending forces can be obtained, as well as the shear stress due to shear forces. Figure 8 shows the normal stress due to axial loads at different depths. The top plot represents the axial stress at a shallow level (46 m); it can be noticed that the average value is negative, which means tension stress. At a greater depth the average value of the axial stress is closer to zero. This can be explained by the equilibrium between the weight and the tension; the shallower segments experience a low column weight while still having the top tension so the total axial load will be in tension. The bottom segment will experiment all the weight of the pipe and mud column which will be balanced by the top tension that is almost the same value of the buoyant weight ($k_{tension}$=1.1). From this analysis we can conclude that the value of the top tension is a significant parameter to define what part of the riser is in tension stress and what part is in compression.

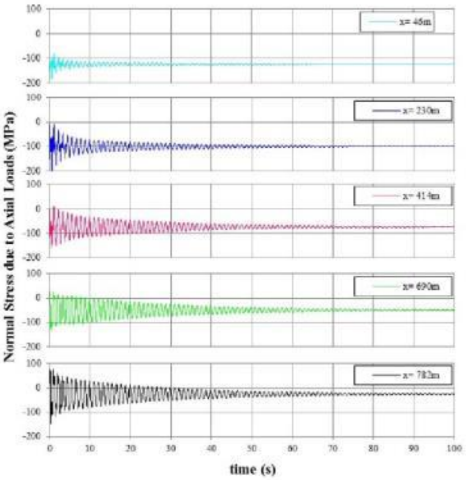

Figure 8. Normal stress due to axial loads at different depths

The horizontal displacements for the same depths are shown in Figure 9. Initial oscillations in the lateral response due to the current are observed; however, the drag force acts as a damping effect reducing the amplitude of the oscillations after a certain time.

The lateral displacement at three different times is plotted against the depth in Figure 10. From this figure it is possible to see the shape that the riser will have. Also in Figure 10, the maximum (extreme) displacement of each point is shown. The plot is shown to illustrate the location where the riser would experience the greater displacements. As expected, the greater displacement for this riser configuration is happening around the middle of the riser and in general the lateral displacements are very small compared to the total length of the riser. This result agrees with the initial assumption of small lateral deflections and confirms the suitability of inertial coordinates for this particular system.

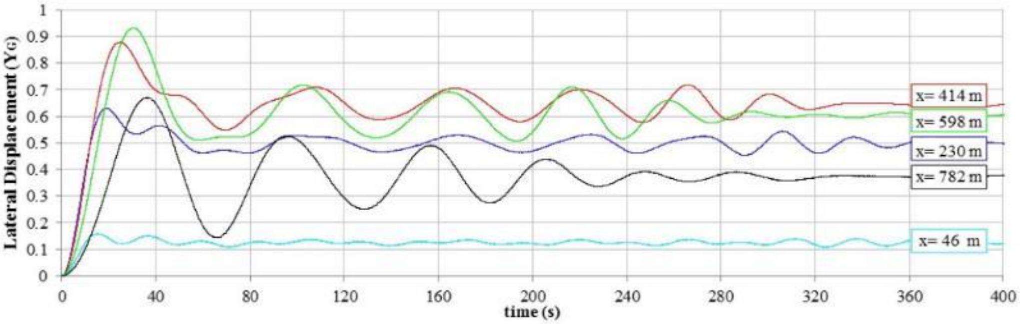

Figure 9. Horizontal Displacement at different depths

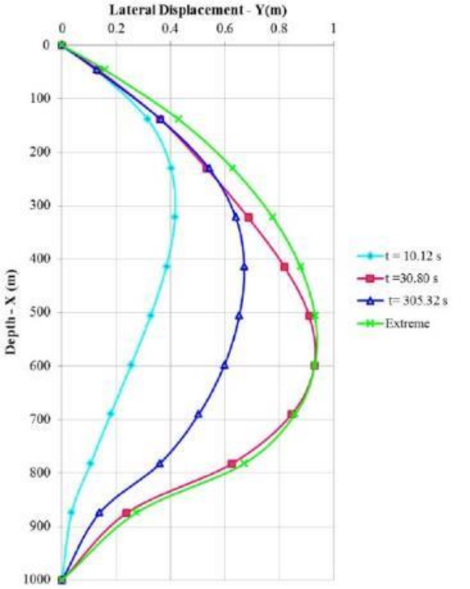

Figure 10. Displacement of the pipe at different times and maximum (extreme) displacement

Previous studies have highlighted the implication of top tension in the lateral response of the riser. Burke determined that a higher top tension would increase the bending stress along the riser [3]. Rao states that the axial load will have a direct effect on the natural frequency of the beam [13]. To verify this, the model was simulated with four different top tension factors. The lateral displacement of the riser at $x = 414$ m is shown in Figure 13 for each different top tension factor. The maximum lateral response and the natural frequency of the first mode of vibration of each top tension factor are presented in Table 2. The increased natural frequency stiffens the beam and as a consequence, the lateral displacements are smaller.

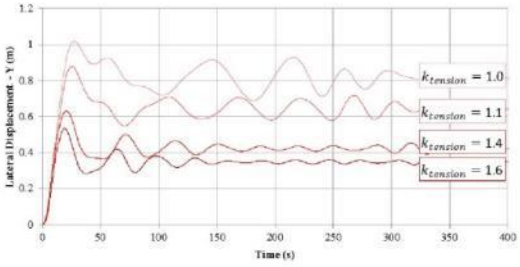

Figure 11. Lateral displacement at x = 414 m for different $k_{tension}$

$k_{tension}$	Max. Y_G (x = 414 m)	ω_{n1} (rad/s)
1	1.018	0.0758
1.1	0.879	0.1036
1.	0.631	0.1452
1.6	0.535	0.1646

Table 2. Maximum horizontal displacement at x = 414 m and natural frequency of the first mode of vibration for different values of $k_{tension}$

The total normal stress due to both bending and axial loads as well as the shear stress at $x = 414$ m is presented in Figure 12. As expected, the shear stresses are much smaller than the normal stress, small enough to be negligible. In fact, most of the previous riser analysis work utilizes the Euler-Bernoulli beam assumption [2, 3, 4, 5, 8, 14] which neglects shear deformation and the influence of rotary inertia (I_{rotary}). The model allows straightforward quantification of the effect of shear rather than reliance on only the experience and intuition of the modeler.

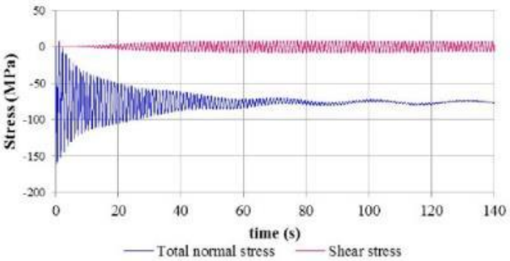

Figure 12. Total normal stress and shear stress at x = 414 m

One useful application of the model is to use the output for fatigue analysis and prediction of fatigue life of the riser based on the different conditions expected for service. Figure 13 shows the spectrum generated by a Fast Fourier Transform (FFT) of the normal stress that was shown previously in Figure 12. By obtaining the amplitude and frequency of every peak, an FFT based method of cycle counting for fatigue analysis can be performed as detailed in [15]. This technique is reported to be of great use in the offshore engineering field [16].

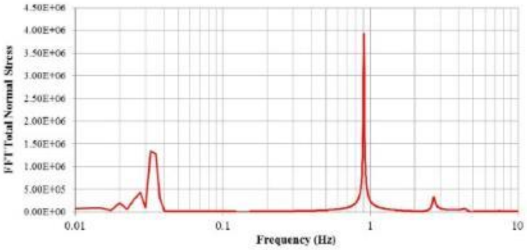

Figure 13. FFT analysis of total normal stress at x = 414 m

CONCLUSIONS

- The multi-body lumped segment model provides a practical way to evaluate the riser response resulting from dynamics of the vessel, the waves and the current.
- Modification of boundary conditions or external forces can be done easily by changing the flow and effort sources without altering the model equations.
- The model presented is capable of capturing coupling between axial and lateral deflections.
- The model requires low computing capacity due to the limited amount of lumps used.
- The top tension is a significant parameter to define what part of the riser is in tension and what part is in compression. For a long slender riser, this would allow for knowing the most convenient depth for the installation of buoyancy devices along the length of the riser. Dynamic analysis of the response can assist in the selection of the ideal value of top tension and thus is a useful aid in deep water riser design.
- The top tension has also shown to affect the lateral response. A very low top tension will increase the compression stress in the whole pipe leading to a reduction of the vibrations; however, having the entire riser in compression would lead to buckling and collapse. Similarly, very high tensions would also reduce the lateral vibrations at the expense of a high normal stress in the shallower sections.
- The model allows for straightforward prediction of quantities such as fluctuating normal and shear stress for use in fatigue analysis.
- Reformulating the model to resolve vectors along body-fixed coordinate frames rotating with each segment can be easily done with inclusion of an Eulerian Junction Structure (modulated gyrator), to improve accuracy when lateral deflections are significant compared to riser length.

Future work will continue the process of validating the model with respect to analytical solutions to verify that the multi body approach accurately captures coupling between axial and lateral deflections. The number of segments was chosen somewhat arbitrarily, and is approximately the minimum number required to capture the first two natural frequencies with reasonable accuracy. Optimizing the number of segments to manage the trade-off between computational efficiency and accuracy remains an area for further investigation.

REFERENCES

1. Chakrabarti, Subrata K. and Ralph E. Frampton. 1982. "Review of Riser Analysis Techniques." *Applied Ocean Research* 4 (2): 73-90.
2. Khan, Rizwan A. and Suhail Ahmad. 2010. "Fatigue Reliability Assessment of Marine Risers in Deep Offshore Fields in Indian Ocean." *Proc. ASME 2010 10th Biennial Conference on Engineering Systems Design and Analysis.*
3. Burke, Ben G. 1974. "An Analysis of Marine Risers for Deep Water." *Journal of Petroleum Technology* 26 (04): 455-465.
4. Hong, YP, M. Nakamura, Wataru Koterayama, and H. Osawa. 2002. "An Experimental and Numerical Study on Dynamics of Flexible Free Hanging Riser." *Proc. Pacific/Asia Offshore Mech. Symposium.* International Society of Offshore and Polar Engineers.
5. Gardner, To N. and MA Kotch. 1976. "Dynamic Analysis of Risers and Caissons by the Element Method." *Proc. Offshore Tech. Conference.*
6. Simmonds, DG. 1980. "Dynamic Analysis of the Marine Riser." Society of Petroleum Engineers.
7. Jensen, Gullik Anthon. 2010. "Offshore Pipelaying Dynamics." Doctoral Thesis. NTNU.
8. Rustad, Anne M., Carl M. Larsen, and Asgeir J. Sørensen. 2008. "FEM Modelling and Automatic Control for Collision Prevention of Top Tensioned Risers." *Marine Structures* 21 (1): 80-112.
9. Morison, JR, JW Johnson, and SA Schaaf. 1950. "The Force Exerted by Surface Waves on Piles." *Journal of Petroleum Technology* 2 (05): 149-154.
10. Stevenson, JD. 1980. "Structural Damping Values as a Function of Dynamic Response Stress and Deformation Levels." *Nuclear Engineering and Design* 60 (2): 211-237.
11. Karnopp, Dean C., Donald L. Margolis, and Ronald C. Rosenberg. 2012. *System Dynamics: Modeling, Simulation, and Control of Mechatronic Systems* John Wiley & Sons.
12. Karnopp, D. and D. Margolis. 1979. "Analysis and Simulation of Planar Mechanism Systems using Bond Graphs." *Journal of Mechanical Design* 101 (2): 187-191.
13. Rao, S. S. 2011. *Mechanical Vibrations* Prentice Hall.
14. Moe, Geir and BjØrn Larsen. 1997. "Dynamics of Deep Water Marine Risers-Asymptotic Solutions." *Proc. Int. Offshore and Polar Engineering Conference*. International Society of Offshore and Polar Engineers.
15. Iaw Kozien, Marek Stanis and Dariusz Smolarski. 2012. "Analitical Simulation of Application of FFT Based Spectral Method of Fatigue Cycle Counting for Multiaxial Stress on Example of Pulse Excited Beam." *Engineering Mechanics* 19 (5): 325-331.
16. Lee, Yung-Li. 2005. *Fatigue Testing and Analysis: Theory and Practice*. Vol. 13 Butterworth-Heinemann.

APPENDIX D

ARMA 15-764

Cuttings Analysis for Rotary Drilling Penetration Mechanisms and Performance Evaluation

Reyes, R., Kyzym, I., Rana P.S., Molgaard J. and Butt, S.D
Memorial University of Newfoundland, St. John's, NL, Canada

This paper was prepared for presentation at the 49th US Rock Mechanics / Geomechanics Symposium held in San Francisco, CA, USA, 28 June-1 July 2015.

ABSTRACT: Drillability or drilling efficiency of rock depends on three main parameter groups: rock characteristics, drill rig parameters and operational parameters. This paper describes the methodology of rock cuttings collection, preparation and their analysis for evaluation of the drilling efficiency and the performance of a passive Vibration Assisted Rotary Drilling (pVARD) tool in particular. The pVARD tool utilizes rock bit interactions to create axial vibrations in order to improve rock penetration. Analyses showed the correlation of such parameters as rate of penetration and weight on bit to cuttings size distribution. Several parameters such as mean particle size and coarseness index were used for numerical representation of cuttings size. Also a new particle size distribution bar diagram was proposed for cuttings samples comparison.

1. INTRODUCTION

One of the purposes of an effective drilling fluid system is to convey the cuttings from around the bit to the surface [1].

Several studies have been carried out on drilling cuttings as these are commonly used for the geological description of wells. Also studies on the petrophysical properties of formations, such as porosity and permeability have been conducted [2,3]. These studies have outlined the importance of cuttings analysis.

However, few studies have focused on studying cuttings as a mean of understanding the cutting action of the drilling tools. By analyzing the way that the cutter affects the different drilled formations and establishing relations between drilling parameters, drilling performance and cuttings, it is more feasible to make assumptions on the rock-bit interaction models for different drilling techniques.

Drilling performance is often defined as the drillability of a rock, that is, how fast a certain formation can be drilled. It is characterized by the rate of penetration (ROP). The parameters that define the drillability of a rock are usually separated in three groups: Rock characteristics (physical, mechanical, and micro-structural properties of the drilled formation), machine parameters (rotation, force, cuttings removal, etcetera.) and operating processes (drilling techniques, state of the equipment, etcetera.) [4].

In previous studies, some relations have been established between these three parameter groups and the cuttings analysis. Pfleider and Blake [5] concluded that the size and shape of cuttings are strongly related to ROP, i.e., the higher the ROP, the coarser the particles. This statement has been supported by other studies, both in percussion drilling and rotary drilling. [4,6].

The use of different drilling bits and drilling through different geological formations has also been evaluated in these studies. In general, there is unanimity in diamond drilling studies that the size of cuttings is related to the speed of advance. Most of these studies have also shown that this advance is proportional to the increase in rotary speed and the weight on bit during the drilling up to certain point. Above this point the relation tends to be inversely proportional due to the grinding of the particles [5].

In terms of quantifying and comparing the particle size of drill cuttings, several techniques have been developed, but the most used method has been to plot the cumulative percentage of undersized particles (or oversized) against particle size [6]. This graphical method has been done using different combinations of scales (linear, log, log-log) each with specific benefits depending on the application [7]. For powder materials and others obtained as a result of grinding, crushing and milling, the double logarithmic scale diagram, hereinafter called Rosin-Rammler (RR) distribution, has been shown to be well suited. Its graphical representation can be approximated to a straight line for better evaluation and comparison of samples [8].

The purpose of the present work is to describe a process for the analysis and comparison of cuttings sizes, its relationship with the drillability parameters and to apply this procedure to the evaluation of the performance of the passive Vibration Assisted Rotary Drilling (pVARD) tool, developed by the Advanced Drilling Technology Laboratory of Memorial University of Newfoundland.

2. BACKGROUND

Several Vibration Assisted Rotary Drilling (VARD) tools were designed and evaluated by the Advanced Drilling Laboratory. Multiple laboratory tests of reduced scale tools and various stages of numerical simulations were conducted.

Laboratory-scale prototype testing of a passive Vibration Assisted Rotary Drilling (pVARD) tool showed a considerable increase in the rate of bit penetration (ROP) by providing axial compliance at the bit-rock contact. To confirm the results obtained in the laboratory, a full-scale model of pVARD tool was designed and fabricated for further testing in field conditions.

3. FIELD WORK

Several potential field sites were identified and evaluated on the Avalon Peninsula of Newfoundland, Canada. The site selected for the present study was a quarry site owned and operated by Greenslades Construction in Conception Bay South.

Some preliminary studies indicated that the rocks drilled would be grey (green) and red shale with a basement of granite. During the field work, an Ingersoll Rand T3W drill rig was used. The rig was equipped with four drill bits that were used alternately during the drilling; however, this report will only focus on the results obtained during the drilling with PDC and RC bits. TSP bit data was not analyzed because of insufficient number of collected samples (less than 2 ft were drilled). Also percussive bit is out of interest, as the paper is focused only on rotary drilling.

The drilling of three wells was performed up to a depth of 121.92 m, 123.44 m and 63.73 m respectively. Several Bottom Hole Assembly (BHA) configurations were tested under different values of weight on bit (WOB). Other parameters like flowrate of the drilling fluid system and rotary speed of the drill string fluctuated because of the nature of drilling rig. During the drilling, cuttings were collected from the return fluid line (water) of the well into plastic containers. The latter were left for 5-10 minutes to give cuttings enough time to settle. After water was drained, cuttings were placed in separate sealed bags for each interval of drilling. Sometimes it was problematic to collect the samples that mainly consisted of very fine grains, as they required a very long time to settle. Consequently, the weight of those samples was relatively small (30-40 grams) compared to others (a few hundred grams). The following parameters were recorded for each interval: drilling depth, net drilling time, feed pressure, rotary speed, pump flowrate. The data was obtained either through the rig's control panel or through direct measurement.

To compensate for the fluctuations of rotary speed, a normalized ROP value was calculated as follows:

$$ROP_n = ROP\frac{100}{n} \qquad (1)$$

where ROP - is rate of penetration corresponding to rotary speed n.

This means that the normalized ROP's values correspond to a rotary speed of 100 rpm.

4. LABORATORY WORK

4.1 Procedure of cuttings size analysis

Since there is no a standard procedure for particle size analysis of cuttings from well drilling, the ASTM D422 Standard Test Method for Particle-Size Analysis of Soils [9] was adapted for this type of sample.

The cuttings were dried in an oven at the temperature of 60~70 °C. While drying, clumps formed in several samples. These were carefully crushed with a rubber mortar. A hundred grams, as a representative weight of the sample, was taken from each sample for sieving. If the sample weight was less than a hundred grams, the entire sample was sieved.

The set of sieves, included the following mesh sizes

- 2300 μm;
- 1180 μm;
- 850 μm;
- 425 μm;
- 300 μm;
- 100 μm.

An automatic shaker was used to provide the proper separation of different size fractions. Finally, all size fractions were weighed and put into separate plastic bags.

The cumulative weight percentage of passing particles was calculated for each size of mesh. A total of 79 sieved samples were obtained and a Rosin-Rammler (RR) diagram was plotted for each sample. From the RR diagram, using a Matlab code [8], the particle mean size (d') was taken as a size parameter; this is the particle size for which 36.79% of the particles are bigger. An example of RR diagram is shown on Fig. 3.

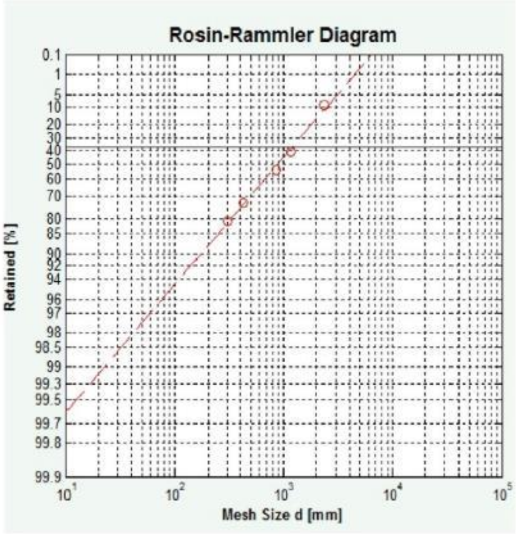

Fig. 3 - Rosin-Rammler (RR) distribution diagram

Another size parameter calculated is the coarseness index (CI); the coarseness index is a non-dimensional number obtained by adding the cumulative weight percentage of particles retained in each size of a set of sieves [10]. The CI will vary depending on the mesh sizes selected but will be suitable for comparison if the same sieves are used throughout the process. This parameter is very useful, because the overall sample can be characterized by one number, however it cannot provide complete information about the particle size distribution. The coarseness index calculation procedure is shown in Table 1.

A regular particle size distribution diagram (PSD) (Fig. 4) could be used for graphical representation of cuttings size distribution. Horizontal and vertical axes represent sieve mesh size and the cumulative percentage of particles finer than corresponding mesh size respectively. The horizontal axis is plotted on a logarithmic scale for a better distribution of the curve. The further right this curve is, the larger the particles are.

Table 1 Sieve analysis of Sample #36. Well 2 Grey Shale with quartz veins

Size (mm)	Weight (%)	Cumulative weight (%)
+2.36	7.52	7.52
-2.36+1.18	27.44	34.96
-1.18+0.850	12.83	47.79
-0.850+0.425	20.98	68.77
-0.425+300	7.34	76.11
-300	23.89	100.0
Σ	100	
Coarseness index (CI)		335.15

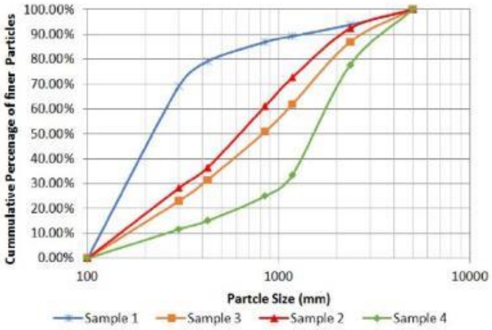

Fig. 4 – PSD diagram

From the diagram shown above it is possible to see that Sample 1 has the finest grains and Sample 4 has the coarsest. However, a PSD diagram can be confusing and the comparison of cuttings samples may be difficult, especially when representative curves intersect (Fig. 5).

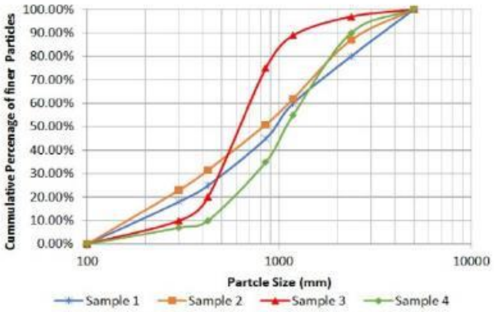

Fig. 5 – PSD diagram with crossing curves

For this reason, a bar particle size distribution (BPSD) diagram was proposed (Fig. 6). Each color represents a different size range in the sample. These diagrams present information in a simple and more convenient way. The bar diagram makes particle size distribution easier to perceive than a regular curve diagram. Also BPSD diagrams facilitate the comparison between different size fractions of different samples. This representation is more complete and precise than numerical parameters such as the coarseness index (CI) or mean particle size (d). Also, it was found that a bar PSD is much more useful than a regular PSD diagram, which might be quite confusing and may lead to inaccurate interpretations of the results.

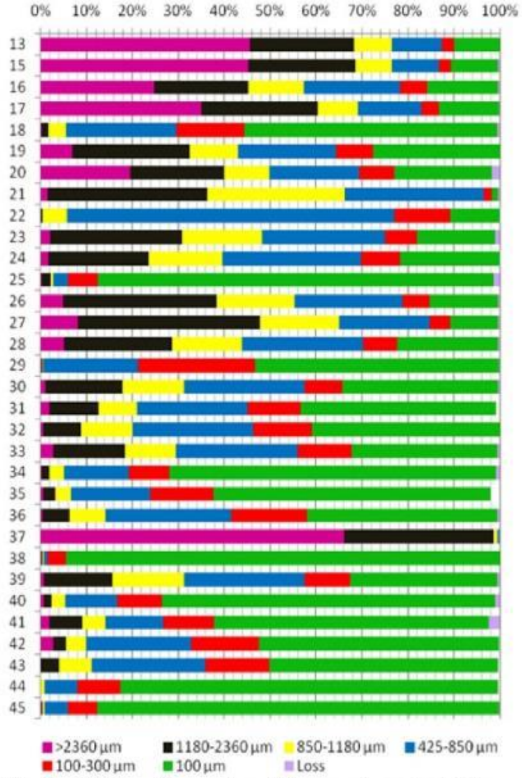

Fig. 6 – PSD bar diagram for cutting samples collected from Well 1

4.2 Geological Studies

Visual and microscopic analyses of cuttings allows for an opportunity to identify the type of drilled formation. For this purpose two microscopes (a Wild at 128x and Reichert ME4 at 2000x magnification) were used.

Analyses showed that the drilled formations were prevalently grey and red shale. The upper 60 m (200 ft) consist of pure grey shale. Deeper formations are mainly consecutively changing, thin, layers of grey and red shale, or red shale interbedded in a grey layer and vice versa. The last 15 m (50 ft) of Well 1 and 2 are mainly grey shale with a high content of quartz. Microscopic pictures of cuttings that represent three drilled formations are shown in Fig. 7.

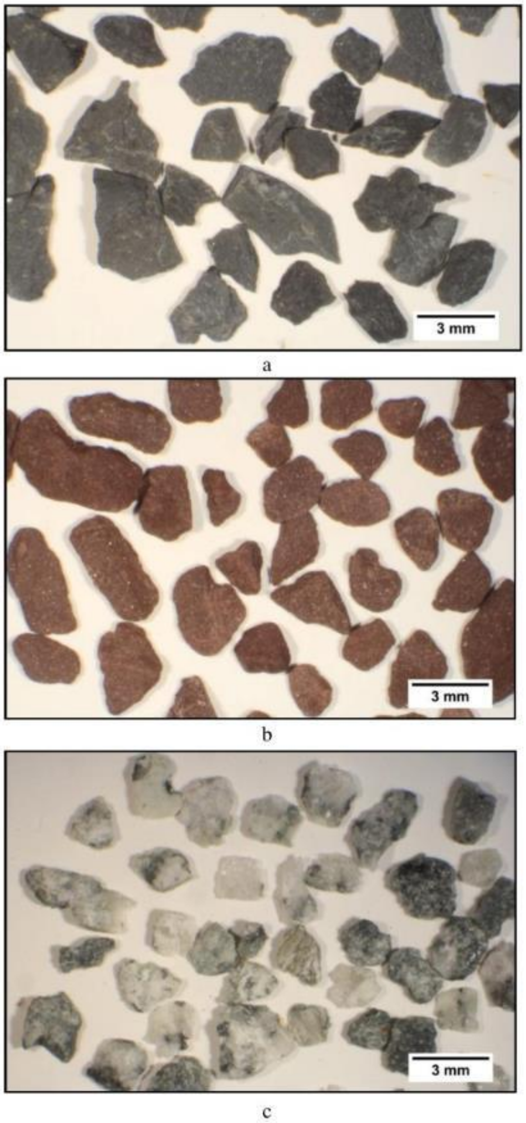

Fig. 7 – Cuttings geological analysis (a – grey shale, b – red shale, c – formation with a high content of quartz)

The last sections of Wells 1 and 2 appeared to be highly heterogeneous due to the differing amount of quartz in each sample; for this reason, no further cuttings analysis, or any drillability evaluation while drilling through this formation, was done. Therefore, the investigation was focused mostly on the depth interval of 0-105 m (0-350 ft) for all three wells. The obtained results allowed us to construct a geological cross-section of the site (Fig. 8).

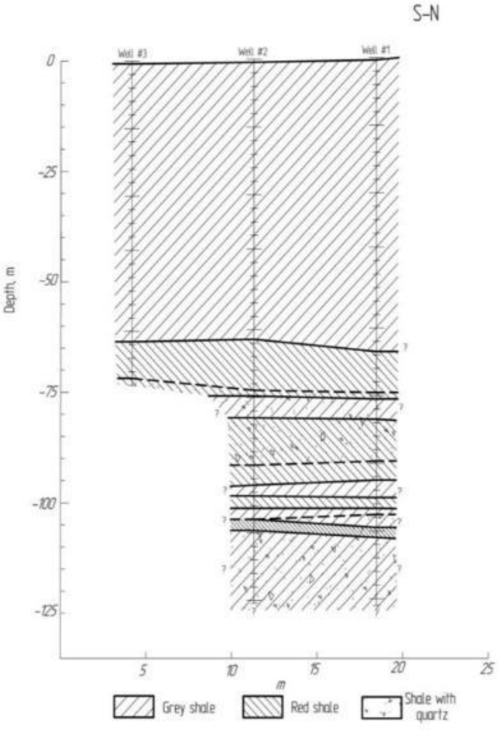

Fig. 8 – Geological cross-section of the site

The section from 72-90 m (240-300 ft) deep also has some quartz veins; however, the percentage of quartz is quite small and it had a negligible effect on the drilling performance.

Additionally, some samples were collected from exposures of shale on the surface of the field site for rock characterization. A brief observation of these samples shows that grey shale (Fig. 9) is a highly brittle sedimentary rock with a brightly expressed laminate structure, while red shale (Fig. 10) is expected to be much more compact and intact rock. However, unconfined compressive strength values, estimated from point load index test (load was applied in direction normal to bedding), are approximately equal for both rocks.

Unconfined compressive strength results for these rocks are shown in Table 2.

Table 2 Unconfined compressive strength of the rocks

Rock type	Value (MPa)
Grey shale	61
Red shale	56

Fig. 9 – Grey shale sample

Fig. 10 – Red shale sample

4.3 Cuttings size interpretation

From each well, several intervals were chosen for further analysis. For each sample from those intervals ROP, WOB, CI and mean particle size (d) values were plotted. WOB values are shown in kN, ROP in meters per hour.

4.3.1 Particle size distribution analysis in grey shale

As section 1, samples 12-21 (39.3-63.6 m) of Well 1 have been analyzed. Drilling was performed with a roller cone bit and without the pVARD tool.

In Fig. 11 a bar PSD diagram for this section is shown, along with CI, d, WOB and ROP values for each sample. In this section, samples 16-17 were not considered because visual analysis of cuttings showed a high content of quartz in these samples.

These diagrams show that cuttings size has a tendency to increase first and then decrease after certain point. Conversely, WOB and ROP values are continuously increasing. From the CI and d plots it can also be observed that both parameters are equivalent for size representation.

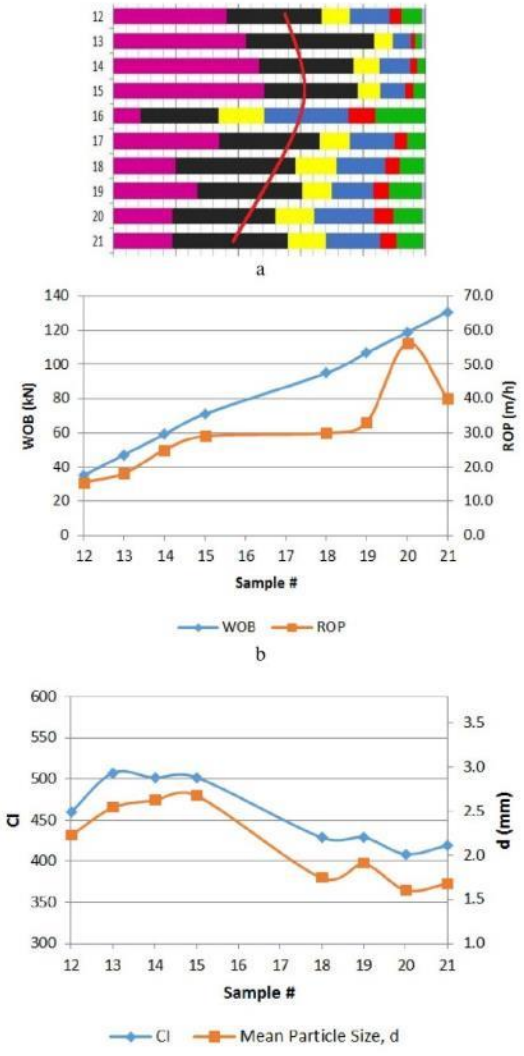

c

Fig. 11 – PSD analysis of Section 1 (a-bar PSD, b-Performance Parameters, c-Size Parameters)

Section 2 (samples 18-21, Well 3, 82.3-91.4 m), which was drilled with a PDC bit and no VARD tool, shows the same results as Section 1. The corresponding results are shown in Fig. 12.

Analyzing both sections, it is possible to say that after reaching a certain threshold of WOB cuttings get smaller because of crushing by the bit before they can be removed from the borehole by the drilling fluid. In both cases (Section 1 and 2) this threshold value is around 70-75 kN. After this value, the positive relation between ROP (WOB) and cuttings size changes into a negative one.

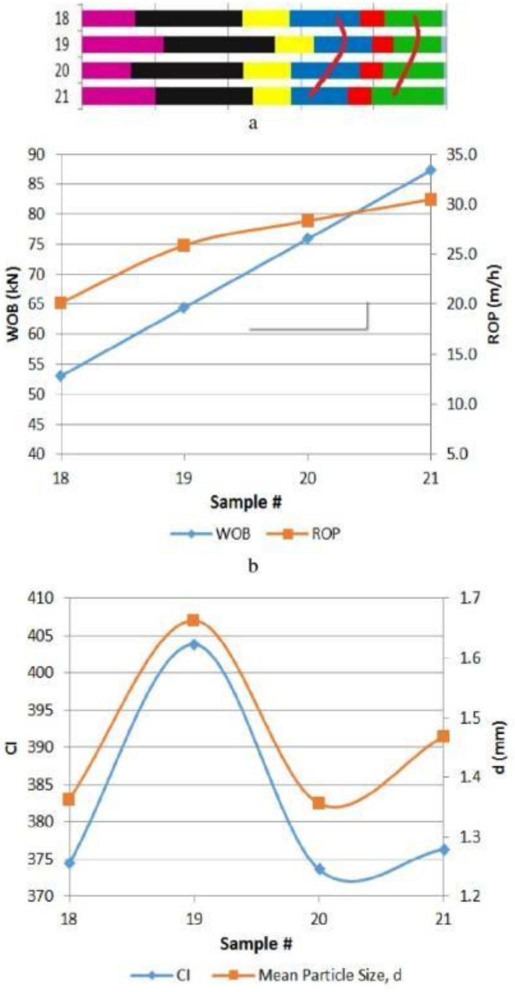

c

Fig. 12 – PSD analysis of Section 2. (a-bar PSD, b-Performance Parameters, c-Size Parameters)

This phenomenon could be explained by the laminate structure and brittleness of the grey shale. It is worth noticing that ROP is still increasing, while smaller cuttings are being generated. We might expect that, with more efficient cleaning of the borehole (a higher flowrate) ROP could be even higher, as additional energy would not be spent in regrinding cuttings. This leads us to conclude that, for weak and brittle formations efficient cleaning is a very important factor.

The other two sections (plots are not shown in the paper) analyzed from the grey shale showed a negative relationship between ROP and cuttings size. In both cases drilling was performed with a WOB over 65 kN, what supports the hypothesis about threshold value.

4.3.2 Particle size distribution analysis in red shale

Section 3 comprises samples 39-43 (71.6-73.6 m) from Well 3. These samples contain quartz, but as the percentage is quite small and constant for all samples we assume that it has no significant effect on the performance and cuttings size. Drilling was performed with the PDC bit and with the pVARD tool.

The bar PSD diagram for this section and the corresponding CI, d, WOB and ROP graphs are shown in Fig. 13.

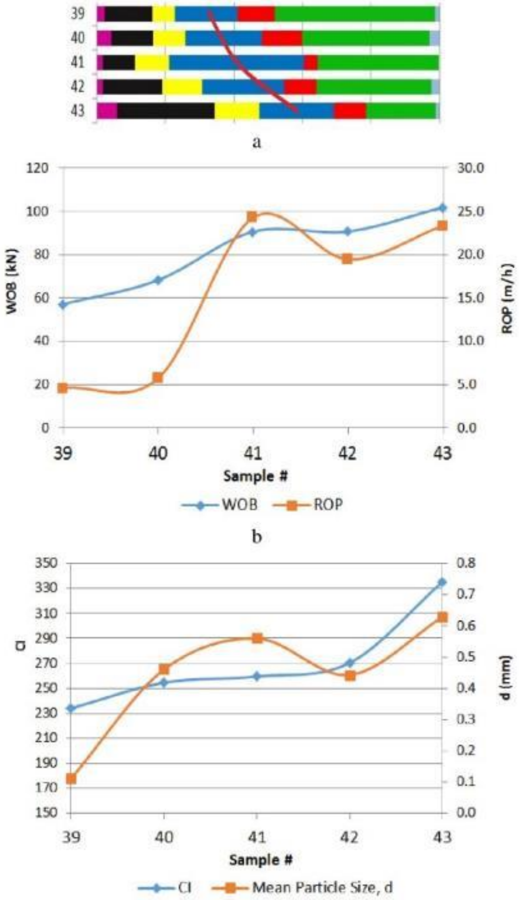

a

b

c

Fig. 13 - PSD analysis of Section 3. (a-bar PSD, b-Performance Parameters, c-Size Parameters)

For drilling in red shale, the cuttings size and ROP (as well as WOB) have a positive relationship for all the WOB range; in other words, bigger cuttings are generated while drilling with higher ROP. Additional analyses performed on other sections of the red shale are consistent with this affirmation.

The same particle size analysis against performance parameters was made for the bottom section of Wells 1 and 2. Although it was mentioned that this formation was highly heterogeneous, the results obtained also support the statement that ROP and cuttings size have a positive relationship. However, is important to keep in mind that, in this case, the change in cuttings size could be due to changing formation (from quartz veins to shale and vice versa).

Also due to natural brittleness of the shale and drillsrting vibrations cavings could occur and consequently affect original particle size distribution of the drill cuttings samples. However, the extent to which cavings could affect particle size distribution is yet to be investigated.

There is no apparent relationship found for ROP and cuttings size in highly interbedded formations.

On the other hand, no conclusive results could be obtained for the use of the pVARD tool. Even though the use of this tool showed an increased performance in the red shale [12], the cuttings analyses did not show a consistent increase in size for all the sections analyzed.

Heterogeneity in the formations and fluctuations in the flushing flowrate and drill string rotary speed might be a reason for the irregularity of the results. It is clear that further work is required to solve this inconsistency.

So far, some preliminary studies performed by ADL members Yingjian Xiao and Jinghan Zhong on concrete samples with different strength values, have shown good results for the cuttings size in drilling with the pVARD tool. Laboratory work on natural rock drilling is expected to be performed later to confirm these results.

5. CONCLUSIONS

The analysis of the results obtained from the field and laboratory work that has been performed lead us to the following conclusions:

- Bar particle distribution diagram (BPSD) is a very useful instrument for graphical representation of cuttings samples. It is easier to perceive information from BPSD than from regular PSD.
- The mean particle size (d) and the Coarseness Index (CI) are suitable for rough numerical characterizing of cuttings size and comparison between samples. Mean size and CI are mainly interchangeable and show a similar relationship with ROP and WOB. Nevertheless, a bar PSD diagram provides more detailed information about cuttings samples.

- ROP and cuttings size (CI, d) have a mainly positive relationship. For very brittle and laminate structure formations like grey shale, this relation might become negative if the WOB is increased over a certain value.
- Efficient cleaning of the borehole is important for drilling through weak, brittle formations.
- The PSD analysis shows consistent results for homogeneous formations. For heterogeneous formations results are not consistent.
- Inconsistency in field data could be caused by formation heterogeneity, cuttings collection issues (incomplete samples were collected), fluctuations in flowrate and rotary speed.

REFERENCES

1. Caenn, R., H. C. H. Darley, and G.R. Gray. 2011. Introduction to drilling fluids. In *Composition and properties of drilling and completion fluids*, 6th ed. Gulf Professional Pub, 1-2.
2. Lenormand, R. and O. Fonta. 2007. Advances in measuring porosity and permeability from drill cuttings. In *Proceedings of the 2007 SPE/EAGE Reservoir Characterization and Simulation Conference, Abu Dhabi, 28 – 30 October 2007,* eds. Curran Associates Inc, 135-143.
3. Carugo, C., A. Malossi, P. Balossino, R. Galimberti, L. Gioacchini, F. Pingitore, and F. Rivolta, 2013. Advanced cuttings analysis improves reservoir characterization and reduces operating times in shale gas drilling project. In *Proceedings of the International Petroleum Technology Conference 2013: Challenging Technology and Economic Limits to Meet the Global Energy Demand, IPTC 2013,Beijing, 26 - 28 March 2013,* eds. Society of Petroleum Engineers 7 5654-5668.
4. Altindag, R. 2003. Estimation of penetration rate in percussive drilling by means of coarseness index and mean particle size. *Rock Mechanics and Rock Engineering*. 36(4): 323-332.
5. Pfleider, E. and R. L. Blake, 1953. Research on the cutting action of the diamond drill bit. *Mining Eng.* 5: 187-195.
6. Ersoy, A. and M. Waller, 1997. Drilling detritus and the operating parameters of thermally stable PDC core bits. *International Journal of Rock Mechanics and Mining Sciences.* 34(7): 1109-1123.
7. Wills, B.A. and T.J. Napier-Munn, 2006. Particle Size Analysis. In *Wills' Mineral Processing Technology*, ed. Elsevier Science & Technology Books, 90 – 108.
8. Brezani, I. and F. Zelenak. 2010. Improving the effectivity of work with rosin-rammler diagram by using MATLAB (R) GUI tool. *Acta Montanistica Slovaca.* 15(2): 152-157.
9. ASTM D422-63 2007-e2, Standard Test Method for Particle-Size Analysis of Soils, ASTM International, West Conshohocken, PA, 2007, www.astm.org
10. Roxborough, F. and A. Rispin. 1973. Mechanical cutting characteristics of lower chalk. *Tunnels & Tunnelling International.* 5(3)
11. Deely, C. 1947. Diamond core drilling methods and problems. *Petroleum Engineer.* 18(9).
12. Rana, P.S. 2014. Field Trial Report. Unpublished document.